Nonreciprocity and nonlinearity: Applications in complex plasmas and time series

Ingo Joachim Laut

München 2017

Nonreciprocity and nonlinearity: Applications in complex plasmas and time series

Ingo Joachim Laut

Dissertation
an der Fakultät für Physik
der Ludwig-Maximilians-Universität
München

vorgelegt von
Ingo Joachim Laut
aus München

München, den 14. September 2017

Erstgutachter: Prof. Dr. Dr. h. c. Gregor Morfill
Zweitgutachter: Prof. Dr. Hartmut Zohm
Tag der mündlichen Prüfung: 15. November 2017

Contents

Zusammenfassung

Newtons drittes Gesetz von Aktion und Reaktion ist ein Grundpfeiler der klassischen Mechanik. In Nichtgleichgewichtssystemen kann dieses Gesetz durch effektive Wechselwirkungen, welche durch einen weiteren Körper vermittelt werden, gebrochen werden. In ähnlicher Weise bereicherte die Entdeckung des deterministischen Chaos das Gebiet der Zeitserienanalyse. Im Rahmen dieser Dissertation werden dynamische Effekte, die auf der nichtreziproken Wechselwirkung in komplexen Plasmen basieren, und der Einfluss der Fourierphasen nichtlinearer Zeitserien untersucht.

In einem komplexen Plasma, welches aus geladenen Mikropartikeln in einem schwach ionisierten Plasma besteht, können strömende Ionen die Rolle dieses weiteren Körpers übernehmen. Der erste untersuchte Effekt ist die Modenkopplungs-Instabilität, bei der bestimmte Schwingungsmoden in einem zweidimensionalen Plasmakristall exponentiell wachsen. In Simulationen wird gezeigt, dass die Instabilibät durch ein anisotropes horizontales Potential in einer asymmetrischen Art und Weise ausgelöst werden kann. Dadurch wird die Instabilität in nur zwei oder vier der sechs möglichen Richtungen aktiviert. In sehr guter Übereinstimmung zu früheren Experimenten wird während der asymmetrisch ausgelösten Instabilität eine synchronisierte Teilchenbewegung beobachtet. Es wird ein Ordnungsparameter entwickelt, der das richtungsabhängige Synchronisationsmuster quantifiziert. Es werden mögliche Mechanismen diskutiert, die zu einem weiteren Symmetriebruch führen der nicht durch das anisotrope Potential erklärt werden kann.

Ein weiterer Effekt, der auf nichtreziproken Wechselwirkungen basiert, ist der Gitterführungseffekt (englisch *channeling*). Ein zuätzliches Teilchen, welches nicht Teil des zweidimensionalen Kristallverbunds ist, bewegt sich knapp überhalb des Kristalls mit annähernd konstanter Geschwindigkeit auf einer durch die Kristallstruktur vorgegebenen Bahn. Der Effekt wird in Simulationen reproduziert. Aufgrund der Nichtreziprozität der Wechselwirkungen zieht das zusätzliche Teilchen umliegende Teilchen an, während es selbst eine repulsive Kraft von den sich annähernden Teilchen erfährt. Dies führt zu einem intrinsischen Antrieb des Teilchens. Mit einem einfachen theoretischen Modell für den Antriebsmechanismus kann die Geschwindigkeit des zusätzlichen Teilchens vorhergesagt werden.

Die Tatsache, dass die gesamte nichtlineare Information einer Zeitserie in den Fourierphasen kodiert ist, wird in einigen Algorithmen zur Surrogaterzeugung genutzt, hat darüber hinaus jedoch keine große Beachtung gefunden. In dieser Arbeit wird gezeigt, dass Korrelationen in den Fourierphasen Nichtlinearitätsmaße beeinflussen können. Es wird gezeigt,

dass die Phasenkorrelationen das Ergebnis von Nichtlinearitätsmaßen beeinflussen können. Phasenkorrelationen in amplitudenregulierten Surrogatalgorithmen, die eigentlich frei von nichtlinearer Information sein sollten, kann zu einer Nichtentdeckung von Nichtlinearitäten führen. Es zeigt sich, dass der nichtlineare Vorhersagefehler ein besseres Nichtlinearitätsmaß ist als neuere, von Netzwerken abgeleitete Maße.

Abstract

Newton's third law of action and reaction is one pillar of classical mechanics. In nonequilibrium systems this fundamental law can be broken when the effective interaction is mediated by a third body, enabling surprising and counterintuitive effects. In a similar manner, the discovery of deterministic chaos in nonlinear systems enriched the field of time series analysis. This thesis covers dynamical effects based on nonreciprocal interactions in complex plasmas and sheds a light on the role of the Fourier phases in nonlinear time series.

In a complex plasma, which consists of charged microparticles immersed in a weakly ionized gas, streaming ions can play the role of the third body in the microparticle interaction. As a first nonreciprocity effect, the asymmetric triggering of the mode-coupling instability, where some wave modes in a two-dimensional plasma crystal grow exponentially with time, is studied in molecular-dynamics simulations. It is shown that an anisotropic confinement in the horizontal plane can trigger the instability in only two or four out of the six directions that are allowed in the hexagonal crystal lattice. In very good agreement with previous experimental observations, the asymmetric triggering of the instability is accompanied by a synchronized motion of the particles. A novel order parameter is developed to quantify the direction-dependent synchronization pattern. Possible mechanisms leading to a more delicate symmetry breaking that cannot be explained by the anisotropic confinement are also discussed.

A second effect based on nonreciprocal particle interactions is the channeling mechanism, where an extra particle that is not part of the two-dimensional crystal lattice floats slightly above the crystal and moves with almost constant velocity through a channel formed by the lattice. The mechanism is reproduced in simulations. It is shown that due to the nonreciprocity of the interactions, the extra particle attracts nearby particles, while it is itself repelled from the approaching particles, leading to a self-propelled motion of the extra particle. A simple theoretical model for the propulsion is provided which predicts the velocity of the extra particle.

The fact that all nonlinearities of a time series reside in the Fourier phases is implicitly used in many schemes for generating surrogates, but has not received much attention beyond that. Here, correlations in the Fourier phases are shown to have an impact on the nonlinear properties of a time series. Spurious phase correlations in amplitude-adjusted surrogates, that should be devoid of nonlinear information, can in turn lead to a nondetection of nonlinearity. Finally, by comparing different nonlinearity measures, the nonlinear prediction error is found to be superior to more recent measures derived from network theory.

Chapter 1

Introduction

1.1 Nonlinear time series analysis

One main goal of nonlinear time series analysis is to determine whether a system has underlying chaotic dynamics [1, 2]. To this end, some measure of nonlinearity, most of which are derived from chaos theory, is calculated for the time series. As the outcome of most tests for nonlinearity yields a numerical value that alone cannot confirm or exclude the presence of nonlinearity, the measure is often also applied to surrogate data which mimic the linear properties of the original data but contain no nonlinearities. If nonlinearity is found in such a statistical test in a time series, purely linear models to describe the underlying physics can be ruled out.

1.1.1 Phase space representation

In his much renowned paper on cellular convection, Lorenz conjectured that low-dimensional, deterministic equations can show chaotic behavior in such a way that "prediction of the sufficiently distant future is impossible by any method, unless the present conditions are known exactly" [3]. The geometric shape of such a *strange* attractor in phase space cannot be described by an integer dimension, which led to the development of a multitude of dimensionality measures for chaotic systems.

In Fig. 1.1(a)–(d) are shown snapshots of the time evolution of 50 different realizations of trajectories on the attractor of the Lorenz system [3],

$$\begin{aligned} \frac{\mathrm{d}x}{\mathrm{d}t} &= \sigma(y-x), \\ \frac{\mathrm{d}y}{\mathrm{d}t} &= x(\rho-z)-y, \\ \frac{\mathrm{d}z}{\mathrm{d}t} &= xy-\beta z, \end{aligned} \tag{1.1}$$

where $\sigma = 10$, $\beta = 8/3$ and $\rho = 28$. Initially, at $t = 0$, the trajectories are within a small distance in phase space. First, the strong dependence on the initial conditions leads

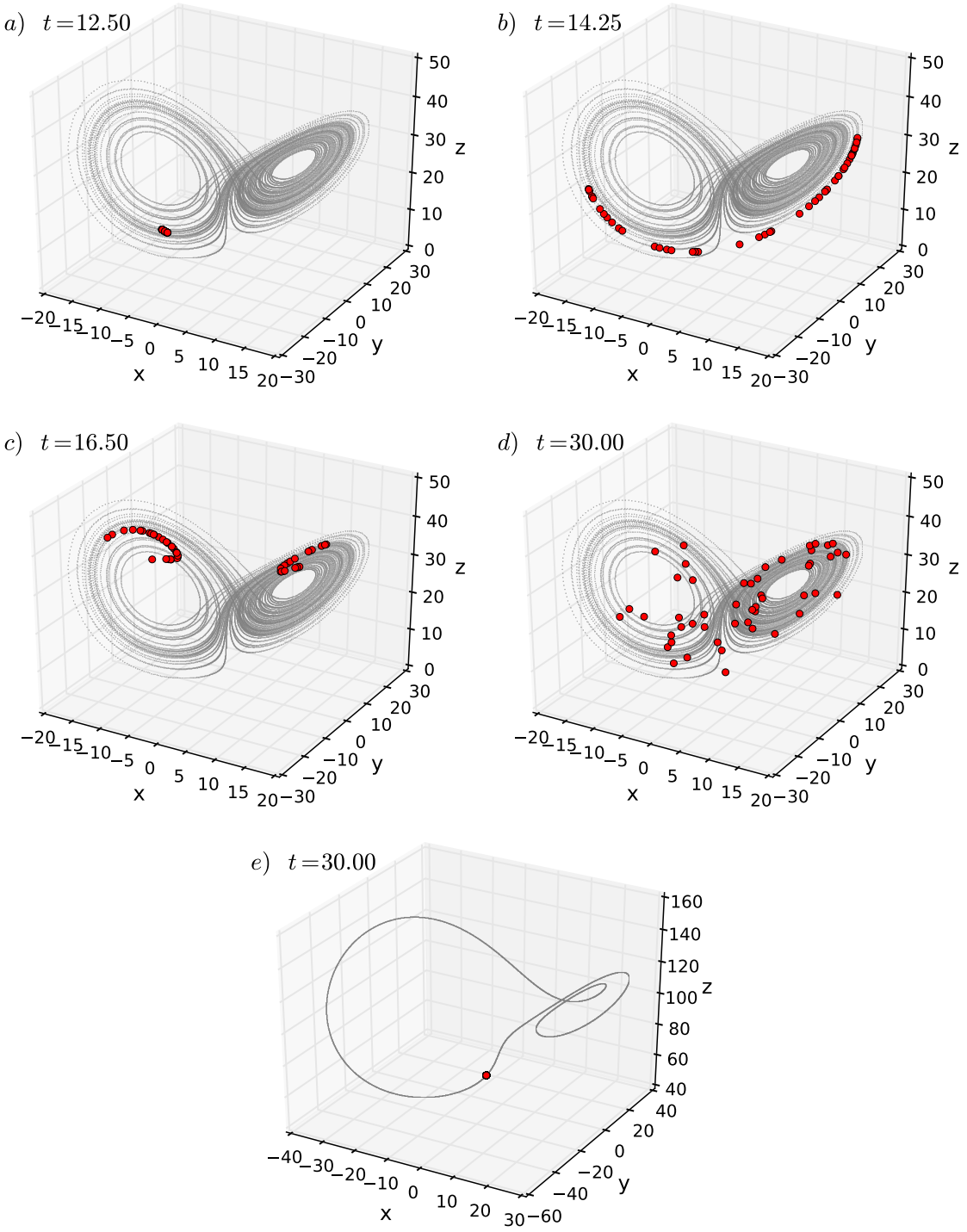

Figure 1.1: Sensitivity on initial conditions. (a)–(d): A trajectory of the Lorenz system (see Eq. 1.1) over 50 time units is shown in gray. At the time step indicated in the top left of each panel, the state of the system and of 49 other trajectories that were within a distance of 0.0001 at $t = 0$ are shown as red dots. (e): The same for the linear regime of the Lorenz system with $\beta = 100$.

to a spread of the different realizations in a direction tangential to the trajectories, see Fig. 1.1(a, b). The realizations then further spread (c) until they are scattered over the full attractor (d). This "unpredictability" of the dynamics of trajectories that are initially close in phase space is most striking when compared to the dynamics of the system in the linear regime shown in Fig. 1.1(e).

If not all variables of a dynamical system can be observed, it is difficult to fully characterize the system. Often, only one observable is available from a measurement of a system that is expected to depend on more than one parameters. The full dynamics of the system can then be regained by embedding the time series in an appropriate higher-dimensional phase space. Takens addressed the question how the phase space of an attractor could be reconstructed from this time series of observables [4]. He proved that there exists an embedding, i. e., a continuous mapping of the time series to an embedding space that is topologically equivalent to the attractor. The embedding is called delay-time embedding of a time series $\{y_i\}$ and reads [5]

$$\mathbf{y}_n = (y_{n-(d-1)\tau}, y_{n-(d-2)\tau}, \ldots, y_n) \tag{1.2}$$

where d is the embedding dimensions and τ the delay time.

If the embedding dimension is too small, points may be near to one another only because the attractor is projected onto a lower dimension. With the false neighbor method [6], an appropriate embedding dimension d can be found by analyzing how the fraction of false neighbors decreases with increasing d. For determining an appropriate delay time τ two values can be considered: the first zero-crossing of the autocorrelation function or the first minimum of the mutual information [7].

1.1.2 Fourier representation

An elegant definition of "nonlinearity" can be given with the Fourier representation

$$FT[\{y_n\}] = \frac{1}{N}\sum_n y_n e^{2\pi i k n/N} = |a_k| e^{i\phi_k} \tag{1.3}$$

of a time series $\{y_n\}$ of length N. All linear information is contained in the Fourier amplitudes $|a_k|$, while all *nonlinear* information is contained in the Fourier phases ϕ_k. The reasoning is as follows. The linear properties of a time series are those that can be reproduced by an autoregressive (AR) process of the form

$$y_n = \mu + \sum_i c_i y_{n-i} + \epsilon_n, \tag{1.4}$$

where μ is a constant, ϵ_n is uncorrelated noise and the c_i are the parameters of the process. The Yule-Walker equations [8, 9] relate the c_i of the corresponding AR process to the autocorrelation function

$$ACF[\{y_n\}] = \sum_n y_n y_{n+\Delta} \tag{1.5}$$

of the time series. Since the Wiener-Khinchin theorem [10] is a bijective relation between the autocorrelation function and the power spectrum $\{|a_k|^2\}$ given by

$$FT\,[\,ACF[\{y_n\}]\,] = |a_k|^2, \tag{1.6}$$

the linear information of a time series is solely contained in the magnitude of the Fourier coefficients $|a_k|$. As a consequence, the nonlinear information is encoded in the Fourier phases. This argument is often used for the generation of so-called surrogate data (see Sec. 1.1.4) that mimic the linear properties of a time series, but have all nonlinearities destroyed.

1.1.3 Measures for nonlinearity

Correlation dimension

Measures for nonlinearity can be divided into two classes, namely static and dynamic measures. Static measures take the data set as a whole into consideration and describe the distribution of the data points in phase space. Dynamical measures, in contrast, also take the time dynamics into account that are encoded in the underlying equations or can be reconstructed from the embedded data if the equations are not known.

The dimension estimates mentioned in Sec. 1.1.1 are static measures. One prime example is the correlation dimension D_2. As a first step, one calculates the correlation dimension

$$C(r) = \frac{1}{N(N+1)} \sum_{n,j} \theta(r - r_{nj}) \tag{1.7}$$

for different values of r. $r_{nj} = \|\mathbf{r}_n - \mathbf{r}_j\|$ and θ is the Heaviside function. If the growth of $C(r)$ with radius r obeys a power law, the correlation dimension can be associated with the slope of $C(r)$ in a double-logarithmic scale:

$$D_2 = \lim_{r\to 0} \lim_{N\to\infty} \frac{d \log C(r)}{d \log r}. \tag{1.8}$$

The attractor of the Lorenz equations shown in Fig. 1.1(a)–(d) has a non-integer correlation dimension of $D_2 = 2.05 \pm 0.01$ [11].

Nonlinear Prediction Error

The nonlinear prediction error is an example of a dynamical measure for nonlinearity [12, 13]. The idea is that for a deterministic system, points that are close to each other in phase space have a comparable time evolution. By averaging over the future positions of the neighbors of a point $\mathbf{y}_n$, an estimate $\mathbf{F}(\mathbf{y}_n, T)$ for the future position is obtained as

$$\mathbf{F}(\mathbf{y}_n, T) = \frac{1}{g} \sum_{j\in U_g(n)} \mathbf{y}_{j+T}, \tag{1.9}$$

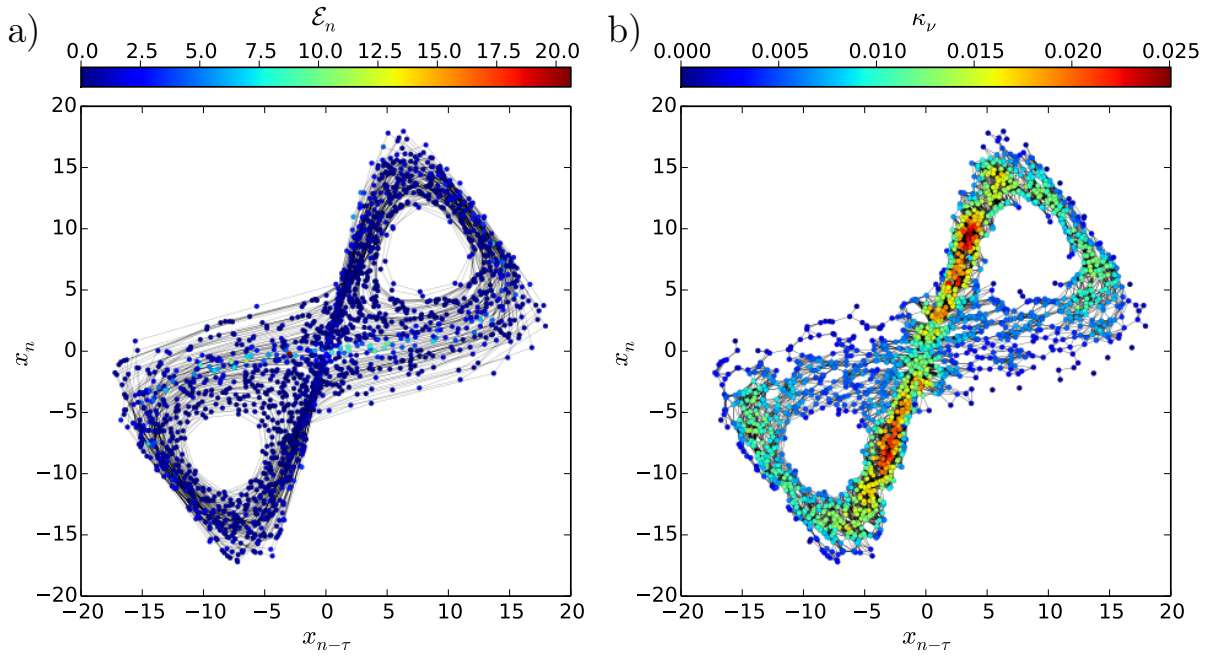

Figure 1.2: (a) Local nonlinear prediction error $\mathcal{E}_n$ for the Lorenz system. Gray lines connect points in embedding space that correspond to successive time steps. (b) Degree centrality κ_ν derived from a recurrence network. Gray lines connect points that are connected in the network. For the visualization of the network, every node ν is located at the point in phase space that it corresponds to.

where $U_g(n)$ is the set of indices of the g nearest neighbors of point $\mathbf{y}_n$ and T is the lead time. The local nonlinear prediction error is then the distance from this estimate to the actual future position in phase space $\mathbf{y}_{n+T}$,

$$\mathcal{E}_n = \sqrt{\|\mathbf{y}_{n+T} - \mathbf{F}(\mathbf{y}_n, T)\|^2}, \tag{1.10}$$

and the global nonlinear prediction error is obtained by averaging over all points in phase space $\mathcal{E} = \sqrt{\langle \mathcal{E}_n^2 \rangle_n}$.

The local nonlinear prediction error $\mathcal{E}_n$ for the Lorenz system (see Eq. 1.1) is shown in Fig. 1.2(a). 2000 data steps of the x coordinate with a step size of 0.08 time units are considered. The data are embedded in $d = 3$ dimensions with a delay time of $\tau = 0.16$. The arrangement of the embedded points resembles the butterfly-shaped structure of the original Lorenz system shown in Fig. 1.1. For $g = 4$ and a lead time of $T = 5$, $\mathcal{E}_n$ is small for almost every data point, only for one point it is comparable to the size of the attractor. The x coordinate thus contains enough nonlinear information of the three-dimensional system to enable nonlinear prediction. If compared to a similar data set without nonlinear information (a *surrogate*, see Sec. 1.1.4), one would expect a significantly smaller value of $\mathcal{E}$ for the nonlinear time series.

Recurrence network

With the substantial success of complex network theory in various fields of physics [14–17], it has recently also been applied to time series analysis. As there is no "natural" way of how to create a network from a time series, different procedures have been suggested to translate the data into nodes and edges of a network [18–21]. One procedure is the *recurrence network* [20, 22, 23] which contains the information which points are sufficiently close to each other in phase space. The adjacency matrix A of the recurrence network [23] reads

$$A_{mn}(\epsilon) = \Theta\left(\epsilon - \|\mathbf{y}_m - \mathbf{y}_n\|\right) - \delta_{mn}, \tag{1.11}$$

where the $\{\mathbf{y}_n\}$ are the (embedded) points of the time series in phase space and ϵ an appropriate threshold. The recurrence network as defined by Eq. 1.11 is an unweighted network as A_{mn} can only take two values: it is unity if there is a connection, or edge, between nodes m and n, and zero otherwise. The Kronecker delta in Eq. 1.11 prevents self-loops such that $A_{nn}=0$.

Once the recurrence network is obtained for a time series, it can be analyzed with different network measures. The most prominent measure for any network is the degree centrality k_ν which counts the number of nodes that are connected to node ν [24],

$$k_\nu = \sum_{i=0}^{N-1} A_{\nu,i}. \tag{1.12}$$

Dividing by the maximum possible value yields the connectivity κ_ν. The average connectivity κ is defined as the mean of all nodes κ_ν,

$$\kappa = \frac{1}{N}\sum_{\nu=0}^{N-1}\kappa_\nu = \frac{1}{N(N-1)}\sum_{\nu=0}^{N-1} k_\nu. \tag{1.13}$$

Other measures include the clustering coefficient which is the fraction of neighbors of a node ν that are themselves connected and the average path length from ν to any other node of the network. In Ref. [20], the bifurcation diagram of the logistic map, a one-dimensional nonlinear system, was analyzed. Different regimes such as period doublings and chaos were identified by dynamical changes of the measures as the control parameter was varied.

Symbolic network

A different approach to generate a network from a time series is a symbolic network [21]. For each segment of a windowed sequence of a time series, an ordinal pattern of indices is obtained that sorts the segment. Each ordinal pattern corresponds to one node of the symbolic network. Nodes corresponding to consecutive time windows are then connected in the network in order to save the temporal information. Since the amplitude information is lost in this approach, it was suggested in Ref. [25] to combine the symbolic network with a transition network where the nodes of the network are the binned amplitudes of the time series.

In the symbolic network proposed in Ref. [25], each time step n is associated with a symbol-pair containing the amplitude information $\alpha(n)$ and the ordinal pattern $\pi(n)$. The former is calculated by binning the time series in the interval $[\min(\{y_n\}), \max(\{y_n\})]$ into Q equal regions. $\alpha(n)$ is then simply the bin number of y_n. To compute $\pi(n)$, one considers the sequence $[y_n, y_{n+\tau}, ..., y_{n+(L-1)\tau}]$ for a given time-delay τ and window length L. The ordinal pattern $\pi(n) = (\beta_1, \beta_2, ..., \beta_L)$ contains the indices sorting the sequence such that $y_{n-1+\beta_1} \leq y_{n-1+\beta_2} \leq ... \leq y_{n-1+\beta_L}$. The symbol-pair at step n, ($\alpha(n)$, $\pi(n)$), is then one node of the network, and it is connected by a directed link to the symbol-pair ($\alpha(n+1)$, $\pi(n+1)$) of the successive time step. In this representation, different time steps may correspond to the same symbol-pairs. Only nodes whose symbol-pairs are present in the time series are part of the network, the actual number of nodes may thus be smaller than the maximal possible value $N^{\max} = Q \cdot L!$.

1.1.4 Surrogate data

Surrogates are *ersatz* data which have the same linear properties as the original time series, but contain no nonlinearities. They provide a statistical test for a nonlinearity measure M in a model-independent way. The outcome of measure M of the original time series under study is compared to the outcomes $\{M_s\}$ of the surrogate data. The significance of the deviation of the time series from a set of surrogates is calculated as

$$S(M) = \frac{|M - \langle\{M_s\}\rangle_s|}{\sigma(\{M_s\})}, \tag{1.14}$$

where $\langle\{M_s\}\rangle_s$ and $\sigma(\{M_s\})$ are the mean and standard deviation of the outcomes of the measures $\{M_s\}$ for the surrogate data.

Surrogate generating algorithms rely on the definition of nonlinearity that was given in Sec. 1.1.2, which states that all nonlinear information of a time series is contained in the Fourier phases. The most popular algorithms thus randomize the Fourier phases in order to remove potential nonlinearities present in the time series while preserving the autocorrelation function. Alternatively, the time series can be shuffled to destroy the nonlinearities, but then also the autocorrelation function is changed and has to be restored in an iterative scheme. Below, different surrogate generating algorithms are presented.

The scheme for Fourier-transformed (FT) surrogates [26] is shown in Fig. 1.3(a). The original time series is Fourier transformed and the Fourier phases are replaced by random, uncorrelated phases. The surrogate is then obtained by simply doing the back-transform. Since the Fourier amplitudes are not altered, the FT surrogates are guaranteed to have the same autocorrelation function as the original time series. The amplitude spectrum of the original time series is only preserved if it obeys a Gaussian distribution; FT surrogates are thus limited to time series that already have a Gaussian distribution, or that were rank-ordered-remapped onto a Gaussian distribution. The remapping is done as follows. For a time series of length N, generate N Gaussian random numbers $\{\xi_n\}$. Reorder the $\{\xi_n\}$ such that if y_i is the kth smallest of the $\{y_n\}$, then ξ_i is also the kth smallest of the

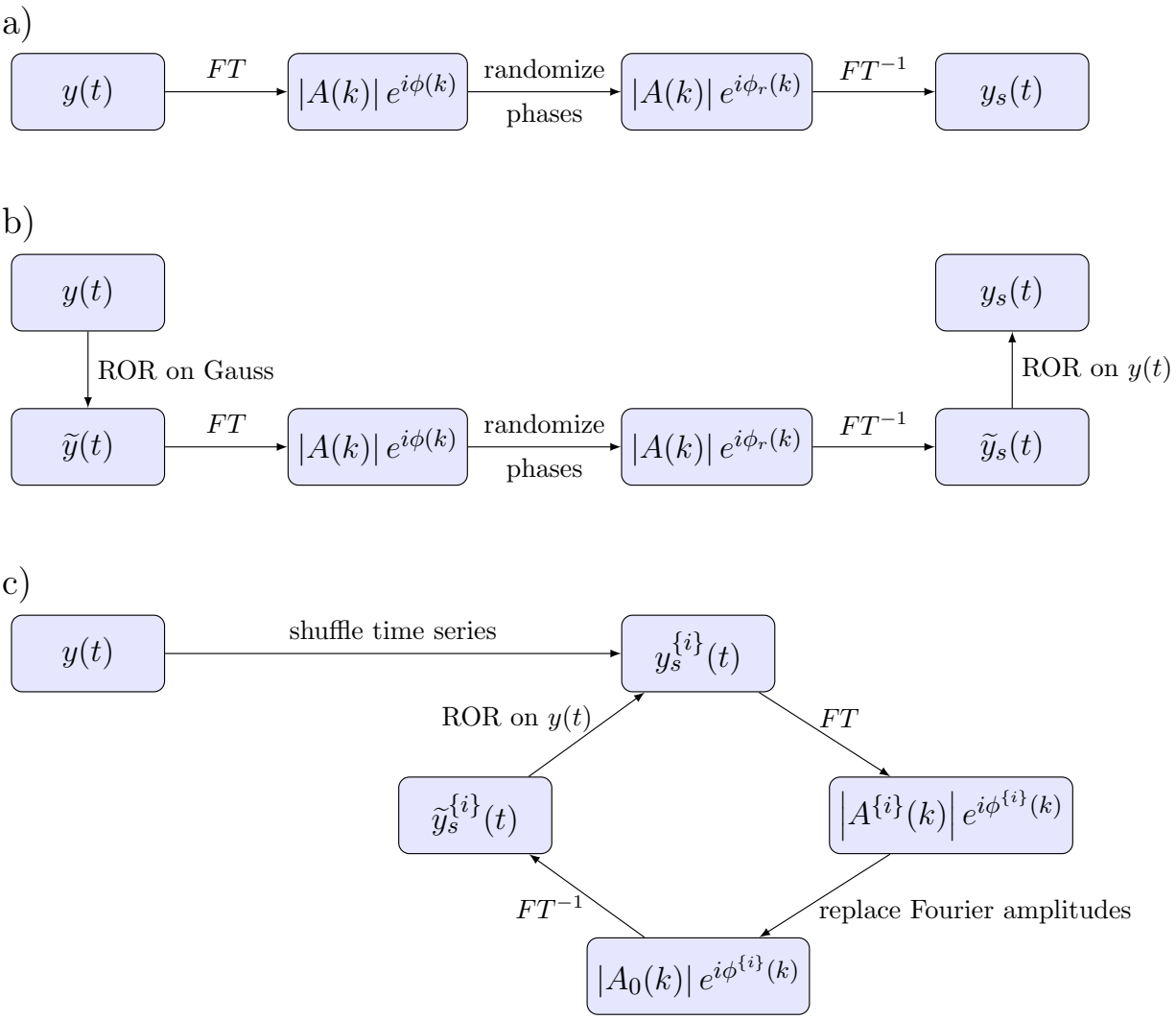

Figure 1.3: Surrogate generating schemes. (a) FT surrogate. (b) AAFT surrogate. (c) IAAFT surrogate. Both the AAFT and IAAFT schemes use a rank-ordered-remapping (ROR) step. FT surrogates do not have a remapping step, but can only be applied to time series with Gaussian amplitude distributions.

$\{\xi_n\}$. The reordered $\{\xi_n\}$ thus "follow" the original time series $\{y_n\}$ while having a Gaussian amplitude distribution.

Amplitude-adjusted Fourier-transformed (AAFT) surrogates can be generated for time series with arbitrary amplitude distribution [26]. As sketched in Fig. 1.3(b), a copy of the original time series is first rank-ordered-remapped to a Gaussian distribution. Then, a FT surrogate of this remapped time series is created. Finally, the surrogate is rank-ordered-remapped to the original time series. The surrogate has the same amplitude distribution as the original time series, but a slightly broader power spectrum due to the final remapping step. As the remapping is done after the phase randomization, new correlations are can be introduced in the Fourier phases. Moreover, in Ref. [27] it was shown that the broader power spectrum may lead to an erroneous detection of nonlinearity in purely linear data.

The iterated amplitude-adjusted Fourier-transformed (IAAFT) surrogates were designed to overcome the shortcoming of AAFT surrogates described in Ref. [27]. The Fourier amplitudes $|A_0(k)|$ of the original time series $y(t)$ are initially saved. Then, as sketched in Fig. 1.3(c), the scheme starts with a random shuffle $y_s^{\{0\}}(t)$ of $y(t)$. Now, the following two steps are repeated iteratively. (1) Take the Fourier transform of $y_s^{\{i\}}(t)$, replace the corresponding Fourier amplitudes by $|A_0(k)|$ and transform back. The resulting time series $\widetilde{y}_s^{\{i\}}(t)$ has now exactly the same autocorrelation function as the original time series, but not the same amplitude distribution. (2) Rank-ordered-remap $\widetilde{y}_s^{\{i\}}(t)$ to $y(t)$ to obtain $y_s^{\{i+1\}}(t)$ for the next iteration. The IAAFT scheme stops when the remapping step leads to no reordering of the time series.

The IAAFT surrogates reproduce both the autocorrelation and the amplitude spectrum of the original time series. However, the randomness of the Fourier phases that is only given at the very beginning of the iteration scheme can no longer be guaranteed. The rank-ordered-remapping step of the AAFT and IAAFT schemes can induce spurious phase correlations in the surrogates. It was shown in Ref. [28] that induced phase correlations in AAFT and IAAFT surrogate data can lead to a nondetection of weak nonlinearities.

1.2 Complex plasmas

Complex or dusty plasmas are weakly ionized gases containing charged particles. In space, dusty plasmas are ubiquitous, for example in planetary rings and interstellar clouds [29]. In distinction to these naturally occurring systems, laboratory realizations of dusty plasmas, often with monodisperse micron-sized particles instead of polydisperse "dust", are termed complex plasmas. A strong coupling regime, meaning that the interaction energy largely exceeds the thermal energy, can be easily obtained due to the large particle charge and relatively low interparticle distances and kinetic temperatures. Ordered structures, called plasma crystals, were predicted by Ikezi in 1986 [30] and observed independently by different research groups in 1994 [31–33]. Today, complex plasmas can be used to study fields as diverse as plasma physics, astrophysics, phase transitions, nonlinear dynamics, solid state physics and applications to industry and engineering [34–37].

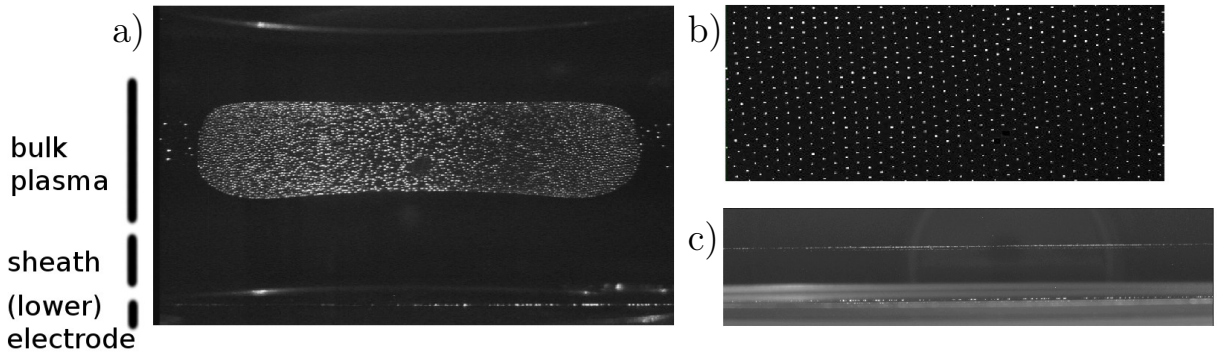

Figure 1.4: Complex-plasma experiments. (a) Side view of a large three-dimensional cloud in the PK-3 Plus laboratory onboard the International Space Station [39]. (b) and (c): Top view and side view of a two-dimensional plasma crystal in the Large Chamber in the research group of complex plasmas. Courtesy of John Meyer. For (a) and (c), the approximate positions of the bulk plasma, the plasma sheath and the electrode are shown to the left.

1.2.1 Basic Properties of Complex Plasmas

Most experiments with complex plasmas can be divided into two classes. First, large three-dimensional homogeneous structures can be obtained under microgravity conditions or with thermophoresis [38]. The particles levitate in the quasineutral bulk plasma. Microgravity conditions are met onboard the International Space Station [39] and during parabolic flights [40]. Various crystal geometries, like bcc, fcc and hcp lattices, can be observed. A typical side view is shown in Fig. 1.4(a). In the second class of experiments, in ground-based laboratories, particles levitate in the plasma sheath region above the lower electrode, where there is a force balance between, primarily, the gravitational and electrostatic forces (see Fig. 1.4(b) and (c)). The plasma sheath is the boundary region of positive space charge where an electric field decreases from the electrode to the bulk plasma [41]. In the sheath, the particles form extended structures consisting of 10^4–10^5 particles arranged in one or a few horizontal layers. In a layer, the particles can form a hexagonal lattice.

The most important elementary processes in complex plasmas are the charging of the particles, the screening of the resulting electrostatic potential through the electrons and ions of the plasma, and the momentum transfer from flowing ions to the particles [35, 36]. The processes have a large impact on the external forces acting on the particles, and on the mutual particle interactions that will also be discussed in the following.

Particle charging

The charge Q of a particle is determined by the electron and ion fluxes on the particle. As the electrons have a higher mobility, the electron flux on an initially uncharged particle will be larger than the ion flux, leading to an increasingly negative charge of the particle. Stationarity is reached when the electron flux onto the negatively charged particle decreases

due to electrostatic repulsion and the electron and ion fluxes are balanced. A well-known approach to calculate the fluxes is the orbital motion limited (OML) approximation, where the cross section determining the fluxes are derived from the conservation laws of energy and angular momentum. A single particle in a collisionless isotropic plasma is assumed. In this theory, the normalized surface potential $z = \phi_s e/k_B T_e$ only depends on the electron-to-ion temperature ratio $\tau = T_e/T_i$ and the electron-to-ion mass ratio (determined by the gas used). For typical parameters $\tau \simeq 10$–100 one obtains $z \simeq 2$–4 [35]. For small particles with a radius $a_p \ll \lambda$, where λ is the Debye screening length, the charge is given by $Q = a_p \phi_s$, and thus increases linearly with particle radius a_p. For typical values, $a_p = 1$ μm and $k_B T_e = 1$ eV, the charge is $Q = -(1\text{–}3) \times 10^3 e$ [35]. The effect of plasma flow anisotropy and ion-neutral collisions on the charging process can be taken into account using more complicated approaches, such as particle-in-cell simulations [42, 43].

Screening

The electrostatic potential $\phi(r)$ around a spherical charged particle of radius a_p in an isotropic and collisionless plasma obeys the Poisson equation

$$\triangle \phi = -4\pi e(n_i - n_e) \tag{1.15}$$

with the boundary conditions $\phi(\infty) = 0$ and $\phi(a_p) = \phi_s$ [35]. n_i and n_e are the ion and electron densities which also depend on the potential ϕ and distance r [44, 45]. The surface potential ϕ_s at the particle radius a_p is connected to the particle charge Q through $\frac{\mathrm{d}\phi}{\mathrm{d}r}\big|_{r=a_p} = -Q/a_p^2$. An exact solution for Eq. 1.15 can be obtained numerically, or various approximations can be made to obtain analytical solutions. Assuming a Boltzmann distribution for ions and electrons

$$n_{e,i} = n_0 e^{\pm e\phi/k_B T_{e,i}}, \tag{1.16}$$

where n_0 is the unperturbed plasma density, and further assuming $|e\phi_s/k_B T_{e,i}| \ll 1$ and $a_p \ll \lambda$, one obtains the Debye-Hückel (Yukawa) potential

$$\phi(r) = \frac{Q}{r} \exp\left(-\frac{r}{\lambda}\right). \tag{1.17}$$

The linearized Debye length $\lambda = \lambda_e \lambda_i / \sqrt{\lambda_e^2 + \lambda_i^2}$ is expressed as function of the electronic and ionic Debye lengths $\lambda_{e,i} = \sqrt{k_B T_{e,i}/(4\pi n_0 e^2)}$. The absorption of plasma particles on the particle surface has a great influence on the electrostatic potential. While this effect is rather weak for electrons, the ion flux on the particle makes the ion distribution non-Boltzmann. In the absence of ion-neutral collisions, the ion flux leads to a power-law dependence $\phi(r) \propto r^{-2}$ in the far-field of the potential [35, 46]. In the other limit of a strongly collisional plasma, the far-field instead has a Coulomb-like dependence $\phi(r) \propto r^{-1}$ [47, 48]. As the far-field limit can often be neglected, the bare Yukawa potential of Eq. 1.17 is often used in isotropic complex plasmas.

Often, the requirement $|e\phi_s/k_B T_{e,i}| \ll 1$ is not fulfilled in complex plasmas, but numerical solutions of the Poisson equation show that the potential is still of Yukawa type with an

effective screening length λ_{eff}. In Ref. [49] it was shown numerically that for distances less than a few λ, $\lambda_{\text{eff}} \simeq \lambda$ for small particles with $a_p \ll \lambda$, and $\lambda_{\text{eff}} \simeq \lambda_e$ for larger particles. As a refinement, the numerical solutions can be fitted by an algebraic function with a single parameter, the nonlinearity parameter $\beta = (a_p/\lambda_i)(e|\phi_s|/k_B T_i)$ [48, 50, 51].

In the plasma sheath region, there is a strong electric field that leads to a downward drift of the ions relative to the particle that greatly influences the electrostatic screening. The flowing ions are focused below the particle, where they form a positive excess charge called the *plasma wake*. The electrostatic potential in the presence of ion flow has attracted considerable attention [52–57]. In Ref. [52], the anisotropic potential of a particle in a "cold" ion flow (where direction and velocity of all ions are identical) was calculated. Lampe *et al.* found similar results with a numerical simulation [53]. The anisotropic potential obtained in Ref. [53] is shown in Fig. 1.5(a). The positive wake directly behind the particle is followed by another, negative wake. Such a pronounced oscillatory character of the wake was also found in other works [54, 56]. All of these works were done under the assumption of a homogeneous plasma. As this assumption is usually not true in the levitation region of the particles, Kompaneets *et al.* studied the plasma wake in an inhomogeneous plasma and found that the oscillatory character can be considerably reduced [57]. A simple way to model of the anisotropic electric field of Fig. 1.5(a) is the pointlike wake model [58]. The complicated wake structure is replaced by a positive pointlike charge q positioned a fixed distance δ below (in z direction) the particle of negative charge Q, see Fig. 1.5(b). The potential of a particle placed at the origin then reads

$$\phi(\mathbf{r}) = \frac{Q}{r} \exp\left(-\frac{r}{\lambda}\right) + \frac{q}{r_w} \exp\left(-\frac{r_w}{\lambda}\right), \tag{1.18}$$

where $\mathbf{r}$ is the three-dimensional position vector (with magnitude r) and $\mathbf{r}_w = \mathbf{r} + \delta \mathbf{e}_z$. Here, $\mathbf{e}_z$ is the vertical unit vector. The force between two particles derived from Eq. 1.18 is nonreciprocal, as it is mediated by a third body, the wake charge (see Sec. 1.2.2).

Electric and gravitational forces

The electric force acting on a particle can be written as

$$\mathbf{F}_e = Q\mathbf{E}, \tag{1.19}$$

where Q is the charge of the particle and $\mathbf{E}$ is the electric field. In Ref. [59] it was shown that the polarization of the bulk plasma in response to the electric field creates an additional field near the particle, increasing the electrostatic force. As the correction is on the order of a_p^2/λ^2, it can be neglected in most complex-plasma conditions.

For micron-sized particles in ground-based experiments, the gravitational force cannot be neglected. With M the mass of the particle and g the gravitational acceleration, it reads

$$\mathbf{F}_g = -Mg\mathbf{e}_z. \tag{1.20}$$

The counterdirected electric and gravitational forces in the plasma sheath lead to a vertical confinement of the particles in ground-based experiments which can be assumed to be

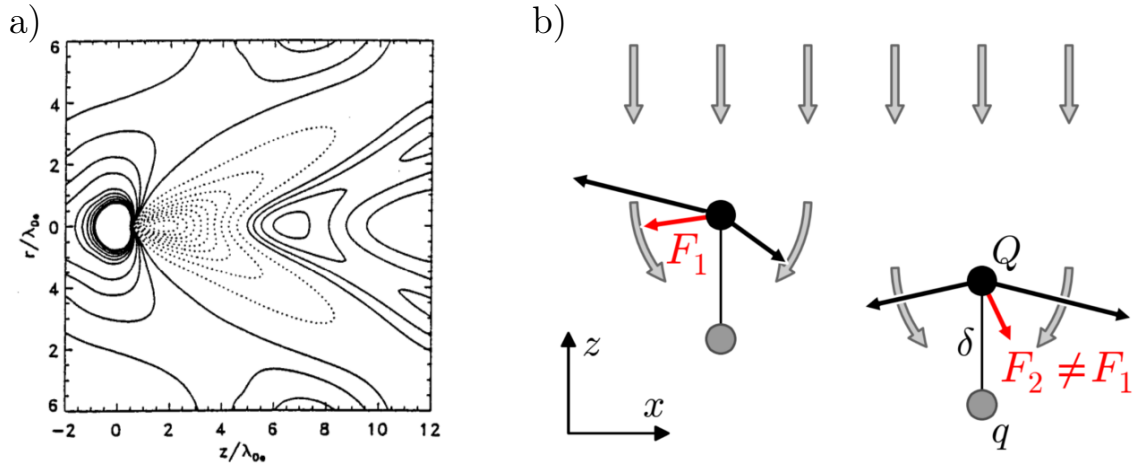

Figure 1.5: (a) Contour plot of the anisotropic potential around a negatively charged particle in an ion flow in the positive z direction. Solid lines indicate a negative potential, the dotted lines indicate the positive *plasma wake*. Reprinted from Ref. [53], with the permission of AIP Publishing. (b) Sketch of the pointlike wake model. The ion flow from top to bottom, sketched by the arrows, is focused below the particle of charge $Q < 0$ (black circles), where it forms a positive wake charge q (gray circles). The distance δ between the particle and its wake is assumed to be constant. For each particle, the repulsive force between the particles and the attractive force towards the wake charge is shown by black arrows. The resulting forces (red arrows) are nonreciprocal, as the lower particle feels a stronger attraction to the wake than the upper particle.

parabolic [60]. Only for large amplitude oscillations, the nonlinear terms of the confinement play a role [61, 62].

Neutral drag

The neutral drag force is caused by collisions with neutral gas atoms or molecules. It is often modeled by the Epstein formula [63]

$$\mathbf{F}_{\text{fric}} = -\delta_E \frac{4\pi}{3} n_n M_n \bar{c}_n a_p^2 \mathbf{v} \equiv -M\nu\mathbf{v}, \tag{1.21}$$

where n_n, M_n, and $\bar{c}_n$ are number density, mass, and mean thermal velocity of the neutral gas atoms. The Epstein coefficient has the limiting cases $\delta_E = 1$ (specular reflection of the gas atoms) and $\delta_E = 1.442$ (diffusive reflection). In Ref. [64], the value $\delta_E = 1.26$ was measured for a complex-plasma system by accelerating a single particle with a laser. The friction coefficient ν has the dimension of inverse time and describes the damping rate of motion of a particle.

Ion drag

The ion drag force is the momentum transfer from the flowing ions onto the particle. There exist two main approaches for the calculation of the ion drag force, the binary collision

approach and the kinetic approach. The binary collision approach considers the ballistic scattering of the ions at the (isotropic) particle potential, excluding any type of multiple collision, in particular, with neutrals. The force is obtained by averaging over all impact parameters and a given ion velocity distribution. An analytical expression was derived by Barnes *et al.* for small scattering angles within the Debye sphere [65]. Khrapak *et al.* extended the approach to the *nonlinear* regime of larger scattering angles [66, 67].

In the (linear response) kinetic approach, the plasma anisotropy and the ion-neutral collisions can be taken into account. To this end, the Poisson equation is coupled to a kinetic equation for ions, and the resulting electrostatic potential is evaluated at the position of the particle to obtain the ion drag force [68, 69]. It was argued in Refs. [68, 70] that the binary collision approach and the kinetic approach are rather complementary, as the former is more suitable to describe (nonlinear) scattering with subthermal ions in the bulk while the latter is suitable for the very anisotropic electrostatic potential in the case of superthermal ions flowing in the sheath region of the plasma.

1.2.2 Nonreciprocity effects in complex plasmas

A multitude of dynamical processes can be studied with complex plasmas at the kinetic level. Phase transitions can be studied in three-dimensional [71, 72] and two-dimensional [73, 74] systems. In two-dimensional complex plasmas, many dynamical effects are connected with waves, for example transport processes [75, 76], harmonic generation [77, 78] and extreme events [79, 80]. The nonreciprocity of the particle interactions, mediated by wake charges, has profound effects on the dynamics in dusty plasmas [60]. In three dimensional complex plasmas, the nonreciprocal interparticle forces can lead to the formation of particle strings in the crystalline [81, 82] and the liquid [83] phase. In the following, dynamical processes that are based on the nonreciprocal interparticle interaction in two-dimensional systems will be discussed.

In the case of the pointlike wake model, the force $\mathbf{F}_{ji}$ exerted by particle j (and its wake) on particle i is derived from Eq. 1.18 as

$$\begin{aligned}\mathbf{F}_{ji} = &\frac{Q^2}{r_{ji}^2}\exp\left(-\frac{r_{ji}}{\lambda}\right)\left(1+\frac{r_{ji}}{\lambda}\right)\frac{\mathbf{r}_{ji}}{r_{ji}} \\ &+\frac{qQ}{r_{w_{ji}}^2}\exp\left(-\frac{r_{w_{ji}}}{\lambda}\right)\left(1+\frac{r_{w_{ji}}}{\lambda}\right)\frac{\mathbf{r}_{w_{ji}}}{r_{w_{ji}}},\end{aligned} \tag{1.22}$$

where $Q<0$ is the particle charge, $q>0$ the wake charge, λ the screening length, $\mathbf{r}_{ji}=\mathbf{r}_i-\mathbf{r}_j$ and $\mathbf{r}_{w_{ji}}=\mathbf{r}_i-(\mathbf{r}_j-\delta\mathbf{e}_z)$.

Equation 1.22 contains the nonreciprocal nature of the particle interactions, since in general $\mathbf{r}_{w_{ji}} \neq -\mathbf{r}_{w_{ij}}$, and thus $\mathbf{F}_{ji} \neq -\mathbf{F}_{ij}$. The effective interaction, which does not consider the flowing ions but only their effect in the particle-particle interaction, is nonreciprocal and Newton's third law of *actio* and *reactio* is broken. It can be seen in the sketch of Fig. 1.5(b) that since the lower particle is closer to the wake of the upper particle, it feels a weaker repulsive force than the upper particle. Many dynamical effects in two-dimensional plasma

crystals are based on the nonreciprocal interactions. Most prominently, the mode-coupling instability [58, 84, 85] can be understood and quantitatively analyzed within this model. More recently, the pointlike wake model also successfully described the existence of different kinetic temperatures for each of the species in a binary mixture [86].

Mode-coupling instability

When Ivlev and Morfill included the ion wakes in the analysis of dust lattice waves in one dimension, they discovered an instability due to a coupling between the vertical and longitudinal modes [58]. Shortly afterwards, the prediction was confirmed experimentally [84] and the theory of the mode-coupling instability (MCI) has since been thoroughly studied in experiments [87, 88], theory [89, 90] and simulations [85, 91].

In Ref. [89], an infinite hexagonal lattice was considered. The particle interaction was given by the pointlike wake model of Eq. 1.22 and the vertical confinement was parabolic with a confinement strength Ω_z. One considers small deviations $\mathbf{d}_i$ from the equilibrium particle position $\mathbf{r}_i^0$ and assumes $\mathbf{d}_i \propto \exp[-i\omega t + i\mathbf{k}\cdot\mathbf{r}_i^0]$ for the wave-induced deviations. The dispersion relation is then obtained from $\det[\mathbf{D}-\omega(\omega+i\nu)\mathbf{I}] = 0$ where $\mathbf{I}$ is the unit matrix and $\mathbf{D}$ is the dynamical matrix

$$\mathbf{D} = \begin{pmatrix} \alpha_h - \beta & 2\gamma & i\sigma_x \\ 2\gamma & \alpha_h + \beta & i\sigma_y \\ i\sigma_x & i\sigma_y & \Omega_z^2 - 2\alpha_v \end{pmatrix}. \tag{1.23}$$

The elements α_h, α_v, β, γ and $\sigma_{x,y}$ are expressed in units of the dust lattice frequency $\Omega_{DL} = \sqrt{Q^2/M\lambda^3}$ and depend on the magnitude and the direction of wave vector $\mathbf{k}$, the crystal interaction range $\kappa = a/\lambda$ (a is the equilibrium interparticle distance) and the wake parameters $\tilde{q} = q/|Q|$ and $\tilde{\delta} = \delta/a$:

$$\begin{aligned}
\alpha_h &= (1-\tilde{q}) \sum_{m,n} e^{-K}(K^{-1} + K^{-2} + K^{-3}) \sin^2(\mathbf{k}\cdot\mathbf{s}/2), \\
\alpha_v &= (1-\tilde{q}) \sum_{m,n} e^{-K}(K^{-2} + K^{-3}) \sin^2(\mathbf{k}\cdot\mathbf{s}/2), \\
\beta &= (1-\tilde{q}) \sum_{m,n} e^{-K}(K^{-1} + 3K^{-2} + 3K^{-3})[(s_y^2 - s_x^2)/s^2] \sin^2(\mathbf{k}\cdot\mathbf{s}/2), \\
\gamma &= (1-\tilde{q}) \sum_{m,n} e^{-K}(K^{-1} + 3K^{-2} + 3K^{-3})[s_x s_y/s^2] \sin^2(\mathbf{k}\cdot\mathbf{s}/2), \\
\sigma_{x,y} &= \tilde{q}\tilde{\delta} \sum_{m,n} e^{-K}(K^{-1} + 3K^{-2} + 3K^{-3})[s_{x,y}/s^2] \sin(\mathbf{k}\cdot\mathbf{s}).
\end{aligned} \tag{1.24}$$

The sum goes over all integers m and n with excluded $(0,0)$ with $K = \kappa\sqrt{m^2+n^2+mn}$, and the two-dimensional vector $\mathbf{s}$ has the components $s_x = (\sqrt{3}/2)ma$ and $s_y = ma/2 + na$. It was assumed that $\tilde{\delta}^2 \ll 1$. Writing $\Omega^2 = \omega(\omega + i\nu)$, the dispersion relation reads [89]

$$(\Omega^2 - \Omega_{\mathrm{L}}^2)(\Omega^2 - \Omega_{\mathrm{TH}}^2)(\Omega^2 - \Omega_{\mathrm{TV}}^2) + \Omega_c^4(\Omega^2 - \Omega_{\mathrm{mix}}^2) = 0, \tag{1.25}$$

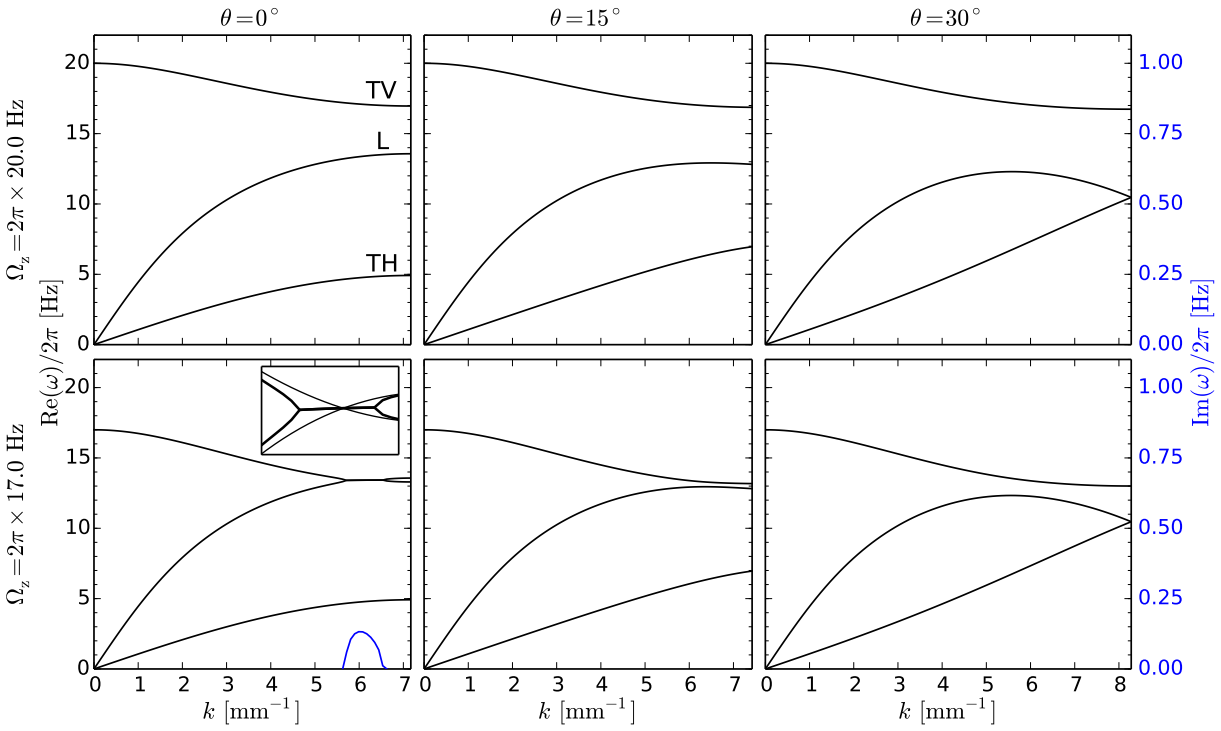

Figure 1.6: Modes in a two-dimensional plasma crystal obtained from the solution of the dispersion relation Eq. 1.25 for different wave directions θ and vertical confinement strengths Ω_z. The real part of the solution ω is shown in black, corresponding to the longitudinal (L), transverse horizontal (TH) and transverse vertical (TV) modes. The imaginary part, shown in blue, corresponds to the growth rate of the hybrid mode that forms during the MCI. The inset (zoomed in to the hybrid mode) also shows the uncoupled modes as thin lines. Parameters: $M = 6.1 \times 10^{-13}\,\mathrm{kg}$, $Q = -18000e$, $\lambda = 400\,\mu\mathrm{m}$, $\nu = 1\,\mathrm{s}^{-1}$, $q = 0.2|Q|$, $\delta = 0.3\lambda$.

where

$$\begin{aligned} \Omega_c &= \sqrt{\sigma_x^2 + \sigma_y^2}, \\ \Omega_{\mathrm{mix}}^2 &= \alpha_h + \beta \frac{\sigma_x^2 - \sigma_y^2}{\sigma_x^2 + \sigma_y^2} - 4\gamma \frac{\sigma_x \sigma_y}{\sigma_x^2 + \sigma_y^2}, \end{aligned} \tag{1.26}$$

and the (uncoupled) wave modes are given by $\Omega_{\mathrm{L,TH}} = \sqrt{\alpha_h \pm \sqrt{\beta^2 + 4\gamma^2}}$ and $\Omega_{\mathrm{TV}} = \sqrt{\Omega_z^2 - 2\alpha_v}$.

The coupled wave modes are obtained by solving the dispersion relation 1.25. In the case of real solutions for ω, one obtains the branches of the longitudinal (L), transverse horizontal (TH) and transverse vertical (TV) modes. The modes are plotted for different wave directions θ in the upper line of Fig. 1.6. Only the wave vectors inside the first Brillouin zone are shown. The MCI is striggered upon decreasing the strength Ω_z of the vertical confinement; the L mode and the TV mode then intersect and one obtains complex

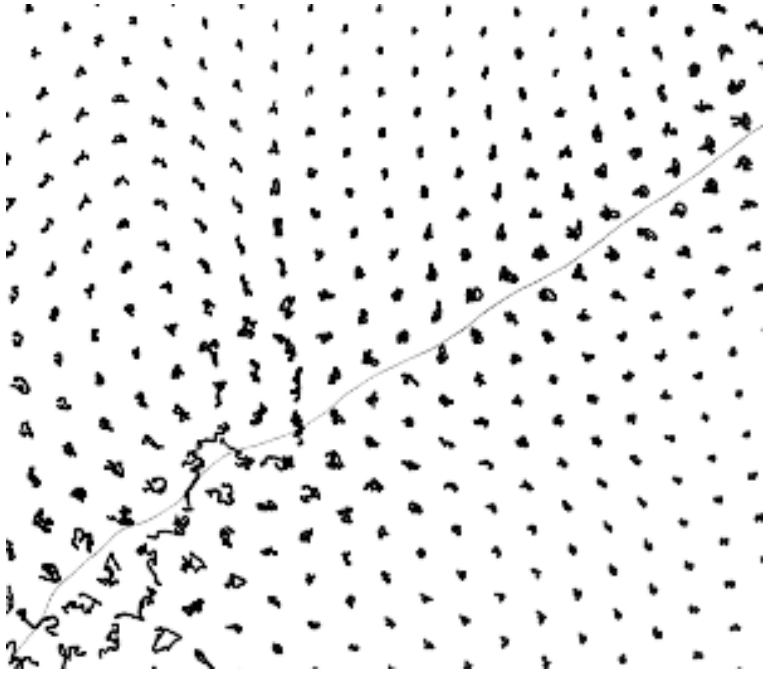

Figure 1.7: Trajectory of an upstream extra particle (top view). The inverted and superimposed pictures show the trajectory of an extra particle flowing above the crystal from the bottom left to the top right. Courtesy of Cheng-Ran Du.

conjugate solutions as the two modes form the unstable *hybrid* mode. As can be seen in the lower line of Fig. 1.6, the mode crossing initially takes place in the $\theta = 0°$ direction (and the directions $\theta = 60°$, $120°$, ..., $300°$ that are equivalent by symmetry). The imaginary part of the hybrid mode is responsible for an exponential growth of the wave motion in the crystal. In theory, the modes grow infinitely, but in experiments and in simulation the crystalline order of the crystal breaks at one point, leading to the melting of the crystal. A self-consistent wake model based on the kinetic equation for ions [90, 92] can give better results than the pointlike wake model when the physical parameters in the sheath region are well known. As this is rarely the case, the dispersion derived for the pointlike wake model (Eq. 1.25) is often used.

Extra particles

The influence of so-called extra particles moving below the plasma crystal have been thoroughly studied [93–95]. Rapidly moving extra particles excite waves in the crystal and increase its kinetic temperature. Extra particles moving at a velocity larger than the speed of sound of the crystal excite Mach cones that can be used to study wave dynamics [93, 94] and as diagnostic tool [96]. At velocities smaller than the speed of sound, lateral waves are excited that have a complicated structure due to the strongly-dispersive nature of waves in the crystal [95]. However, as the extra particle increases the kinetic temperature in the

crystal, it can disturb experiments where an undisturbed crystal is wanted. To eliminate this effect, the crystal can be "purified" by reducing the levitation height of the crystal such that the lower extra particles hit the lower electrode.

More recently, extra-particles moving *above* the crystal lattice were observed [97, 98]. These extra particles are called upstream particles as they are positioned upstream with respect to the ion flow that passes perpendicularly through the crystal lattice in the downward direction. Upstream particles are observed less frequently and have a smaller effect on the crystal lattice than the downstream extra particles (positioned below the lattice) [98]. It was observed that upstream particles can follow the channel formed by lines of neighboring particles as shown in Fig. 1.7. Despite ambient gas friction, the particles move at a nearly constant velocity.

1.2.3 Molecular-dynamics simulations

Molecular dynamics (MD) simulations have proven to be an adequate tool to study and compare a wide range of experimental conditions [84, 91, 99, 100]. The equations of motion read

$$M\ddot{\mathbf{r}}_i + M\nu\dot{\mathbf{r}}_i = \sum_{j\neq i} \mathbf{F}_{ji} + \mathbf{C}_i + \mathbf{L}_i \,, \tag{1.27}$$

where $\mathbf{r}_i$ is the position of particle i. Apart from the friction force described by the damping rate ν, the forces acting on a particle i are the interaction forces $\mathbf{F}_{ji}$ exerted by all other particles j, the confinement force $\mathbf{C}_i$ and a Langevin heat force $\mathbf{L}_i$.

The pairwise particle interaction is given by the pointlike wake model (Eq. 1.22), which is often used in MD simulations [85, 91, 101, 102]. In addition to a repulsive Yukawa force between two particles, an attractive component is exerted by the wake charge of one particle on the other particle.

In the simulations, the confinement force $\mathbf{C}_i$ can be used as a tunable parameter in order to control the lattice configuration [99, 103] and the crystal stability [84, 91]. A parabolic confinement well is often used to simulate a monolayer suspension [84, 99, 103–106]. To model a monolayer extended in the xy-plane, a highly anisotropic three-dimensional confinement well is used with a vertical confinement frequency $\Omega_z = 2\pi f_z$ that is about 100 times larger than the horizontal confinement $\Omega_h = 2\pi f_h$. The confinement force then reads

$$\mathbf{C}_i = -M \begin{pmatrix} \Omega_h^2 x_i \\ \Omega_h^2 y_i \\ \Omega_z^2 z_i \end{pmatrix} . \tag{1.28}$$

The central region of a crystal consisting of 3000 particles in a parabolic confinement is shown in Fig. 1.8(a).

Recently, a weak anisotropy was introduced in the horizontal plane in order to study the influence of an anisotropic horizontal confinement on a rotating plasma crystal in simulations [107]. The anisotropy can be described by introducing a confinement frequency $\Omega_\parallel = 2\pi f_\parallel$

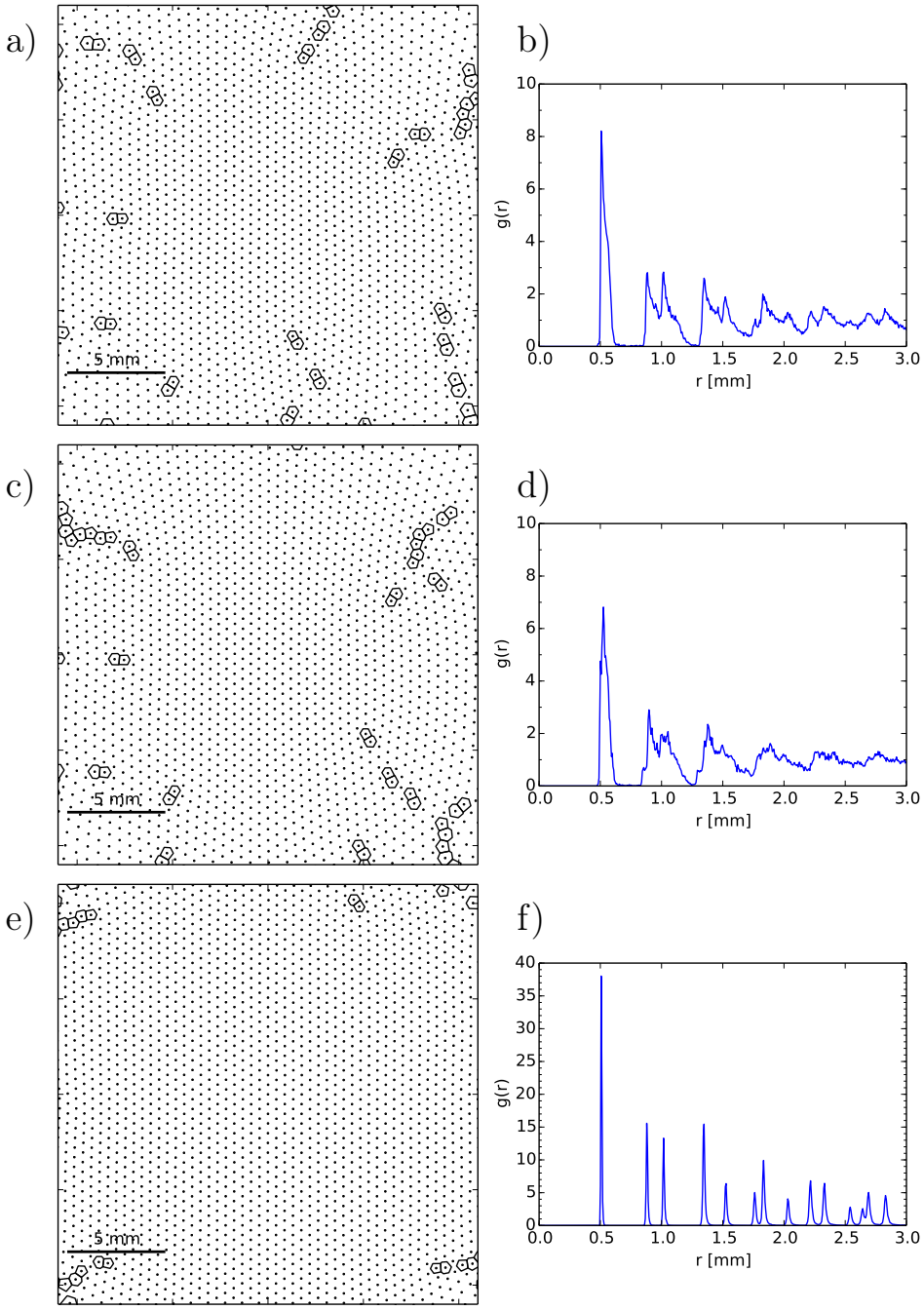

Figure 1.8: Top view and pair correlation function for simulated two-dimensional plasma crystals for different horizontal confinements. (a), (b) Parabolic confinement (see Eq. 1.28) with $f_h = 0.3\,\mathrm{Hz}$. (c), (d) Anisotropic parabolic confinement (see Eq. 1.29) with $f_\parallel = 0.315\,\mathrm{Hz}$, $f_\perp = 0.285\,\mathrm{Hz}$ and $\alpha = 0$. (e), (f) Tenth-order confinement (see Eq. 1.30) with $R = 15\,\mathrm{mm}$. Parameters: $N = 3000$, $M = 6.1 \times 10^{-13}\,\mathrm{kg}$, $Q = -18000e$, $\lambda = 400\,\mu\mathrm{m}$, $f_z = 22\,\mathrm{Hz}$, $\nu = 1\,\mathrm{s}^{-1}$, $T = 300\,\mathrm{K}$, $q = 0.2|Q|$, $\delta = 0.3\lambda$. The Voronoi cells are shown for all cells except the sixfold ones.

acting in the direction of an angle α and a smaller confinement frequency $\Omega_\perp = 2\pi f_\perp$ that is perpendicular to it. The confinement then reads

$$\mathbf{C}_i = -M \begin{pmatrix} \Omega_s^2 x_i + \Omega_a^2 (x_i \cos 2\alpha + y_i \sin 2\alpha) \\ \Omega_s^2 y_i + \Omega_a^2 (x_i \sin 2\alpha - y_i \cos 2\alpha) \\ \Omega_z^2 z_i \end{pmatrix}, \tag{1.29}$$

where $\Omega_{s,a}^2 = (\Omega_\parallel^2 \pm \Omega_\perp^2)/2$. In Fig. 1.8(c) a crystal that was compressed along the direction of the x-axis, i. e., with an angle $\alpha = 0°$, is shown. The crystal was initially equilibrated in an isotropic horizontal confinement and subsequently compressed by the anisotropic potential.

The parabolic horizontal confinement wells of Eqs. 1.28 and 1.29 lead to crystals where the interparticle distance increases from the center to the crystal edge. As a consequence, domains of crystalline order have slightly bent lines. Very homogeneous crystals can be obtained with higher-order confinement wells, which are flatter in the region occupied by the crystal and have steeper walls on their edges as compared to a parabolic confinement. A confinement derived from a tenth-order potential was proposed in Ref. [108] as

$$\mathbf{C}_i = -M \begin{pmatrix} 5(\rho_i^8/R^8)\Omega_h^2 x_i \\ 5(\rho_i^8/R^8)\Omega_h^2 y_i \\ \Omega_z^2 z_i \end{pmatrix}, \tag{1.30}$$

where $\rho_i = \sqrt{x_i^2 + y_i^2}$ is the radial particle position and R is the approximate radius of a comparable crystal in a parabolic horizontal confinement of strength Ω_h. A crystal confined in a tenth-order horizontal potential is shown in Fig. 1.8(e). It is apparent to the eye that the interparticle distance hardly varies in the central region of the crystal.

The particles are also coupled to a Langevin heat bath of temperature T,

$$\langle \mathbf{L}_i(t) \rangle = 0\,, \quad \langle \mathbf{L}_i(t+\tau)\mathbf{L}_j(t) \rangle = 2\nu M T \delta_{ij} \delta(\tau)\,. \tag{1.31}$$

δ_{ij} is the Kronecker delta and $\delta(\tau)$ is the delta function. The heat bath models the random excitations of the particles from the background gas.

The equations of motion (1.27) are integrated using the Beeman algorithm with predictor-corrector modifications [109, 110]. The code is parallelized using OpenMP.

1.2.4 Characterizing complex plasmas

Pair correlation

The pair correlation function $g(\mathbf{r})$ is a widely used tool to analyze the structure of particle arrangements. In two dimensions, it is defined as

$$g(\mathbf{r}) = \sum_i \frac{N_i^s(\mathbf{r}, dx, dy)}{N \rho \, dx \, dy}, \tag{1.32}$$

where $N_i^s(\mathbf{r}, dx, dy)$ is the number of particles in a rectangle of side lengths dx and dy a distance $\mathbf{r}$ from particle i, N is the number of particles and ρ the particle density in the area that is considered.

When the structure can be assumed to be isotropic in the plane, the radial pair correlation function is often considered as

$$g(r) = \sum_i \frac{N_i^r(r, dr)}{N 2r\pi dr\rho}, \tag{1.33}$$

where $N_i^r(r, dr)$ is the number of particles that are at a distance between r and $r + dr$ from particle i. The radial pair correlation function $g(r)$ for the simulated crystal with parabolic horizontal (see Fig. 1.8(a)) is shown in Fig. 1.8(b). It shows a distinct peak at the interparticle distance $a = 0.508$ mm, followed by subsequent peaks that are increasingly difficult to discriminate. For the horizontally compressed crystal, the peaks are less pronounced and $g(r)$ goes to unity for $r \simeq 3$ mm, see Fig. 1.8(d). Finally, $g(r)$ shows very sharp peak for the crystal in a tenth-order horizontal confinement shown in Fig. 1.8(f). For each crystal, $g(r)$ was calculated for a central region of radius 10 mm.

Fluctuation spectra

Particle current fluctuation spectra are well suited to study wave processes in complex plasmas. For a 2D plasma crystal, the spectra are calculated from the longitudinal (L), transverse horizontal (TH) and transverse vertical (TV) particle currents which are defined as [111]

$$\begin{aligned} V_{\mathrm{L}}(\mathbf{k}, t) &= \sum_j v_j^{\parallel}(t, \mathbf{k}) e^{-i\mathbf{k}\cdot\mathbf{r}_j}\,, \\ V_{\mathrm{TH}}(\mathbf{k}, t) &= \sum_j v_j^{\perp}(t, \mathbf{k}) e^{-i\mathbf{k}\cdot\mathbf{r}_j}\,, \\ V_{\mathrm{TV}}(\mathbf{k}, t) &= \sum_j v_{j,z}(t) e^{-i\mathbf{k}\cdot\mathbf{r}_j}\,, \end{aligned} \tag{1.34}$$

where $v_j^{\parallel}(t)$ and $v_j^{\perp}(t)$ are the components of the velocity of particle j at time t parallel and perpendicular to wave vector $\mathbf{k} = (k_x, k_y)$ in the horizontal plane. The spectra are then obtained from the Fourier transform in the time domain of the respective current,

$$\tilde{V}_s(\mathbf{k}, f) = FT[V_s(\mathbf{k}, t)] \tag{1.35}$$

where $s \in \{\mathrm{L}, \mathrm{TV}, \mathrm{TH}\}$. Each of the three currents corresponds to one of the three modes that are sustained in a (quasi-)two dimensional crystal. The spectra are thus well suited to measure the modes from experimental or simulated data and compare them to the modes obtained from the theoretical dispersion relation Eq. 1.25. The wave dynamics can be visualized by adding the three contributions $|\tilde{V}_{\mathrm{TOT}}|^2 = |\tilde{V}_{\mathrm{L}}|^2 + |\tilde{V}_{\mathrm{TH}}|^2 + |\tilde{V}_{\mathrm{TV}}|^2$ and visualizing them as function of magnitude of the wave vector k and frequency f for a given orientation

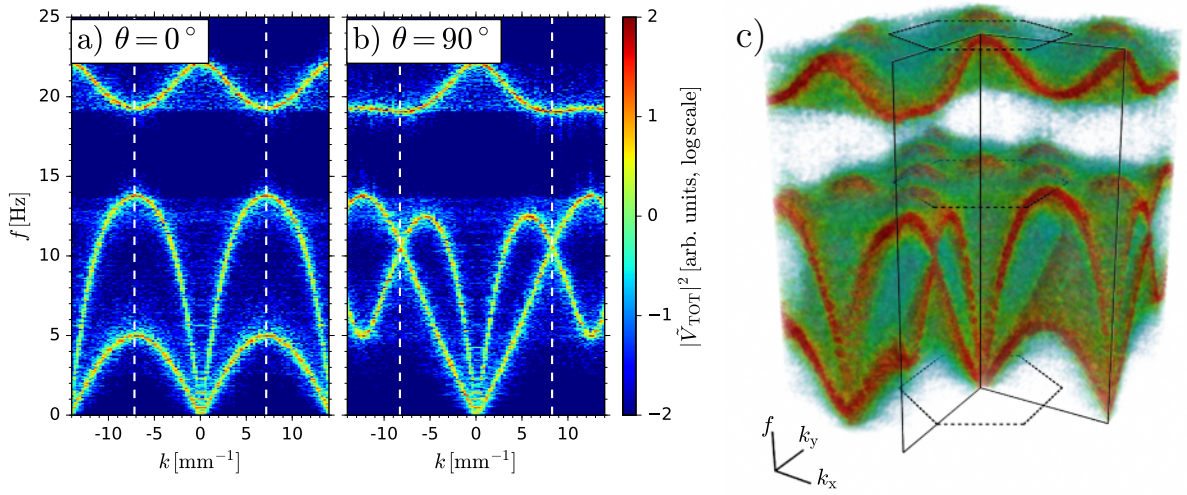

Figure 1.9: Velocity current fluctuation spectra in the direction denoted by $\theta = 0$ (a) and $\theta = 90°$ (b) for the simulated crystal shown in Fig. 1.8(c). The spectra are shown as a function of wave number k and frequency f. To calculate the spectra, a central region consisting of 1400 particles was analyzed for a period of 28.8 s. To show all three modes, the spectra of the longitudinal, transverse horizontal and transverse vertical currents (see Eq. 1.35) are added up and shown in arbitrary units and logarithmic scale. (c) To visualize the spectra in the three dimensions spanned by k_x, k_y and f, lower intensities are set transparent. The region along the solid lines was cut out in order to offer a clear view on the origin of the k_xk_y-plane. The plot was created with the Mayavi library [112]. Dashed lines indicate the border of the first Brillouin zone.

θ of the wave vector in the plane, as shown in Figs. 1.9(a) and (b). For a visualization in the k_xk_y-plane, the spectra can be calculated for a large number of **k**-vectors and then averaged over a frequency range of interest [85, 88]. A novel way to inspect the spectra in the three-dimensional space spanned by k_x, k_y and frequency f is shown in Fig. 1.9(c), where smaller intensities are made transparent to give view to the larger contributions.

1.3 Aims of this thesis

One aim of this thesis is the analysis of dynamical effects involving nonreciprocal particle interactions in complex plasmas. As one prime example of nonreciprocity effects, the discovery of the mode-coupling instability vastly contributed to the understanding of the dynamics of two-dimensional plasma crystals and was the basis for several theoretical and experimental works [58, 84, 85, 87, 89]. More than 15 years after its discovery, experiments point to new and interesting effects associated with the instability. In Chapter 2, the synchronized motion that was observed experimentally during the asymmetric triggering of the mode-coupling instability [88] will be analyzed. The synchronization is reproduced in MD simulations, which enables an analysis of delicate symmetry-breaking effects in complex

plasmas.

As a second example of nonreciprocity effects, the so-called *channeling* mechanism in two-dimensional plasma crystals will be analyzed in Chapter 3. During the channeling mechanism, an extra particle that is not part of the crystal lattice floats slightly above the crystal and moves with almost constant velocity through a channel formed by the lattice [97, 98]. As a theoretical analysis of the experimental findings has not yet been reported, the mechanism that propels the extra particle and confines it to the crystal channel is studied with simulations and a simple theoretical model.

Finally, in Chapter 4, the Fourier phases of nonlinear time series are investigated. To characterize the nonlinearities, the well-known nonlinear prediction error and recently developed measures from network theory are applied to various nonlinear time series and to surrogate data. Understanding the role of the Fourier phases could considerably increase our knowledge of nonlinear time series. A good understanding of the Fourier phases is also necessary to guarantee the linearity of surrogate data, which otherwise lead to wrong results of statistical tests for nonlinearity.

Chapter 2

Synchronization during the mode-coupling instability

This chapter provides complementary information to the following papers, which appear as Refs. [102] and [113] in this thesis.

> I. Laut, C. Räth, S. Zhdanov, V. Nosenko, L. Couëdel and H. M. Thomas. *Synchronization of particle motion in compressed two-dimensional plasma crystals*, Europhysics Letters **110**, 65001 (2015)
>
> I. Laut, S. K. Zhdanov, C. Räth, H. M. Thomas and G. E. Morfill. *Anisotropic confinement effects in a two-dimensional plasma crystal*, Physical Review E **93**, 013204 (2016)

2.1 Objectives

When one calculates the theoretical dispersion relation in a two-dimensional plasma crystal (see Sec. 1.2.2), one expects all six symmetry directions to be perfectly equivalent, as can be seen in Fig. 2.1(a). In particular, the growth rates of the mode-coupling instability (MCI) should be equally large in the six directions. In contrast to these expectations, Couëdel *et al.* [88] observed a very asymmetric triggering of the MCI in experiments which is shown in Fig. 2.1(b). The onset of the instability was accompanied by a synchronization process: lines of particles were found to oscillate in phase, and in antiphase with the neighboring lines. The intention of the first paper [102] was to understand these synchronization effects by means of MD simulations.

As we will see in the following, under horizontal compression the MCI can be triggered in two or four (out of six) directions. During this asymmetric triggering of MCI, patterns of synchronized motion can be observed. However, two opposite directions, for example $\theta = 0°$ and $180°$ are still equivalent in the theoretical spectra of a compressed lattice. Possible mechanisms leading to a breaking of this symmetry were studied in the second paper [113].

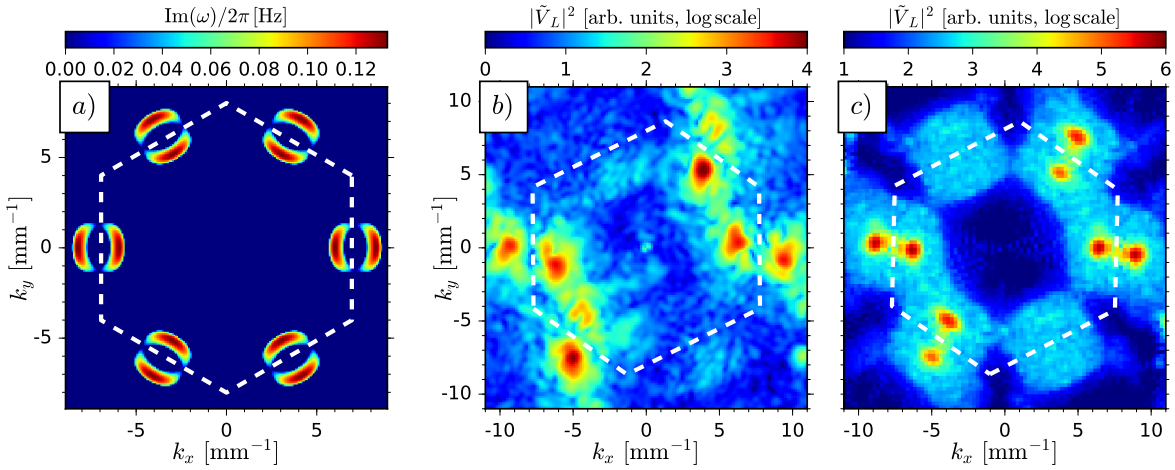

Figure 2.1: (a) Growth rate of the hybrid mode calculated for a perfect hexagonal lattice (see Eq. 1.23) for parameters from Fig. 1.6. (b) Longitudinal particle current fluctuation spectrum (see Eq. 1.35) of the experimental data of Ref. [88]. To visualize the spectra in the $k_x k_y$-plane, the intensity was averaged in the frequency range $14\,\mathrm{Hz} < f < 18\,\mathrm{Hz}$ containing the frequency of the hybrid mode. (c) The same as (b) for the simulation [102].

2.2 Methods

To quantify the deformation of the crystal lattice for the experimental data of Ref. [88], the pair correlation function $g(\mathbf{r})$ in the horizontal plane defined in Eq. 1.32 is considered. The first six peaks of $g(\mathbf{r})$ are fitted to an ellipse centered on the origin. The eccentricity $\epsilon = \sqrt{1 - B_e^2/A_e^2}$ of the ellipse, where A_e and B_e are the major and minor half axes, is a measure for the compression of the crystal, and the tilt angle β between the minor axis and the x-axis denotes the direction of compression.

The synchronization pattern that was observed in Ref. [88] can be described as follows. A line of particles tends to oscillate in synchrony, with a larger oscillation amplitude in the direction perpendicular to the line. The oscillation is in antiphase to the neighboring lines which also oscillate in synchrony, such that a pattern of alternating oscillation is formed. In a hexagonal lattice, the pattern can be oriented in three different directions. A synchronization pattern with the lines along the y-axis and the particles oscillating along the x-axis is sketched in Fig. 2.2. To measure the degree of synchronization in the three directions of the crystal, an orientation-dependent order parameter motivated from the Kuramoto model [114] is proposed. To account for the stripe pattern of alternating phases in complex plasma crystals, a local order parameter is defined as

$$R_{i,\theta}(t) = \frac{1}{\mathrm{N_n}} \sum_{j=1}^{\mathrm{N_n}} \left[k_j \cos(\phi_{j,\theta} - \phi_{i,\theta}) \right], \tag{2.1}$$

where $N_n = 6$ is the number of nearest neighbors in the hexagonal lattice and θ is the angle perpendicular to the stripe pattern. The instantaneous phase $\phi_{i,\theta}(t)$ of particle i is estimated

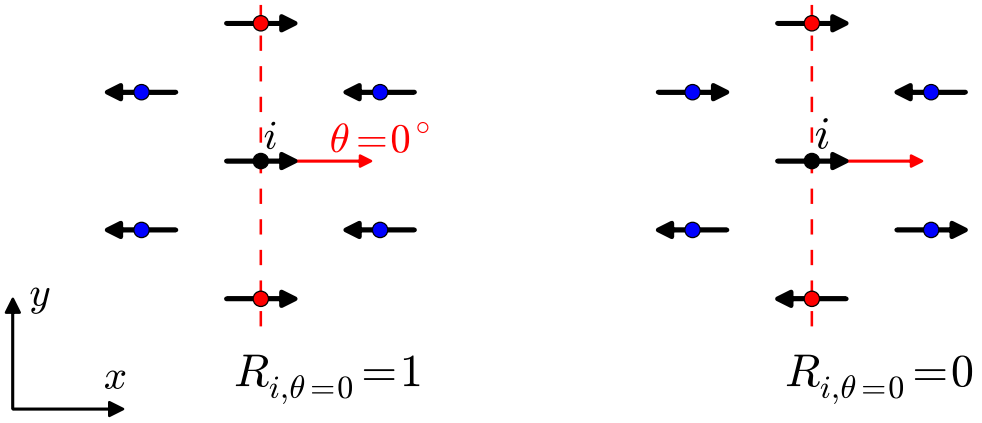

Figure 2.2: Sketch for construction of order parameter. For the calculation of the order parameter in direction $\theta=0$, the two nearest neighbors of particle i along the y-direction (red circles) are associated with a factor $k_j=+1$, while the other particles (blue circles) have $k_j=-1$. Counterdirected arrows stand for a phase shift of π for the particle oscillations. For two different situation, the resulting order parameter for the central particle i is indicated.

from the projection of the horizontal position in the direction θ. The instantaneous deviation from the time average is obtained with a sliding window of length 0.2 s, and the phase is assumed to grow linearly by 2π between each maximum of the deviation. The factor

$$k_j = \begin{cases} +1 & \text{for particles assumed to be on the same line as particle } i \\ -1 & \text{otherwise,} \end{cases} \tag{2.2}$$

determines the sign of the contribution of particle j to the local order parameter. The line with $k_j = +1$ is perpendicular to the direction denoted by the angle θ. As sketched in Fig. 2.2, for $\theta=0°$, for a particle i the two nearest neighbors along the y-direction contribute with a positive factor, while for the other four nearest neighbors, $k_j=-1$. This leads to a maximal order parameter $R_{i,\theta=0}=1$ during a pattern of alternating oscillations as sketched by the arrows in Fig. 2.2(a). When there is no synchronized pattern as in Fig. 2.2(b), the order parameter averages to zero.

Defects were extensively studied in complex plasmas. In a regular hexagonal lattice, all Voronoi cells are sixfold cells; a defect is then a cell with a different number of faces. Defect chains between domains yield information about structural properties [74, 105, 115]. Gliding dislocations, i. e., isolated pairs of one fivefold and one sevenfold cell, can be used as moving perturbations in the crystal [116]. Here we consider the dislocation dipole vector $\mathbf{d} = \mathbf{r}_7 - \mathbf{r}_5$ [117], where $\mathbf{r}_{7,5}$ are the positions of the centers of the sevenfold and fivefold defect cells.

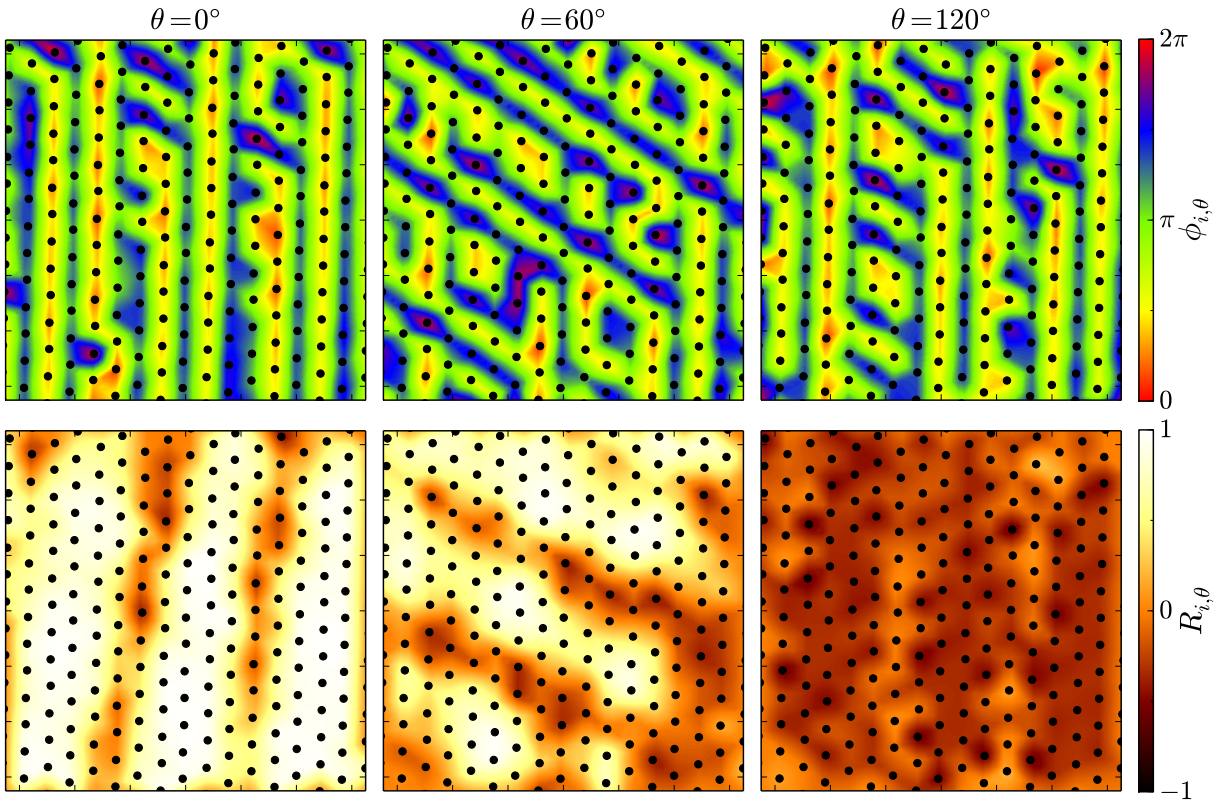

Figure 2.3: Snapshots of the instantaneous phases and the order parameters during asymmetrically triggered MCI in a simulated crystal. Black dots indicate the particle positions. In the upper line, the instantaneous phases $\phi_{i,\theta}$ of the particle oscillations are shown for the three directions $\theta = 0°$, 60°, and 120° at time $t = 23.87\,\mathrm{s}$. In the lower panels, the associated local order local parameter $R_{i,\theta}$ (see Eq. 2.1) is shown. The crystal was compressed horizontally under an angle $\alpha = 30°$ in order to trigger the MCI in the 0° and 60° directions. See the paper [102] for a similar plot of the experimental data.

2.3 Results

By analyzing the pair correlation function $g(\mathbf{r})$ of the experimental data of Ref. [88], a tilt angle $\beta = 27° \pm 2°$ and an eccentricity of $\epsilon = 0.42 \pm 0.07$ were obtained. The crystalline lattice was thus clearly compressed. Reasons for an unwanted compression in experiments can be slight anisotropies in the global horizontal confinement or deformations due to the slow horizontal rotation of the crystal during the experiment.

To reproduce the deformed crystal lattice in simulations, an anisotropic horizontal confinement was considered (see Eq. 1.29) with an angle of $\alpha = 30°$ and horizontal confinement frequencies $f_\parallel = 0.156$ Hz and $f_\perp = 0.137$ Hz. The anisotropic confinement resulted in a deformed lattice; the ellipse fitted to the first peaks of $g(\mathbf{r})$ had a tilt angle of $\beta = 29.7° \pm 0.5°$ and an eccentricity of $\epsilon = 0.36 \pm 0.03$. The longitudinal particle fluctuation spectra, shown

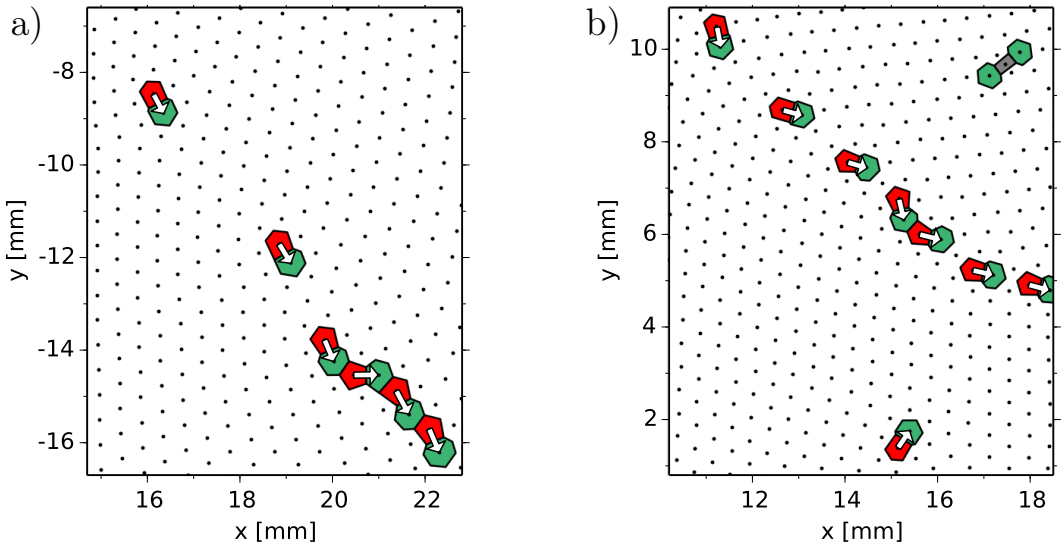

Figure 2.4: Defect patterns for simulated (a) and experimental (b) data. The Voronoi cells of particles having more or less than six neighbors are shown in red for fivefold cells, green for sevenfold cells, and gray otherwise. The dislocation dipole vectors **d** are shown as white arrows. The center of the crystal is located (roughly) at the origin of the coordinate system.

in Fig. 2.1(c), indicate an asymmetric triggering of the MCI in good agreement with the experimental spectra (Fig. 2.1(b)). The compressed crystal lattice allows the MCI to be triggered in the directions $\theta = 0°$ and $\theta = 60°$ (and the two counterdirected directions $\theta = 180°$ and $\theta = 240°$), while in $\theta = 120°$ direction no instability is triggered. Recently, the theory of the asymmetric triggering of the MCI was studied by Ivlev *et al.* by analyzing theoretically the wave modes in a compressed plasma crystal [118].

A snapshot of the instantaneous phases $\phi_{i,\theta}$ of the particle oscillations in the three directions $\theta = 0°$, 60°, and 120° is shown in Fig. 2.3 for the simulated crystal during MCI. The map of $\phi_{i,\theta=0°}$ shows a pronounced pattern with the stripes along the y-direction as can be seen in the upper left panel of Fig. 2.3. The map of the corresponding order parameter of Eq. 2.1 (lower left panel) shows values close to unity for almost all particles in the window. For $\theta = 60°$, the stripes of alternating phases go from the top left to the upper right, and the order parameter indicates that synchronization under this angle is most pronounced in the upper region of the window (upper and lower center panels). Finally, when the horizontal trajectories are projected along $\theta = 120°$, as there is no large amplitude associated to MCI in this direction, the map of the instantaneous phases looks very similar to the case of $\theta = 0°$ (compare upper left and upper right panels). The order parameter $R_{i,\theta=120°}$, however, now shows slightly negative values.

Averaging the local order parameter $R_{i,\theta}(t)$ over all particles i in the central region of the crystal, the time behavior of the synchronization process can be studied. The averaged order parameter $R_\theta(t)$ during the MCI also shows a good agreement of simulations with experiment (see Figs. 2(d) and 3(d) of the first paper [102]): In the directions $\theta = 0°$ and

$\theta = 60°$, the order parameter is positive, while no positive values are obtained in the $\theta = 120°$ direction. At the beginning of the instability in the experiment, $R_{\theta=60°}$ rapidly grows and saturates at $R_{60°} \simeq 0.4$, while in the other direction $R_{0°}$ follows more slowly. The analysis shows that there are two competing synchronization patterns. In the simulation, the dynamics of the order parameters is similar, but the roles of 0° and 60° are interchanged. In addition, in the experiment the intensities in the 60° direction and the counterdirected 240° direction are very different (see Fig. 2.1(b)); a similar, but weaker intensity difference can also be observed in the simulations (see Fig. 2.1(c)).

The theory of wave modes in compressed crystals of Ref. [118] cannot explain such a delicate symmetry breaking. From the asymmetric intensity distribution in Fig. 2.1(c) a net phonon flux can be calculated. In the second paper [113], the direction of this flux was calculated to be in the direction of $\theta = 223°$. Adding a nonvanishing phonon flux in the theoretic calculation of the wave modes indeed reproduces the broken symmetry as can be seen in Figs. 3(d) and 3(e) of the paper [113].

One possible reason for the net phonon flux is phonon scattering by the anisotropically distributed defects in the crystal as indicated by a nonvanishing global dislocation polarization vector $\mathbf{D} = \sum \mathbf{d}$. In the simulations, a majority of the polarization vectors $\mathbf{d}$ was oriented outward as can be seen in Fig. 2.4(a). In experiments, only the central region of the crystal is observed in order to have a good resolution. In the experimental data considered in the paper, only one major defect line is visible. As can be seen in Fig. 2.4(b), the dislocation vectors are also loosely oriented away from the central region. For an analysis of the global polarization pattern in experiments dedicated studies with a larger field of view would be necessary. A second possible explanation for the net phonon flux is the umklapp scattering which can also happen in a perfect, dislocation-free crystal lattice.

2.4 Conclusion

This chapter focused on symmetry breaking during the mode-coupling instability. By compressing the crystal lattice horizontally, the MCI can be triggered in two or four directions (depending on the angle of compression), in contrast to the triggering of MCI in a perfect hexagonal lattice where all six directions are equally strong. The asymmetric triggering is accompanied by a synchronization pattern or a competition of patterns, which can be characterized by a direction-dependent order parameter.

By repeating the simulations but only taking the *linearized* interparticle interactions into account, it is possible to discriminate the linear and the nonlinear contributions to the synchronization process. As it is common belief that nonlinear terms are necessary for synchronization to occur, studying synchronization in such a linearized model of the MCI could show that nonreciprocal—but linear—interactions are sufficient, and shed light on the profound properties of synchronization processes [119].

The intensity difference of the MCI in two opposite directions, observed in experiments and simulations, cannot be described by a mere deformation of the crystal lattice. With

anisotropic phonon scattering at defects and umklapp processes two mechanisms were proposed that could be responsible for the net phonon flux which in turn leads to the broken symmetry.

In the first experiments with the new large-diameter plasma chamber that is currently built and tested in the research group, the experimental fluctuation spectra reveal a coupling of modes far away from a triggering of the MCI [120]. This coupling of modes can only be explained by the influence of strongly nonreciprocal interactions. It is a challenge for further studies to understand the (nonlinear) effects leading to this non-resonant coupling of the modes.

Chapter 3

Self-propelled motion of an extra particle

This chapter provides complementary information to the following paper, which appears as Ref. [121] in this thesis.

> I. Laut, C. Räth, S. Zhdanov, V. Nosenko, G. Morfill and H. Thomas.
> *Wake-mediated propulsion of an upstream particle in two-dimensional plasma crystals*, Physical Review Letters **118**, 075002 (2017)

3.1 Objectives

In 2012, Du *et al.* observed the intriguing motion of an upstream extra particle moving above the lattice of a two-dimensional plasma crystal [97]. "Extra" means that the particle was not part of the two-dimensional crystal lattice and "upstream" means that the downward ion flow passes by the particle before reaching the crystal. As shown in Fig. 1.7, the particle followed the channel formed by lines of neighboring particles and thus moved in a straight line through the crystal. What is more, the motion of the extra particle was not dampened despite ambient gas friction. It was assumed that the persistent motion was a result of the nonreciprocity of the particle interaction [97, 98], but the exact propulsion mechanism was not explained. The objective of the present work was to reproduce the channeling effect in simulations and study the underlying mechanism in greater detail.

3.2 Methods

To reproduce the channeling effect, the equation of motion Eq. 1.27 is initially integrated for $N-1$ particles in order to equilibrate the two-dimensional crystal. The crystal is oriented such that the crystal forms channels along the x-direction. After equilibration, the Nth particle, termed extra particle, is added to the crystal at $t=0$. Its initial velocity $\mathbf{v}(t=0) = v_0\mathbf{e}_x$ is oriented in the x-direction. In the experiments, the extra particle was

found to be slightly smaller than the other particles [97], which is the reason for the different levitation height of this lighter particle. In the simulations, the vertical confinement of the extra particle is assumed to have its minimum at a distance h above the crystal, the vertical confinement force then reads

$$\mathbf{C}_{i,z} = \begin{cases} -M\Omega_z^2(z_i - h) & \text{for } i = N, \\ -M\Omega_z^2 z_i & \text{otherwise.} \end{cases} \tag{3.1}$$

The terms for horizontal confinement, the interaction force (see Eq. 1.22) and the Langevin heat bath (see Eq. 1.31) are identical for the extra particle and the other particles.

Simulations with different horizontal confinement wells are considered. The simulations with a parabolic confinement well (see Eq. 1.28) resemble well the experiments. As the interparticle distance increases from the center of the crystal outward, the channels are bent and, therefore, the extra particle slightly changes its direction during the channeling process. The simulations with a tenth-order horizontal confinement well (see Eq. 1.30) produce very regular crystals which enable a detailed analysis of the driving mechanism.

The simulation parameters were chosen to be close to the experimental conditions of Ref. [97]. The crystal consisted of $N = 10\,001$ particles, each of mass $M = 6.1 \times 10^{-13}$ kg and charge $Q = -18500e$. The screening length was $\lambda = 380$ μm. The wake charge q and its distance δ are not known in experiments and are treated as free parameters; they were set to relatively large values $q = 0.6|Q|$ and $\delta = 0.4\lambda$. If not stated otherwise, the friction coefficient was $\nu = 1.26$ s^{-1}. The parameters of the confinement were $\Omega_z = 2\pi \times 22$ s^{-1}, $h = 350$ μm, $\Omega_h = 2\pi \times 0.12$ s^{-1} and $R = 27$ mm. Thus confined, the equilibrium interparticle distance was $a = 511 \pm 5$ μm for the parabolic confinement and $a = 505 \pm 2$ μm for the tenth-order horizontal confinement.

3.3 Results

Trajectories of the extra particle in crystals with parabolic and tenth-order horizontal confinements are shown in Fig. 3.1. In both cases, the extra particle had an initial velocity of $v_0 = 10$ mm/s. The extra particle initially accelerates to larger velocities. For the crystal confined in a parabolic confinement (Fig. 3.1(a)), the channel lines are bent and the extra particle follows the lines, similarly to the experimental observation of Ref. [98]. The channeling is accompanied by a zig-zag motion as it bounces from one side of the channel to the other; this behavior is also in good agreement with experiments [97].

The trajectory of the extra particle is a straight line with barely noticeable zig-zag motion in the case of the tenth-order horizontal confinement (Fig. 3.1(b)). We show in the paper that in such a homogeneous crystal, extra particles with different initial velocities obtain the same terminal velocity $v_s = 20.5 \pm 0.3$ mm/s. The influence of the extra particle on the particles forming the channel, termed the *channel particles* in the following, can be analyzed in detail for this idealized case. It can be seen from Fig. 3.1 that the channel particles are dragged towards the extra particle during its passage and subsequently perform

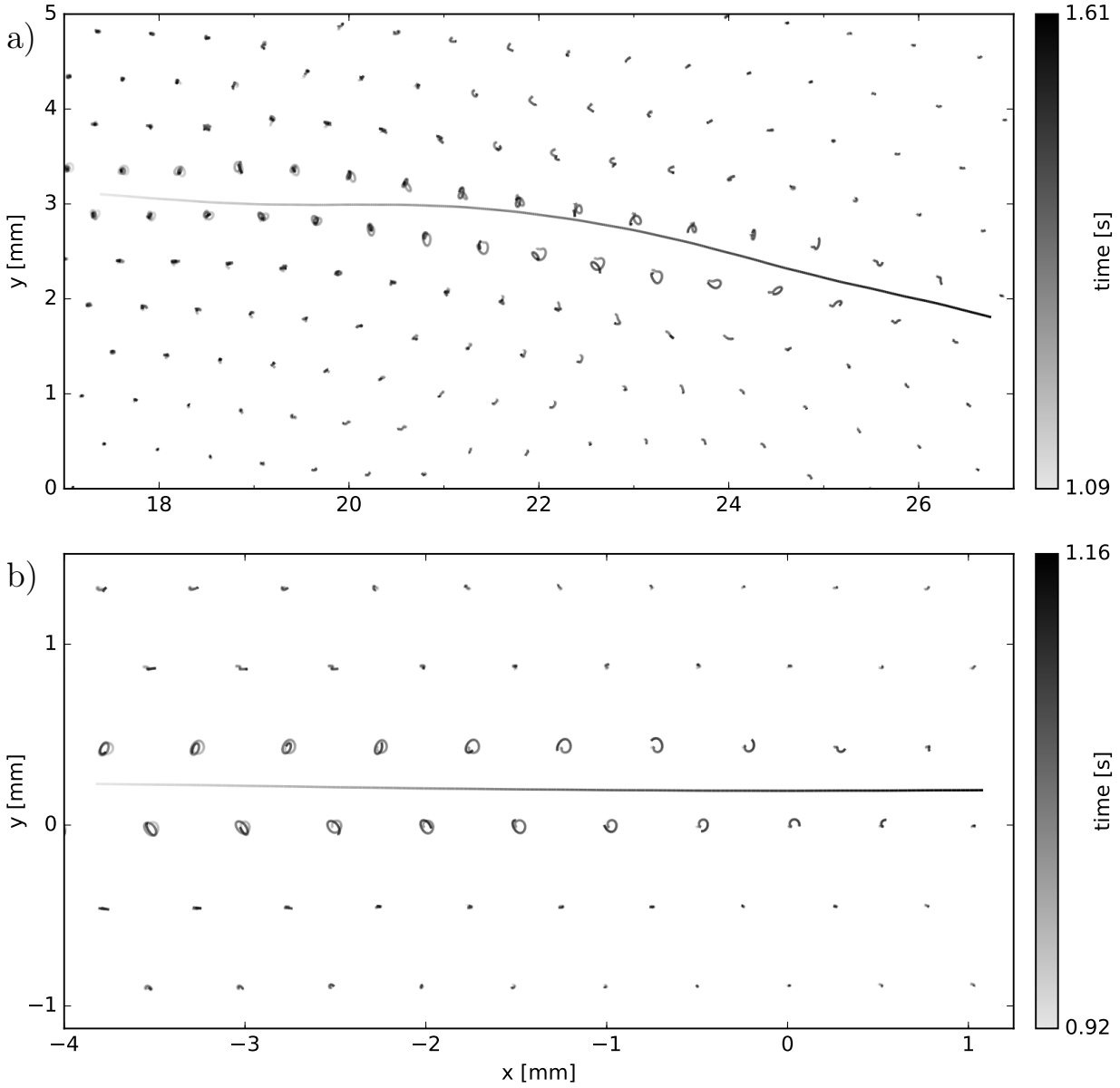

Figure 3.1: Trajectories of upstream extra particles in the simulation. The horizontal trajectories of the particles are color coded with respect to time. In (a), the horizontal confinement is parabolic, in (b) the horizontal confinement is of tenth order.

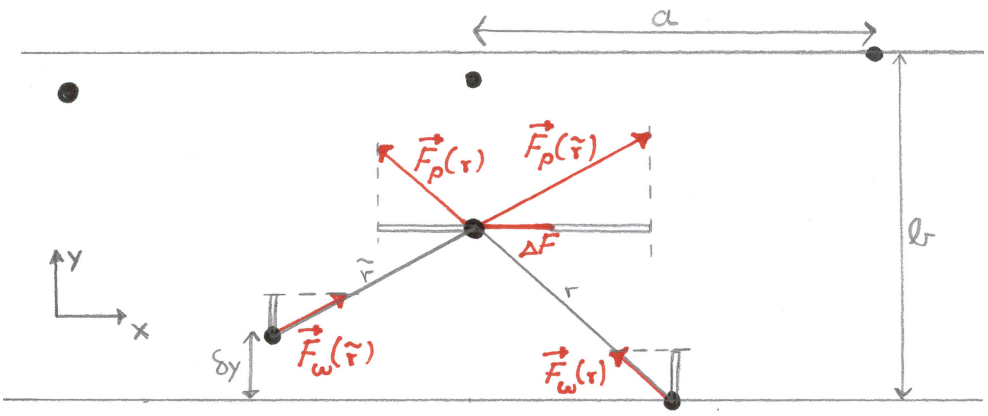

Figure 3.2: Sketch of the propulsion mechanism of the extra particle. The horizontal particle positions are shown by black dots. As the extra particle (central dot) moves above the channel from left to right, the particles forming the channel are displaced towards the extra particle by δy, leading to a different distance before (r) and after ($\tilde{r}$) the passage of the extra particle. While the y-component of the attractive force $\mathbf{F}_w$ towards the wake of the extra particle varies only weakly with δy, the x-component of the repulsive force $\mathbf{F}_p$ exerted on the extra particle is by ΔF larger after the passage, leading to a net propelling force.

an oscillatory motion. Note that in the reference frame of the extra particle, the channel is significantly deformed (see Fig. 1(b) of the paper [121]): it contracts closely behind the extra particle. Similar channel deformations caused by the upstream extra particle were recorded in experiments [97, 98].

A theoretical model interpreting the channel deformation and explaining the propulsion process observed in experiments and simulations can be described as follows. We assume that as the extra particle floats above the crystal, the force exerted on the channel particles is mainly attractive since the extra-particle wake is close to the crystal layer. The force exerted by a channel particle on the extra particle is, however, repulsive as the extra particle is at a greater distance from the wake of the channel particle. The forces involved in the propulsion process are sketched in Fig. 3.2, where the interaction force of Eq. 1.22 is decomposed in the repulsive particle-particle term $\mathbf{F}_p$ and the attractive wake-particle term $\mathbf{F}_w$.

The displacement δy of the channel particle in y-direction can be estimated from the y-component of the attractive force $\mathbf{F}_w$. In the situation sketched in Fig. 3.2, the distance vector from the channel particle to the wake of the extra particle is $\mathbf{r}_w = (a/2, b/2, h-\delta)$, where $b = \frac{\sqrt{3}}{2}a$ is the channel width. Assuming the attractive force to be constant in the range $-a/2 < \Delta x < a/2$, where $\Delta x = x - x_e$ is the distance from the extra particle in x-direction, we obtain

$$\delta y \approx \frac{F_w(r_w)}{r_w} \frac{ba^2}{4Mv_s^2}. \tag{3.2}$$

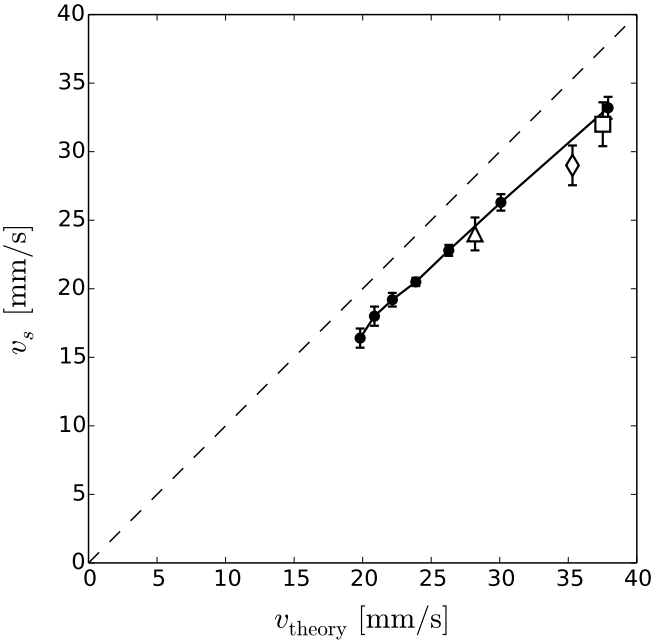

Figure 3.3: Observed terminal velocity of the extra particle v_s as a function of the predicted value v_{theory}. The values for simulation runs with different friction rates are given by the solid symbols and connected by a line. The values for the experiments of Ref. [97] are shown by open symbols. □: Experiment 1. △: Experiment 3. ♢: Experiment 5. Experiments 2 and 4 of Ref. [97] involved downstream particles and are not considered. The diagonal corresponding to a perfect agreement of observation and theory is shown as a dashed line.

The propelling force $\Delta F = \frac{F_p(\tilde{r})}{\tilde{r}}\frac{a}{2} - \frac{F_p(r)}{r}\frac{a}{2}$ stems from the asymmetry of the repulsive particle interactions before and after the passage, where $\mathbf{r} = (a/2, b/2, h)$ and $\tilde{\mathbf{r}} = (a/2, b/2 - \delta y, h)$ is the distance to the channel particle that was displaced by δy. The propelling force can then be estimated as

$$\Delta F \approx \delta y \left[\frac{\partial}{\partial\, \delta y} F_p(\tilde{r}) a/2\tilde{r}\right]_{\delta y = 0}, \tag{3.3}$$

and equating ΔF with the friction force $F_{\text{fric}} = M v_s \nu$, one can solve the equation for $v_s \equiv v_{\text{theory}}$, yielding

$$v_{\text{theory}} \approx \sqrt[3]{\xi(r)\frac{F_p(r)}{r^3}\frac{F_w(r_w)}{r_w}\frac{b^2 a^3}{16 M^2 \nu}}, \tag{3.4}$$

where the term $\xi(r) = (3 + 3r/\lambda + r^2/\lambda^2)/(1 + r/\lambda)$ stems from the derivative of the Yukawa force with respect to δy.

For the simulation with $\nu = 1.26\ \text{s}^{-1}$, Eq. 3.4 yields $v_{\text{theory}} = 23.9$ mm/s, which overestimates the observed velocity v_s by about 17%. In Fig. 3.3, the terminal velocity is compared to the predicted value for simulations with different friction values in the range $0.32\ \text{s}^{-1} < \nu < 2.21\ \text{s}^{-1}$. The simple model of Eq. 3.4 shows a good agreement for all simulations, as it always only slightly overestimates the terminal velocity by a factor of

about 15–20 %. For friction rates above $\nu = 2.21$ s^{-1}, the propulsion mechanism was not observed and the extra particle was decelerated by the friction force, while for $\nu < 0.32$ s^{-1} the extra particle was so fast that it was not possible to determine whether the velocity saturated at a constant value before reaching the boundary of the crystal.

Equation 3.4 can also be applied to experiments. The wake parameters are not known in experiments, but one can assume that they are similar to the simulations that reproduce the propulsion mechanism. In Fig. 3.3 are also shown the predicted velocities for the experiments of Ref. [97], where the dimensionless wake parameters were taken as $q/|Q| = 0.6$ and $\delta/\lambda = 0.4$ as in the simulations and all other parameters (including Q and λ) were taken from Ref. [97]. The extra-particle velocities from the experiments are within the velocity range that is accessible in the simulations. Here again, Eq. 3.4 yields good results, only slightly overestimating the observed velocity v_s.

A possible reason for the discrepancy between the observed and predicted terminal velocity of the extra particle is that the particle-particle repulsion is not considered when estimating the wake-mediated displacement δy.

Reproducing the channeling effect in simulations also enables a detailed study of the impact of the extra particle on the crystal. Suitable tools are the visualization of density variations and the particle current fluctuation spectra. Both are shown in Fig. 3.4 for three simulations with different friction rates $\nu = 0.63$, 1.26, and 2.21 s^{-1}. For the largest friction rate (upper panels of 3.4), the extra particle obtains a terminal velocity of $v_s = 16.4 \pm 0.7$ mm/s. For this rather slow perturbation, the subsonic lateral wakes [95] propagate almost in the same direction as the extra particle. In front of the extra particle, the particle density is slightly increased. From the fluctuation spectra it can be seen that in this case of a subsonic extra particle the straight line corresponding to the extra-particle propagation crosses the longitudinal spectrum at approximately $k = 4$ mm^{-1} (upper right panel of Fig. 3.4). For $\nu = 1.26$ s^{-1} (middle panels of Fig. 3.4), the extra-particle velocity saturates at $v_s = 20.5 \pm 0.3$ mm/s. The crests of the lateral wakes are no longer straight lines but bent outwards from the extra particle. From the slopes of the straight line and the longitudinal spectrum at small k it can be seen that v_s is close to the sound speed $c_l = 23 \pm 1$ mm/s in the crystal. Finally, for a small friction rate $\nu = 0.63$ s^{-1} (lower panels of Fig. 3.4), the extra-particle velocity $v_s = 26.3 \pm 0.6$ mm/s exceeds the sound speed and a Mach cone forms in front of the particle. The predicted Mach cone is shown that obeys the well-known relation

$$\sin \mu = \frac{c_l}{v_s} \equiv \frac{1}{M}, \tag{3.5}$$

where μ is the half cone angle and M the Mach number. The predicted cone angle agrees well with the measured density variations. The Mach number is calculated to be $M = 1.14$.

For subsonic extra-particle velocities (upper right panel of Fig. 3.4), the longitudinal spectrum of the crystal has a higher intensity near the intersection point with the straight line associated to the movement of the extra particle. For the supersonic case (lower right panel of Fig. 3.4), the increased intensity can only be seen for very small values of wave vector k. In this case, however, an increased intensity can be clearly seen at $f \simeq 20$ Hz where the vertical mode of the crystal is located. The increased intensity of the *longitudinal*

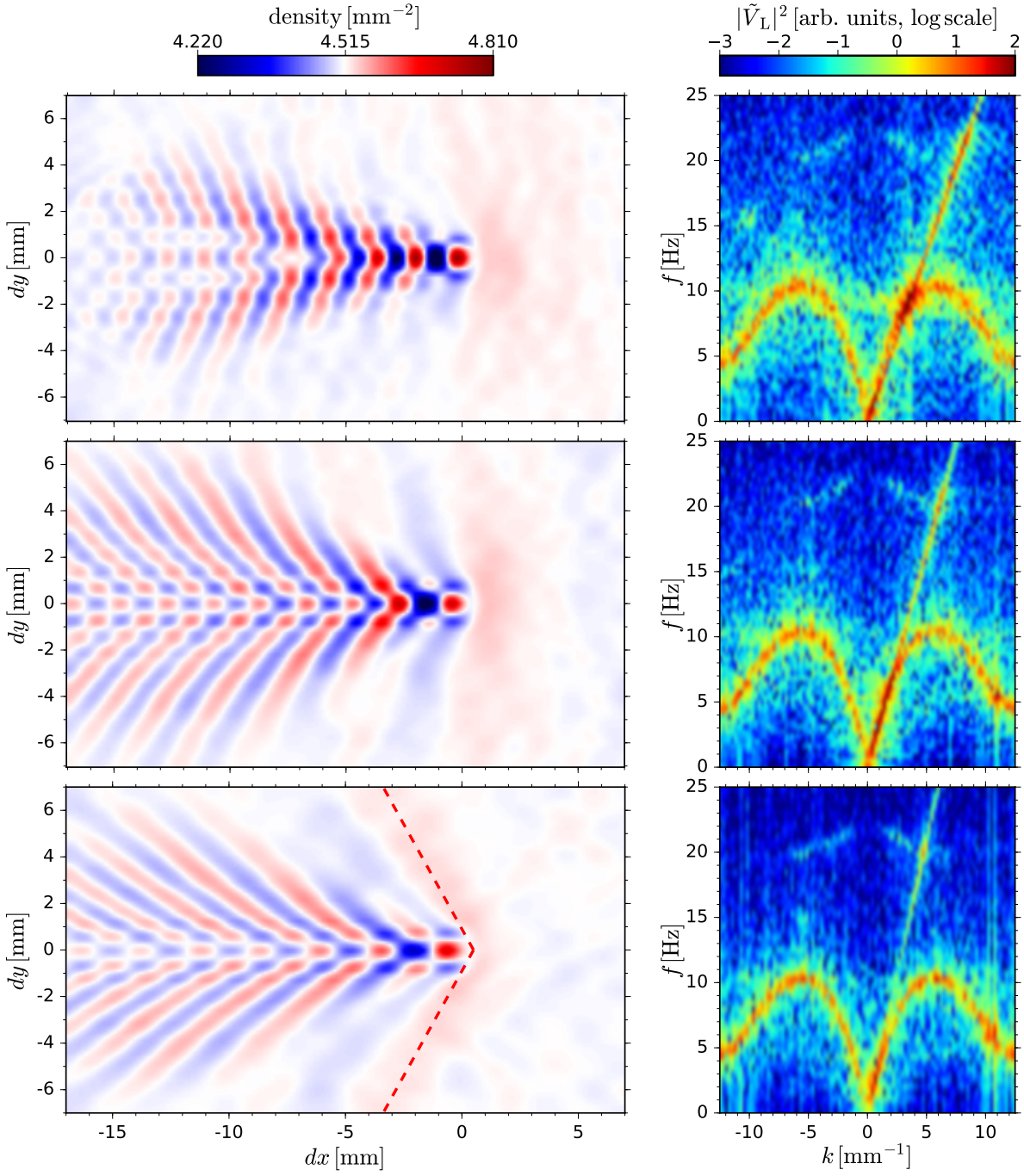

Figure 3.4: Waves excited by the extra particle for different friction rates. In the left panels, the density variation in the crystal plane is shown in the reference frame of the extra particle. In the right panels, the longitudinal mode of the particle current fluctuation spectra are shown. Upper panels: $\nu = 2.21$ s^{-1} resulting in a terminal velocity $v_s = 16.4 \pm 0.7$ mm/s. Middle panels: $\nu = 1.26$ s^{-1} and $v_s = 20.5 \pm 0.3$ mm/s. Lower panels: $\nu = 0.63$ s^{-1} and $v_s = 26.3 \pm 0.6$ mm/s.

mode at frequencies where the *vertical* mode is located hints to a resonant coupling of these two modes [122].

3.4 Conclusion

By reproducing the propulsion process of an extra particle in simulations with the pointlike wake model, we obtained insight into the physical processes involved. The nonreciprocal interaction due to the ion wake plays a crucial role in the process. Due to the different levitation heights of the extra particle and the channel particles, the nonreciprocity is so strong that the pairwise interaction is attractive for one particle, and repulsive for the other particle. The simple analytical model that was derived from an idealized channel geometry can also be applied to experiments.

The field of active particles [123] has recently attracted much attention and it would be interesting to study the dynamics of extra particles under this perspective. The limiting case of many extra particles on a two-dimensional plasma crystal corresponds to a bilayered system with wake-mediated interactions that is studied in simulations in Ref. [124] where, however, the two layers consisted of particles of opposite charge. It would be interesting to study if the model equations of Ref. [124] also support a mixed state where one layer is active while the other layer is in an inactive crystalline order.

As further applications, the spontaneous emergence of extra particles in the crystal could also be studied in the simulations. The dust particles in experiments are not perfectly monodisperse, and lighter particles naturally have a slightly elevated vertical position in the horizontal lattice. It is possible that the illumination laser exerts a strong enough push on such a lighter particle to remove it from the crystal and let it float above the crystal plane where it is accelerated by the propulsion process described in this chapter. Reproducing the onset of the extra-particle motion in simulations would enable a better control on the generation of extra particles in experiments.

The interactions of the extra particle with defects in the crystal, or even with other extra particles, are natural candidates for further studies. The interference patterns created by two supersonic particles in a two-dimensional plasma crystal were studied recently in Ref. [125], where the particles were driven artificially at a constant velocity. The internal propulsion mechanism of upstream extra particles enables a more detailed study of the interaction of such particles.

Chapter 4

The role of Fourier phases in nonlinear time series

This chapter provides complementary information to the following papers, which appear as Refs. [126] and [127] in this thesis.

> C. Räth and I. Laut. *Time series with tailored nonlinearities*, Physical Review E **92**, 040902(R) (2015)
>
> I. Laut and C. Räth. *Surrogate-assisted network analysis of nonlinear time series*, Chaos **26** 103108 (2016)

4.1 Objectives

The analysis of the Fourier phases is a relatively small subfield of time series analysis despite their great influence on the outcome of nonlinearity measures. In Refs. [128, 129], the evolution of the Fourier phases of astronomical data was studied, stressing their important role to fully characterize a non-Gaussian field. Phase correlations were also found for the cosmic microwave background [130, 131]. The randomness of the Fourier phases as a warrant for nonlinearity is the basis of surrogate data, see Sec. 1.1.4. As was shown in Räth *et al.*, the rank ordered remapping steps of the AAFT and IAAFT schemes can induce nonlinearities in surrogates and lead to a nondetection of weak nonlinearities in the original time series. Nevertheless, IAAFT surrogates are still widely used, see, e. g., Refs. [132–137].

The first objective of this chapter is a detailed analysis of the impact of correlations in the Fourier phases of time series and surrogate data. Insight can be gained either by artificially correlating subsequent Fourier phases or by comparing different surrogate generating mechanisms that are known to induce phase correlations. The two different strategies are followed in the two papers of this chapter.

In 1997, Schreiber and Schmitz compared various nonlinearity measures [138]. They found that the nonlinear prediction error had the best overall performance for a broad

range of applications. Since then, a number of new measures were proposed, most of which are based on network theory [18–21], but a detailed comparison is lacking. Thus, a second objective of this chapter is a comparison of the new network measures and the well-known nonlinear prediction error. For a thorough analysis, both synthetic and real-world data sets are considered. Since the nonlinearity measures are based on surrogate data sets, the two objectives of this chapter are tightly connected.

4.2 Methods

Correlations in the Fourier phases can be visualized and analyzed with the help of phase maps. In a phase map, the Fourier phases $\{\phi_k\}$ are plotted against the phases $\{\phi_{k+\Delta}\}$ shifted by a mode shift Δ in a square of side length 2π [139]. For a linear time series, the set of $\{\phi_k\}$ are independent and uniformly distributed, and thus scattered uniformly in the square. Correlations in the phases appear as diagonal stripes in the phase maps, which indicates that the phases contain nonlinear information about the time series.

One way to quantify the correlation in the phase maps is to calculate the cross correlation between $\{\phi_k\}$ and $\{\phi_{k+\Delta}\}$,

$$c(\Delta) = \frac{\langle \phi_k \phi_{k+\Delta} \rangle}{\sigma(\{\phi_k\})\sigma(\{\phi_{k+\Delta}\})} \,. \tag{4.1}$$

The average is performed over all possible pairs of shifted phases. c is normalized by the standard deviation of the phases, $\sigma(\{\phi_k\})$.

As discussed in Sec. 1.1.4, the rank-ordered-remapping step of AAFT and IAAFT surrogates can introduce phase correlations. The Fourier phases ϕ_k and $\phi_{k+\Delta k}$ can also be correlated artificially by the iterative scheme suggested in the paper [126]

$$\phi_{k+\Delta k} = \phi_k + d\phi + \eta, \quad k = k_s,\, k_s + dk,\, k_s + 2\,dk,\, \ldots \,, \tag{4.2}$$

where $d\phi$ is a constant phase shift and η is a Gaussian noise with standard deviation σ_η. The iteration starts at k_s and continues with a step size of dk.

In order to analyze the impact of phase correlations on the outcome of a test for nonlinearity, the time series under study are embedded (see Eq. 1.2) and analyzed with different (static and dynamic) measures (see Sec. 1.1.3). In the case of the nonlinear prediction error, one expects the values for a nonlinear time series to be smaller than those of the surrogate data. When analyzing surrogate schemes that can possibly contain spurious nonlinearities, it is sensible to calculate the *signed* significance (as compared to the definition in Eq. 1.14)

$$S^{\pm}(M) = \pm \frac{M - \langle \{M_s\} \rangle_s}{\sigma(\{M_s\})}. \tag{4.3}$$

The test with the nonlinear prediction error $S^{-}(\mathcal{E})$ is then also sensible to nonlinearities in surrogate data by showing less significant or even negative significances. Similarly, one expects larger values of the average connectivity κ for the recurrence network of a nonlinear

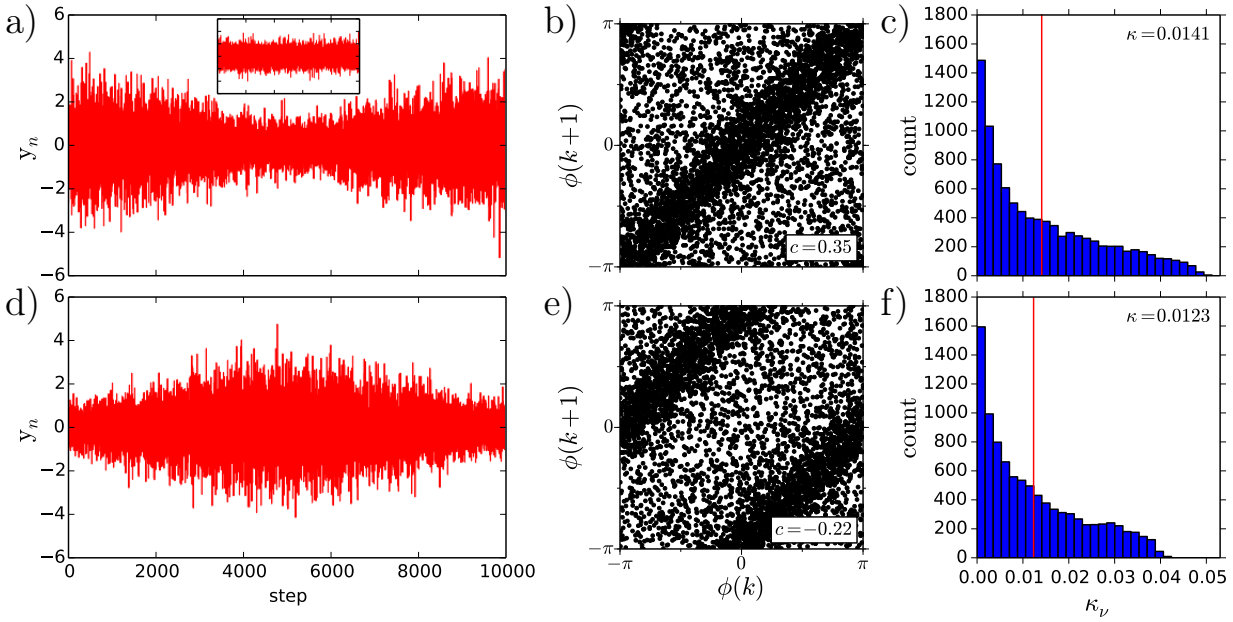

Figure 4.1: Time series with artificial phase correlations. (a) Equation 4.2 with $\Delta k = 1$ and $d\phi = 0$ applied to the original time series (shown in the inset) consisting of 10000 Gaussian random numbers. (b) Phase map for $\Delta = 1$; the cross correlation c is indicated in the panel. (c) Histogram of the degree centrality κ_ν of the recurrence network. The embedding parameters were $\tau = 250$ steps and $d = 3$. The threshold $\epsilon = 0.4768$ was chosen that the average connectivity for the original time series is $\kappa_{\text{or}} = 0.01$. The average connecitivty κ is indicated by the red line and shown in the top right corner of the panel. (d)–(f): The same for $d\phi = \pi$.

time series if the underlying attractor is well reproduced by the embedding. In this case, the signed significance $S^+(\kappa)$ is considered. Finally, for the symbolic network, identical links between the symbols can be expected for the quasi-periodic orbits on the attractor of a nonlinear time series, leading to a smaller average degree k. The signed significance is thus calculated as $S^-(k)$ for the symbolic networks.

4.3 Results

In the first paper [126], nonlinear time series with artificial phase correlations were produced by correlating every pair of successive Fourier phases. This was achieved by applying the scheme of Eq. 4.2 with $\Delta k = 1$, $dk = 2$, and $k_s = 1$ to an initially linear time series of Gaussian random numbers. The width of the noise term was $\sigma_\eta = 1$. The resulting time series is shown in Fig. 4.1(a) for a phase shift of $d\phi = 0$. It can be seen that after this simple scheme, the larger amplitudes of the time series are concentrated at the beginning and the end of the time series. The phase map for $\Delta = 1$ (Fig. 4.1(b)) shows the increased density at the diagonal as could be expected from the scheme; the cross correlation has

a value of $c = 0.35$. As one example for a nonlinearity measure, the distribution of the degree centrality κ_ν for the recurrence network (see Sec. 1.1.3) is shown in Fig. 4.1(c). The threshold ϵ was chosen such that the average connectivity of the initial Gaussian time series shown in the inset is $\kappa = 0.01$. The concentration of the lower amplitudes in the middle of the generated time series leads to a more connected recurrence network and a larger value of $\kappa \simeq 0.0141$.

A time series for $d\phi = \pi$ is shown in Fig. 4.1(d). Here, the larger amplitudes are now concentrated in the middle of the time series leading to an average connectivity of the recurrence network $\kappa \simeq 0.0123$ that is still larger than for the original time series, but slightly smaller than for the time series with $d\phi = 0$ (see Fig. 4.1(f). The cross correlation in the phase map is now negative, $c = -0.22$. In the paper [126] we showed that there is a significant correlation between c and κ, and an anticorrelation between c and the nonlinear prediction error. As $d\phi$ controls the position of the regions with higher and lower fluctuations in the time series, we can now get a detailed understanding of how the phase correlations influence the measures for nonlinearity. The embedding leads to a truncation of the last part of the time series. Depending on whether the remaining time series has smaller ($d\phi = 0$) or larger ($d\phi = \pi$) fluctuations, one obtains a larger or smaller value of the degree centrality κ of the recurrence network, leading to a correlation between c and κ. Similarly, lower fluctuations in the time series lead to a larger prediction error and vice versa, resulting in an anticorrelation of c and the nonlinear prediction error. The artificial phase correlations thus have a direct impact on the measures for nonlinearity.

Applying the scheme of Eq. 4.2 multiple times on an initial time series with different parameters Δk, dk and $d\phi$, it is possible to create a nonlinear time series which has the typical intermittent properties observed in turbulent systems and economic data such as stock prices. We showed that power-law scaling could be found in both the amplitude distribution and a distribution of the volatility $v_n = \sum_{l n=n}^{n+N-1} |y_n|$ that indicate the *fat tails* and the volatility clustering, respectively [126]. Artificially correlating Fourier phases in time series can thus increase our knowledge of the interplay of the Fourier phases on the one hand, and the nonlinear properties of a time series on the other hand.

In the second paper [127], the role of the Fourier phases was studied with the aid of different surrogate generating mechanisms, some of which are known to induce phase correlations (see Sec. 1.1.4). Figure 4.2 shows the time evolution, phase maps and degree centrality for two IAAFT surrogates of an astrophysical time series. The time series, an X-ray light curve from the active galactic nucleus Mrk 766 [140] was chosen because such relatively short and noisy data are well suited to compare different tests for nonlinearity. In contrast to Fig. 4.1, where the phase correlations were artificially added to the data, the correlations shown in 4.2(b) and (e) stem from the iterative scheme of the surrogate generating algorithm. Again, the cross correlation c of the phase map is correlated with the measures for nonlinearity. We showed in the second paper that AAFT and IAAFT surrogates detect no nonlinearities for different light curves where the FT surrogates (which are guaranteed to have no phase correlations) already show significant results [127].

When considering the signed significance test (Eq. 4.3) in Fig. 4.3 for the astrophysical time series shown in the inset of Fig. 4.2, it becomes apparent that the IAAFT surrogates

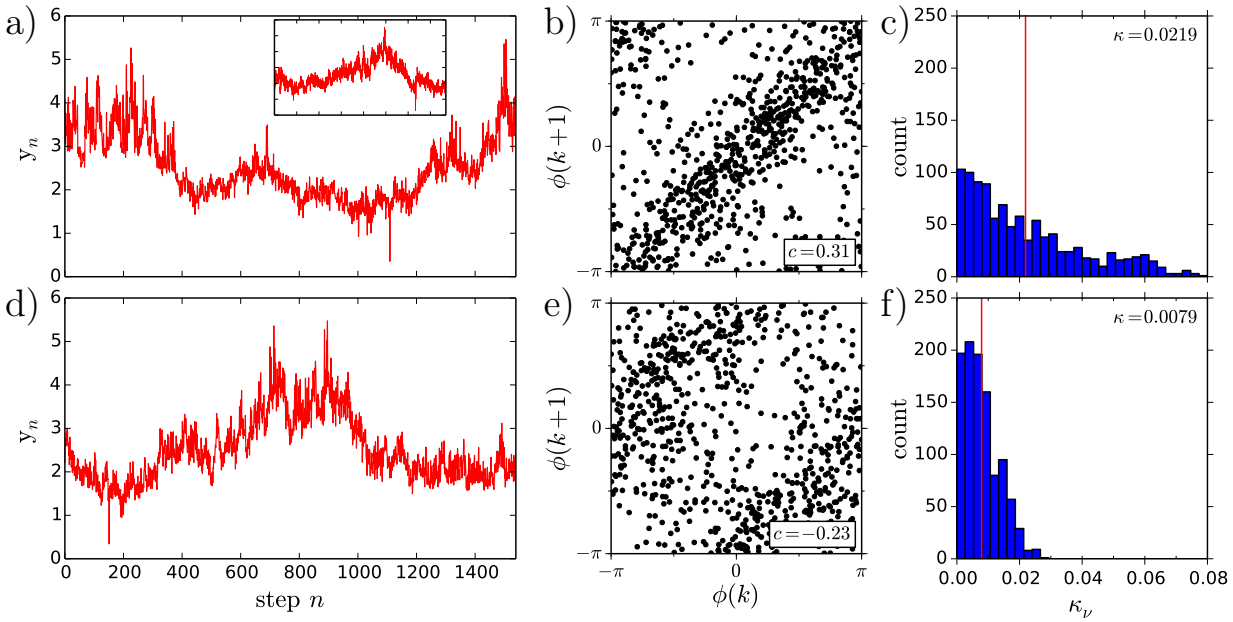

Figure 4.2: Same as Fig. 4.1 but for two IAAFT surrogates of an astronomical time series. Note that while in Fig. 4.1 the phase correlations were introduced artificially, they are here the result of the surrogate generating algorithm.

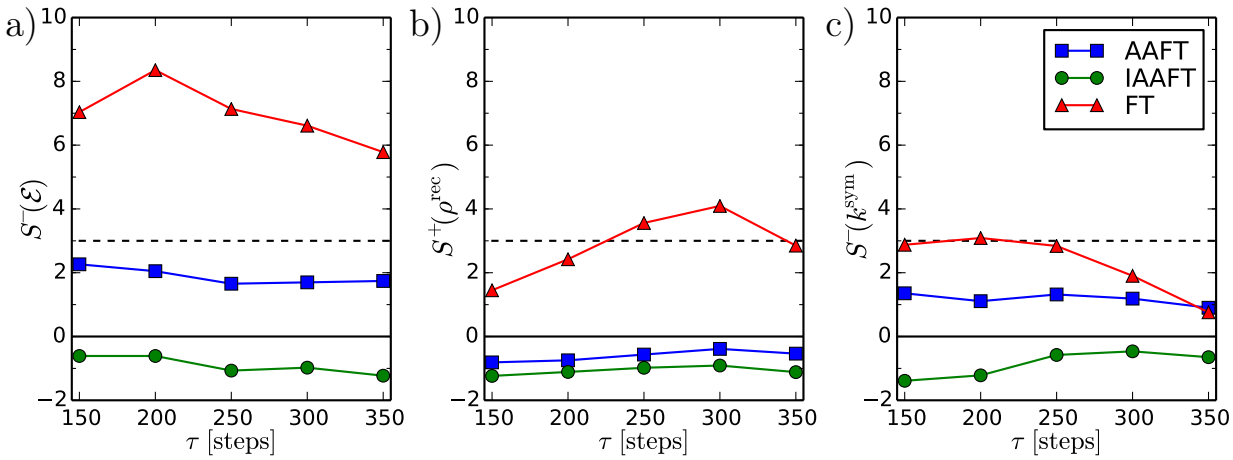

Figure 4.3: Significance of the tests for nonlinearity for the astrophysical time series shown in the inset of Fig. 4.3. (a) For the nonlinear prediction error $\mathcal{E}$, a lead time of 5 time steps was used. The predictor was calculated for the $g = 4$ nearest neighbors. The embedding parameters were $\tau = 250$ time steps and $d = 3$. (b) For the recurrence network, the same embedding parameters were used. The threshold ϵ was chosen such that the $\kappa_{\mathrm{or}} = 0.01$. (c) For the symbolic network, $L = 2$ and $Q = 25$ was used. The 3σ detection limit is shown by a dashed line, and the zero-significance line is shown in black.

not only yield reduced significance values but even negative values for all three measures for nonlinearity, which means the surrogates are found to be *more nonlinear* than the original time series. As measures, the nonlinear prediction error, recurrence networks and symbolic networks were compared. For this particular time series, significant results are only achieved with the FT surrogates; the largest value is obtained for the nonlinear prediction error in Fig. 4.3(a).

The measures for nonlinearity were also applied to artificial data sets in the paper [127]. In order to test both the ability of the measures to detect nonlinearities and the susceptibility to erroneously do so, the nonlinear time series of the Lorenz system $\{x_n\}$ (see Eq. 1.1) are mixed with a linear autoregressive process $\{a_n\}$,

$$a_n = s_n\sqrt{|s_n|}, \quad s_n = cs_{n-1} + \eta_n \tag{4.4}$$

with $c = 0.9$ and noise η_n drawn from a Gaussian distribution. The resulting time series,

$$y_n = m \cdot x_n + (m-1) \cdot a_n, \tag{4.5}$$

then contains a given fraction m of the nonlinear time series. Comparing the performance of detecting nonlinearity as a function of m, the nonlinear prediction error again yielded slightly better results than the network measures.

The increased detection probability of the AAFT surrogates for a linear process (in our case, for $m = 0$) was used in Ref. [27] to argue the advantage of the IAAFT algorithm which indeed shows a lower percentage of false detection. Upon increasing m, we show that the detection of nonlinearity stays at very low values for the IAAFT surrogates (see Fig. 4(a) of the paper [127]). Both amplitude-adjusted surrogate schemes thus have disadvantages: The broadening of the power spectrum with AAFT surrogates can lead to a false detection of nonlinearity in a linear time series, while the iterated rank-ordered-remapping scheme of the IAAFT algorithm introduces nonlinearities in the surrogates that can lead of a nondetection of weak nonlinearities present in the time series.

4.4 Conclusion

Comparing the measures derived from network theory to the nonlinear prediction error for various synthetic and real-world data sets, our conclusion is similar to the one of Schreiber and Schmitz more than 20 years ago: The nonlinear prediction error is a powerful measure with the best overall performance for detecting weak nonlinearities. The more recent network-based measures for nonlinearity show a weaker performance for the artificial and real-world data under consideration. Since the AAFT and IAAFT schemes for generating surrogate data can induce phase correlations that lead to a weaker performance in many cases, we recommend using FT surrogates that are guaranteed to have uncorrelated phases.

Imposing in turn phase correlations artificially by an iterative scheme can deepen our understanding of the role of the Fourier phases in nonlinear time series analysis. After applying the sheme to an initially linear time series, fingerprints of nonlinearity can be

observed. It is conceivable to find a theorem connecting the nonlinear properties of a time series to the Fourier phases, similar to the Wiener-Khinchin theorem (Sec. 1.1.2) connecting the linear properties to the Fourier amplitudes.

Understanding the role of the Fourier phases can increase our knowledge in many fields of physics. In the field of complex plasmas, the analysis of experimental or simulated dynamical effects can help to discriminate the linear and nonlinear mechanisms. In particular, it is interesting to study the dynamics beyond the (linear) theory of the mode-coupling instability and find appropriate theories to model them.

Appendix A

Enclosed papers

Synchronization of particle motion in compressed two-dimensional plasma crystals (Ref. [102])

I. Laut, C. Räth, S. Zhdanov, V. Nosenko, L. Couëdel and H. M. Thomas. *Synchronization of particle motion in compressed two-dimensional plasma crystals*, Europhysics Letters **110**, 65001 (2015) http://dx.doi.org/10.1209/0295-5075/110/65001
©2015 EPLA

A Letters Journal Exploring the Frontiers of Physics

June 2015

EPL, **110** (2015) 65001
doi: 10.1209/0295-5075/110/65001

www.epljournal.org

Synchronization of particle motion in compressed two-dimensional plasma crystals

I. Laut[1(a)], C. Räth[1], S. Zhdanov[2], V. Nosenko[1], L. Couëdel[3] and H. M. Thomas[1]

[1] *Deutsches Zentrum für Luft- und Raumfahrt, Forschungsgruppe Komplexe Plasmen - 82234 Weßling, Germany*
[2] *Max Planck Institute for Extraterrestrial Physics - 85741 Garching, Germany*
[3] *CNRS, Aix-Marseille Université, Laboratoire de Physique des Interactions Ioniques et Moléculaires 13397 Marseille, France*

received 20 April 2015; accepted in final form 19 June 2015
published online 13 July 2015

PACS 52.27.Lw – Dusty or complex plasmas; plasma crystals
PACS 89.75.Kd – Complex systems: Patterns

Abstract – The collective motion of dust particles during the mode-coupling–induced melting of a two-dimensional plasma crystal is explored in molecular-dynamics simulations. The crystal is compressed horizontally by an anisotropic confinement. This compression leads to an asymmetric triggering of the mode-coupling instability which is accompanied by alternating chains of in-phase and anti-phase oscillating particles. A new order parameter is proposed to quantify the synchronization with respect to different directions of the crystal. Depending on the orientation of the confinement anisotropy, mode-coupling instability and synchronized motion are observed in one or two directions. Notably, the synchronization is found to be direction dependent. The good agreement with experiments suggests that the confinement anisotropy can be used to explain the observed synchronization process.

Copyright © EPLA, 2015

Introduction. – Weakly ionized gases containing micron-sized dust particles are called complex (dusty) plasmas. In the plasma the particles charge up and self-arrange enabling the formation of strongly coupled and highly ordered quasicrystalline phases [1–5] (analogous to colloids [6]), called *plasma crystals* [2,7,8]. In ground-based experiments these crystals are typically composed of plastic microspheres that are injected into a plasma created by a radio frequency discharge. The particles charge up negatively and levitate in the plasma sheath region above the lower electrode where they can form a horizontal two-dimensional (2D) monolayer under adequate experimental conditions [2,4]. Many dynamical processes can be studied rigorously in plasma crystals, in particular, linear [9,10] and nonlinear waves [11], resonance effects [12], dynamics of dislocations [13–15] and crystal plasticity [16,17].

As in many physical, astrophysical and biological systems [18], cooperative particle motion is an exceptionally important element of self-organization in complex plasmas. In particular, synchronized motion of particle chains was recently discovered in plasma crystals [19]. Synchronization processes in large systems of oscillators have been studied in chemistry, physics and engineering [20], and the behavior of chirping crickets [21], or superconducting Josephson junctions [22] can be described by the Kuramoto model of globally coupled oscillators [23] which can be solved analytically in a mean-field approach.

In a plasma crystal, the particle-particle interaction is strongly influenced by the surrounding plasma. While the interaction in the bulk plasma is well described by a Yukawa potential [1], the strong ion flow in the plasma sheath region distorts the screening cloud [24,25]. This plasma *wake* below the particles adds an attractive component to the interaction [26] which was described theoretically as a point-like positive effective charge below each particle [27]. Due to the finite vertical confinement of a 2D plasma crystal, there is an out-of-plane wave mode which has an optical dispersion relation in addition to the two in-plane modes with acoustic dispersion. If the vertical confinement is smaller than a critical value, the longitudinal in-plane mode and the out-of-plane mode intersect and form an unstable hybrid mode in the vicinity of the intersection. During this *mode-coupling instability* (MCI), energy is continuously transferred from the flowing ions to the crystal, breaking the crystalline order if the damping rate is small enough [28,29].

(a) E-mail: ingo.laut@dlr.de

Due to the lattice symmetry, MCI in the shallow crossing regime is equally strong in three directions in a perfect hexagonal lattice [29]. In the experiment of ref. [19], however, the instability was dominant in one direction. Synchronized motion of particle chains was observed. The process of synchronization was measured by calculating the Shannon entropy of the instantaneous phases of neighboring particles as well as the distribution of frequencies. In ref. [19], an inhomogeneity of the horizontal confinement was suggested to be a reason for this asymmetry in the crystal, but it was not possible to study the origin of the deformation of the crystal in detail.

The influence of an anisotropy in the horizontal confinement on a rotating plasma crystal was studied in ref. [30]. It was shown that even small anisotropies may considerably affect the dynamical behavior of the system.

In this paper, we demonstrate with simulations that an anisotropy of the horizontal confinement can cause an asymmetric triggering of MCI. At the onset of the instability, synchronized particle motion is characterized by a new order parameter that is sensitive to the direction of the synchronization pattern. Depending on the orientation of the confinement anisotropy, MCI and synchronized motion are observed in one or two directions.

Experiment. – The experiment of ref. [19] will be briefly outlined below. Argon plasma was produced using a capacitively coupled radio frequency discharge at 13.56 MHz with a forward power of 12 W. The microparticles formed a monolayer with mean interparticle distance $a = (480 \pm 10)\,\mu$m. The particle x and y positions were obtained with subpixel accuracy from a top-view camera operating at 250 frames per second. The axes were chosen as depicted in the inset of fig. 1. The gas pressure was reduced from 0.94 Pa to 0.92 Pa to initiate the MCI.

The spectral distribution of particle velocity fluctuations (see eq. (5)) in the $\boldsymbol{k}$-space is highly anisotropic [19]. As can be seen in fig. 2(c), bright "hot spots", the fingerprints of the developed MCI, appear in two directions, in contrast to a perfect hexagonal crystal where the three directions are equally strong [29].

Simulation. – Molecular-dynamics simulations have proven to be an adequate tool to study and compare a wide range of experimental conditions [31–34]. The equations of motion read

$$m\ddot{\boldsymbol{r}}_i + m\nu\dot{\boldsymbol{r}}_i = \sum_{j\neq i} \boldsymbol{F}_{ji} + \boldsymbol{C}_i + \boldsymbol{L}_i, \tag{1}$$

where $\boldsymbol{r}_i$ is the position of particle i, m the particle mass and ν the damping rate.

The force exerted by particle j (and its wake) on particle i is

$$\begin{aligned}\boldsymbol{F}_{ji} = {} & \frac{Q^2}{r_{ji}^2}\exp\left(-\frac{r_{ji}}{\lambda}\right)\left(1+\frac{r_{ji}}{\lambda}\right)\frac{\boldsymbol{r}_{ji}}{r_{ji}} \\ & - \frac{q|Q|}{r_{w_{ji}}^2}\exp\left(-\frac{r_{w_{ji}}}{\lambda}\right)\left(1+\frac{r_{w_{ji}}}{\lambda}\right)\frac{\boldsymbol{r}_{w_{ji}}}{r_{w_{ji}}},\end{aligned} \tag{2}$$

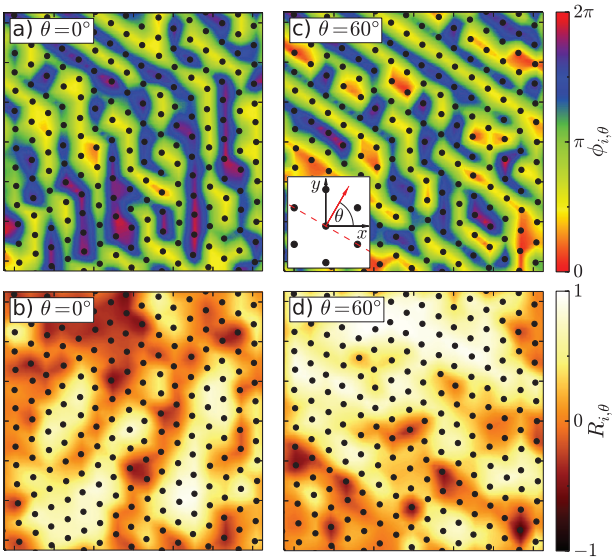

Fig. 1: (Color online) (a) Map of the instantaneous phases $\phi_{i,\theta=0°}$ of the particle oscillations at time $t = 2.5$ s. The particle positions are indicated by black dots. The phases of the particles are interpolated between the particle positions in order to be visualized in a map. Lines of particles with similar phases appear as stripes. The window has a side length 6.5 mm. (b) Map of the order parameter $R_{i,\theta=0°}$ (see eq. (6)) at the same time step. (c), (d): the same for $\theta = 60°$. The inset shows the reference frame. The direction denoted by angle θ is shown as a red arrow, the line perpendicular to it as a dashed line.

where $Q < 0$ is the particle charge, λ is the screening length, $\boldsymbol{r}_{ji} = \boldsymbol{r}_i - \boldsymbol{r}_j$ and $\boldsymbol{r}_{w_{ji}} = \boldsymbol{r}_i - (\boldsymbol{r}_j - \delta\boldsymbol{e}_z)$. To model the ion wake effect a positive "extra charge" q ($0 < q < |Q|$) is added a fixed distance δ ($\delta < \lambda$) below each particle. Note that since in general $\boldsymbol{r}_{w_{ji}} \neq \boldsymbol{r}_{w_{ij}}$, the forces are nonreciprocal due to the ion wake effect. The ion wake (described in detail in [6]) is known to be responsible for triggering the MCI [29].

To form a monolayer, the equally charged particles have to be confined vertically as well as horizontally. In the experiment, the confinement can be controlled, *e.g.*, by varying the discharge power or gas pressure [29]. In simulations it is treated as a tunable parameter, allowing us to control the crystal stability and anisotropy effects. The anisotropic parabolic confinement force in the horizontal plane is characterized by the confinement parameter $\Omega_\parallel = 2\pi f_\parallel$ acting in the direction of the angle α (measured from the x-axis), and $\Omega_\perp = 2\pi f_\perp$ that is perpendicular to it. Thus,

$$\boldsymbol{C}_i = -\begin{pmatrix}\Omega_s^2 x_i + \Omega_a^2(x_i\cos 2\alpha + y_i \sin 2\alpha) \\ \Omega_s^2 y_i + \Omega_a^2(x_i \sin 2\alpha - y_i \cos 2\alpha) \\ \Omega_z^2 z_i\end{pmatrix}, \tag{3}$$

where Ω_s and Ω_a are the symmetric and asymmetric contributions to the horizontal confinement, and

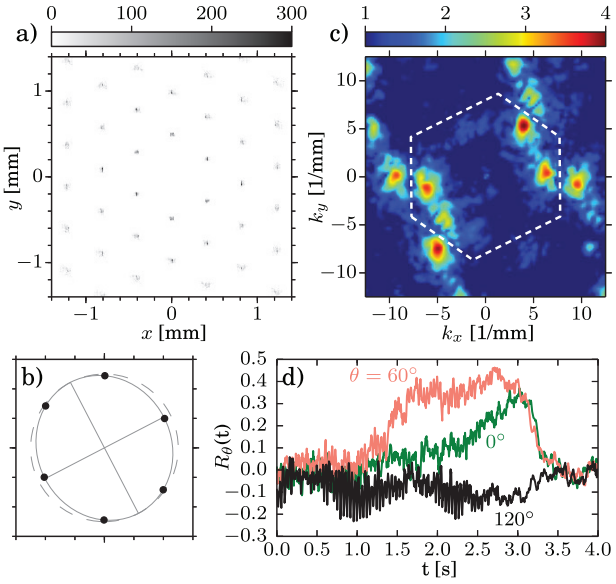

Fig. 2: (Color online) Synchronized particle motion at the onset of mode-coupling–induced melting of 2D plasma crystal. (a) Pair correlation $g(\boldsymbol{r})$ in the horizontal plane at $t = 0$. (b) $g(\boldsymbol{r})$ in a smaller window of side length 1.2 mm with the first peaks shown as solid circles. An ellipse (solid line) is fitted to the positions of the peaks, its semiaxes of length $A = (0.500 \pm 0.014)$ mm and $B = (0.454 \pm 0.011)$ mm are also shown as solid lines. The tilt angle of the ellipse is $\beta = (27 \pm 2)°$. The dashed circle with a radius identical to A is shown to guide the eye. (c) Integrated particle current fluctuation spectrum of the longitudinal mode in the k_xk_y-plane, with arbitrary units in a logarithmic scale, calculated from the first 3.2 s of the data. The border of the first Brillouin zone is shown as a dashed line. (d) Order parameter $R_\theta(t)$ measuring the degree of synchronization of the particles as a function of time t, see eq. (6).

Ω_z the vertical-confinement parameter. The symmetric and asymmetric contributions can be expressed as $\Omega^2_{s,a} = (\Omega^2_\parallel \pm \Omega^2_\perp)/2$. The orientation of the confinement anisotropy can thus be changed without changing the choice of the axes depicted in the inset of fig. 1, leading to a horizontal compression of the crystal in the direction denoted by the angle α.

The particles are also coupled to a Langevin heat bath of temperature $T = 300$ K,

$$\langle \boldsymbol{L}_i(t)\rangle = 0, \quad \langle \boldsymbol{L}_i(t+\tau)\boldsymbol{L}_j(t)\rangle = 2\nu m T\delta_{ij}\delta(\tau). \qquad (4)$$

δ_{ij} is the Kronecker delta and $\delta(\tau)$ is the delta function.

In a simulation run, a system of 16384 particles, each with a mass $m = 6.1 \times 10^{-13}$ kg and charge $Q = -19000e$, is first equilibrated at $f_\parallel = f_\perp = 0.145$ Hz and a large vertical confinement $f_z = \Omega_z/2\pi = 23$ Hz that prevents the onset of MCI. When a crystal is formed in the center of the monolayer, the horizontal frequencies are changed to $f_\parallel = 0.156$ Hz and $f_\perp = 0.137$ Hz to introduce an anisotropy. After equilibration, the vertical confinement is finally reduced to $f_z = 20$ Hz to trigger the instability, this moment corresponds to $t = 0$. Because of the sixfold symmetry of the crystal, it is sufficient to study the orientation of the confinement anisotropy in the range $0° \le \alpha \le 30°$. Here, two simulations with $\alpha = 30°$ and $\alpha = 0°$ are considered. The damping rate is assumed to be $\nu = 1.26\,\mathrm{s}^{-1}$, the screening length is $\lambda = 380\,\mu$m. A point-like wake charge $q = 0.2|Q|$ is a distance $\delta = 0.3\lambda$ below each particle.

Analysis methods. – The radial pair correlation function in the horizontal plane, $g(\boldsymbol{r})$, is used to measure the inhomogeneity in the hexagonal lattice. An ellipse is fitted to the first six peaks of $g(\boldsymbol{r})$. The tilt angle β and the eccentricity ϵ are used to quantify the deformation of the crystal.

The particle current [35] for the longitudinal in-plane mode is defined as

$$V(\boldsymbol{k}, t) = \sum_j v_j^{\boldsymbol{k}}(t) e^{-i\boldsymbol{k}\cdot\boldsymbol{r}_j}, \qquad (5)$$

where $v_j^{\boldsymbol{k}}(t)$ is the component of the velocity of particle j at time t parallel to wave vector $\boldsymbol{k} = (k_x, k_y)$. The particle current fluctuation spectra of the longitudinal mode $V(\boldsymbol{k}, f)$ are then calculated using the Fourier transform. To show the spectra in the xy-plane, $V(\boldsymbol{k}, f)$ is integrated over a frequency range $14\,\mathrm{Hz} < f < 18\,\mathrm{Hz}$ centered on the hybrid frequency $f_{\mathrm{hyb}} = (16 \pm 1)$ Hz. The MCI, where the out-of-plane mode couples to the longitudinal in-plane mode, appears as hot spots in the spectra of both modes [29]. The out-of-plane mode is not considered since it is not available for the experimental data. In the simulations, the integrated spectrum of the out-of-plane mode is very similar to that of the longitudinal mode. The border of the first Brillouin zone is calculated from the static structure factor $S(\boldsymbol{k}) = N^{-1}\langle\sum_{l,m} e^{i\boldsymbol{k}\cdot(\boldsymbol{r}_l - \boldsymbol{r}_m)}\rangle$, where N is the number of particles, the sum runs over all pairs of particles, and the averaging is performed over time.

The chains of synchronized particle motion (see fig. 1) cannot be characterized using the Kuramoto order parameter $re^{i\psi} = (1/N)\sum_j e^{i\phi_j}$ [20], because neighboring chains tend to be in antiphase. The contributions to the order parameter would thus cancel even in the presence of a synchronization pattern. Therefore, we define a local order parameter as

$$R_{i,\theta}(t) = \frac{1}{\mathrm{nn}}\left(\sum_{j=1}^{\mathrm{nn}}\left[(-1)^{k_j}\cos(\phi_{j,\theta} - \phi_{i,\theta})\right]\right), \qquad (6)$$

where $\phi_{i,\theta}$ is the phase of the oscillation of particle i in the direction denoted by angle θ at time t and nn is the number of nearest neighbors. $k_j = 0$ if particle j is on the line passing through particle i perpendicular to direction denoted by θ, and $k_j = 1$ otherwise[1]. In the inset of fig. 1,

[1]Since the crystal is highly ordered, the definition of particle lines is straightforward. We consider two neighboring particles i and j to be on a line if the angle between the i-j bond and the line is smaller than 30°.

the direction denoted by $\theta = 60°$ is indicated by an arrow and the line perpendicular to it by a dashed line. The cosine of the phase differences are thus added for nearest neighbors on the same line and subtracted for nearest neighbors on the subsequent lines, leading to $R_{i,\theta} = 1$ if particle i is in a region with perfect alternating in-phase and out-of-phase oscillating lines of particles. In the opposite case, $R_{i,\theta} = -1$. If there is no phase relation, $R_{i,\theta} \simeq 0$.

The instantaneous phase $\phi_{i,\theta}$ is calculated from the projection of position $\boldsymbol{r}_i$ in the horizontal plane onto the direction denoted by θ. The instantaneous deviation from the time-averaged particle position is obtained with a sliding window of length 0.2 s. The phase is then assumed to grow linearly by 2π between each maximum of the deviation. An order parameter for the system is calculated by averaging over all particles $R_\theta(t) = \langle R_{i,\theta}(t)\rangle_i$. The three main directions of the crystal, $\theta = 0°$, $60°$ and $120°$, are considered.

In ref. [36] a local order parameter was used to increase the resolution for a system where the number of oscillators is small. The local order parameter proposed here is sensitive to the orientation of the synchronization pattern. In fig. 1, maps of $\phi_{i,\theta}$ and $R_{i,\theta}$ are shown for the experimental data at a characteristic time $t = 2.5$ s for $\theta = 0°$ and $\theta = 60°$. Lines with two different orientations are apparent for $\phi_{i,\theta=0°}$, see fig. 1(a). The corresponding order parameter $R_{i,\theta=0°}$ (see fig. 1(b)) is sensitive to the lines that are oriented along the y-axis which are located in the lower part of the inspection window. For $\theta = 60°$ (figs. 1(c) and (d)), the largest values of the order parameter are concentrated in the upper part of the window.

Results. – The experimental data of ref. [19] is analyzed in a window containing about 800 particles near the center of the crystal. The pair correlation $g(\boldsymbol{r})$ is shown in fig. 2(a). A deviation from a perfect hexagonal structure can clearly be seen. In fig. 2(b), an ellipse is fitted to the first peaks of $g(\boldsymbol{r})$, its tilt angle is $\beta = (27 \pm 2)°$. The value of the eccentricity is $\epsilon = 0.42 \pm 0.07$.

The phases $\phi_{i,\theta}$ are calculated for a smaller window of side length 6.5 mm containing about 230 particles. In this region synchronized particle motion was observed. As can be seen in fig. 2(d), the order parameter R_θ has significant positive values for $\theta = 0°$ and $\theta = 60°$. In the latter case, $R_{\theta=60°}$ increases between $t \simeq 1$ s and $t \simeq 2$ s and then saturates at a value of $R_{\theta=60°} \simeq 0.4$. At $t \simeq 3.2$ s the crystal melts and the order parameter drops back to zero. For $\theta = 0°$, $R_{\theta=0°}$ increases much more slowly in a time interval $1\,\text{s} < t < 3\,\text{s}$ before also decreasing again when the crystal melts. $R_{\theta=120°}$ becomes slightly negative during the phase of synchronized motion in the other directions (see supplementary movie `mci-synchronization.mp4` for the time evolution of the order parameter).

In the first simulation, the crystal was compressed at an angle of $\alpha = 30°$. The region of interest is chosen to be of the same size as in the experiments. The pair correlation $g(\boldsymbol{r})$ is shown in fig. 3(a). An ellipse is fitted to the first peaks of $g(\boldsymbol{r})$ (see fig. 3(b)), the value of the tilt angle, $\beta = (29.7 \pm 0.5)°$, is close to the experiment, the value of the eccentricity $\epsilon = 0.36 \pm 0.03$ is slightly smaller. The integrated spectrum of the longitudinal mode (see fig. 3(c)) shows bright hot spots in two main directions of the crystal. The hot spot at $\theta = 120°$ that would be expected for a perfect hexagonal lattice is almost absent.

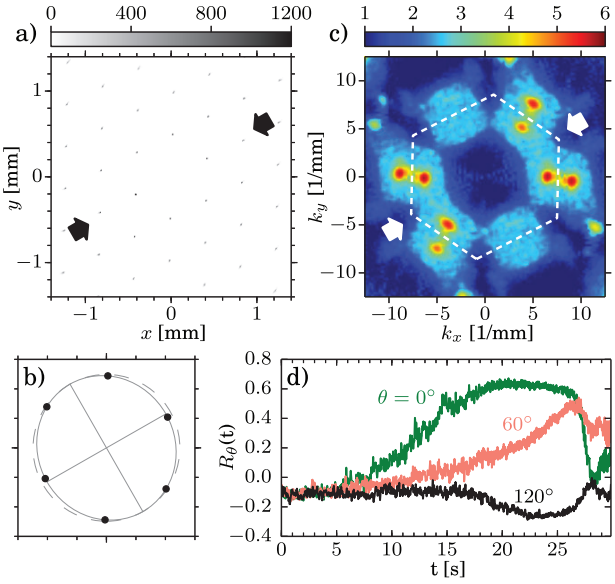

Fig. 3: (Color online) Same as fig. 2, but for a molecular-dynamics simulation of a crystal with an anisotropy in the horizontal parabolic confinement. The direction of the largest confinement frequency $f_\parallel = 0.156$ Hz, given by angle $\alpha = 30°$ (see eq. (3)), is indicated by arrows in (a) and (c), the frequency in the perpendicular direction is $f_\perp = 0.137$ Hz. The vertical-confinement frequency is $f_z = 20$ Hz. In (b), the semiaxes of the ellipse fitted to the first peaks of $g(\boldsymbol{r})$ are of length $A = (0.498 \pm 0.004)$ mm and $B = (0.464 \pm 0.003)$ mm. The tilt angle of the ellipse is $\beta = (29.7 \pm 0.5)°$. In (c), the first 25 s of the data are used to calculate the spectrum.

The main characteristics of the synchronization process in the experiment are recovered in the simulations, albeit with the roles of $\theta = 0°$ and $\theta = 60°$ interchanged: As can be seen in fig. 3(d), the order parameter saturates at $R_{\theta=0°} \simeq 0.6$ rather quickly in one direction, while it follows more slowly in the other. At $t \simeq 27$ s, both order parameters decrease. For $\theta = 120°$, the order parameter decreases to about -0.2 to -0.3. Note that the time scale is larger than in the experiment.

The order parameter is slightly negative even at $t = 0$. This could be explained by noting that before the onset of MCI, the particle movement is slightly correlated between nearest neighbors due to their mutual repulsion. This small positive correlation leads to a negative R_θ, since the phase differences to the four neighbors on the next lines are subtracted from the phase differences to only two neighbors on the same line. The decrease of $R_{\theta=120°}$ during the period of synchronization can be explained by the fact that the three directions of the projection are not orthogonal.

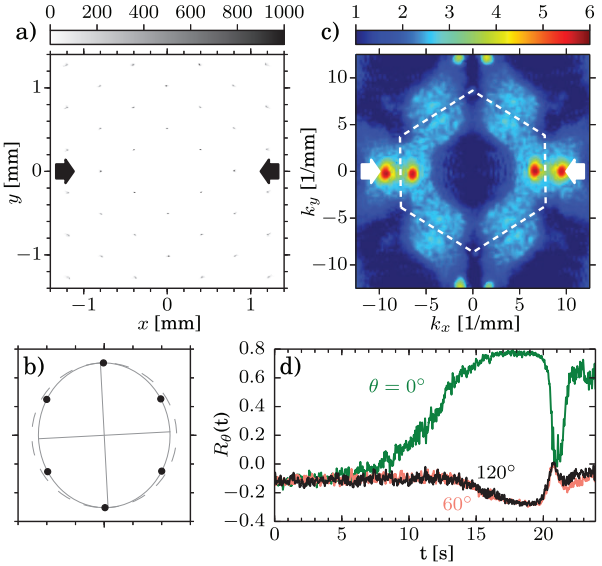

Fig. 4: (Color online) Same as fig. 3, but for a different direction of the anisotropy in the horizontal confinement, $\alpha = 0°$. In (b), the semiaxes of the ellipse fitted to the first peaks of $g(\boldsymbol{r})$ are of length $A = (0.504 \pm 0.004)$ mm and $B = (0.458 \pm 0.004)$ mm. The tilt angle of the ellipse is $\beta = (3.0 \pm 0.5)°$. In (c), the first 20 s of the data are used to calculate the spectrum.

Consequently, alternating lines of in-phase and anti-phase particles in one direction lead to a negative order parameter in the other directions.

In a second simulation, the orientation of the confinement anisotropy was $\alpha = 0°$. The pair correlation $g(\boldsymbol{r})$ and the ellipse fitted to the first six peaks of $g(\boldsymbol{r})$ are shown in fig. 4(a) and (b). As expected, the ellipse is tilted by only a small angle of $(3.0 \pm 0.5)°$. The eccentricity $\epsilon = 0.42 \pm 0.03$ is larger than in the first simulation. The integrated particle fluctuation spectrum (fig. 4(c)) shows that the MCI is dominant only in the x direction.

Here, synchronized motion is only observed in $\theta = 0°$ direction, see fig. 4(d). The corresponding order parameter increases between $t \simeq 5$ s and $t \simeq 15$ s and subsequently saturates at $R_{\theta=0°} \simeq 0.8$. R_θ decreases to negative values (about -0.2 to -0.3) in the other two directions $\theta = 60°$ and $\theta = 120°$.

At $t \simeq 20$ s, $R_{\theta=0°}$ decreases and increases again at $t \simeq 21.5$ s. This can be understood as follows. As observed in [33], a molecular-dynamics simulation of MCI does not lead to a complete melting of the crystal but rather to cycles of partial melting and recrystallization. Thus, the synchronization process does not completely stop as in the case of the experiment.

Discussion and conclusion. – The good agreement of the simulation (fig. 3) with the experiment (fig. 2) suggests that the confinement asymmetry can be used to explain the observed anisotropic triggering of MCI and the synchronization process. The anisotropy of the spectral intensity of the particle velocity fluctuations indicates undoubtedly that the MCI is sensitive to a weak anisotropy in the horizontal confinement. The dispersion relations for a sheared crystal were examined theoretically in refs. [37,38].

In the experiment, the hot spot at $\theta = 60°$ is much brighter than the one in the opposite direction $\theta = 240°$ which almost vanishes, see fig. 2(c). This effect —which is much weaker in the simulations— may be due to further anisotropies in the crystal structure, stemming for example from defect chains near the boundary of the plasma crystal. It will be subject to further studies.

Confining a plasma crystal in the horizontal plane always makes it internally inhomogeneous. A parabolic confinement is often used in the literature, see, *e.g.*, [16,17,31,32]. The scaling laws of plasma crystals are also well known. In particular, the interaction range $\kappa = a/\lambda$ of such clusters is weakly dependent on the strength of the horizontal-confinement parameter Ω_c,

$$\kappa \propto \Omega_c^{-1/2}, \tag{7}$$

as is easy to verify by using refs. [15,31,39]. Taking into account that the critical vertical confinement for MCI to be triggered, $\Omega_{z,\mathrm{crit}}$, is known to be strongly dependent on the particle interaction range κ (see ref. [29] for details), the influence of the horizontal-confinement strength becomes apparent. For plasma clusters, the dependence of $\Omega_{z,\mathrm{crit}}$ on κ is described by [29]

$$\frac{\Omega_{z,\mathrm{crit}}^2}{\Upsilon(\kappa)} \simeq \mathrm{const}, \quad \Upsilon(\kappa) = \frac{\kappa^2 + 3\kappa + 3}{\kappa^3} e^{-\kappa}. \tag{8}$$

The dependence of $\Omega_{z,\mathrm{crit}}$ on Ω_c can be calculated by combining eqs. (7) and (8):

$$\frac{\delta\Omega_{z,\mathrm{crit}}}{\Omega_{z,\mathrm{crit}}} = \Lambda(\kappa)\frac{\delta\Omega_c}{\Omega_c}, \quad \Lambda(\kappa) = \frac{1}{4}\left(\kappa + \frac{(\kappa+3)^2}{\kappa^2+3\kappa+3}\right). \tag{9}$$

Since $\Lambda(\kappa) \sim 1$ at $\kappa \sim 1$, the relative variation of the instability threshold is practically proportional to the relative variation of the horizontal-confinement strength.

The prediction of eccentricity ϵ due to an anisotropic horizontal confinement can be deduced from eq. (7), yielding $\epsilon^{\mathrm{theory}} = \left[1 - (\kappa(\Omega_\parallel)/\kappa(\Omega_\perp))^2\right]^{1/2} \simeq 0.35$. Of course, in a more detailed analysis the orientation of the anisotropy would have to be taken into account, as the compressibility of the crystal depends on it. Still, this estimate is not far from the values of experiment and simulations.

The role of frequency synchronization [19] was not studied here since special care was taken to quantify the orientations of the phase synchronization processes. The interplay of phase and frequency synchronization during the onset of MCI is an important point in the understanding of the collective phenomenon.

An order parameter motivated by the Kuramoto model is often used to quantify synchronization processes [36]. If the interaction is repulsive, complex patterns can arise

that call for a detailed analysis. For example, traveling waves [40] or competing domains of different chirality [41] were observed. Here, a local order parameter was proposed which is sensitive to the orientation of the observed synchronization patterns.

To conclude, it was shown in simulations that an anisotropy of the horizontal confinement can cause an asymmetric triggering of MCI which is accompanied by particle chains with synchronized motion. To the best of our knowledge, it is reported for the first time that a horizontal compression in simulations of a plasma crystal reproduces well the synchronization process observed in experiments. For an appropriate orientation of the anisotropy, MCI is triggered in two directions which leads to competing synchronization patterns. If MCI is triggered in one direction, a single pattern dominates. A new order parameter was proposed that is able to quantify direction-dependent synchronization. We were thus able to identify synchronization patterns that show a pronounced anisotropy.

* * *

This project received funds from the German Federal Ministry for Economy and Technology under grant No. 50WM1441. SZh received support from the European Research Council under the European Union's Seventh Framework Programme (FP7/2007-2013)/ERC Grant agreement 267499. LC, VN and SZh received support from the French-German PHC PROCOPE program (No. 28444XH/55926142).

REFERENCES

[1] Ikezi H., *Phys. Fluids*, **29** (1986) 1764.
[2] Thomas H., Morfill G. E., Demmel V., Goree J., Feuerbacher B. and Möhlmann D., *Phys. Rev. Lett.*, **73** (1994) 652.
[3] Hayashi Y. and Tachibana K., *Jpn. J. Appl. Phys.*, **33** (1994) L804.
[4] Chu J. H. and Lin I, *Phys. Rev. Lett.*, **72** (1994) 4009.
[5] Thomas H. M. and Morfill G. E., *Nature*, **379** (1996) 806.
[6] Morfill G. E. and Ivlev A. V., *Rev. Mod. Phys.*, **81** (2009) 1353.
[7] Samsonov D., Ivlev A. V., Morfill G. E. and Goree J., *Phys. Rev. E*, **63** (2001) 025401(R).
[8] Nunomura S., Samsonov D. and Goree J., *Phys. Rev. Lett.*, **84** (2000) 5141.
[9] Fortov V. E., Khrapak A. G., Khrapak S. A., Molotkov V. I., Nefedov A. P., Petrov O. F. and Torchinsky V. M., *Phys. Plasmas*, **7** (2000) 1374.
[10] Misawa T., Ohno N., Asano K., Sawai M., Takamura S. and Kaw P., *Phys. Rev. Lett.*, **86** (2001) 1219.
[11] Samsonov D., Ivlev A. V., Quinn R. A., Morfill G. and Zhdanov S., *Phys. Rev. Lett.*, **88** (2002) 095004.
[12] Williams J. D., *Phys. Rev. E*, **90** (2014) 043103.
[13] Nosenko V., Zhdanov S. and Morfill G., *Phys. Rev. Lett.*, **99** (2007) 025002.
[14] Nosenko V., Zhdanov S. and Morfill G., *Philos. Mag.*, **88** (2008) 3747.
[15] Zhdanov S. K., Thoma M. H. and Morfill G. E., *New J. Phys.*, **13** (2011) 013039.
[16] Durniak C. and Samsonov D., *Phys. Rev. Lett.*, **106** (2011) 175001.
[17] Durniak C., Samsonov D., Ralph J. F., Zhdanov S. and Morfill G., *Phys. Rev. E*, **88** (2013) 053101.
[18] Zwicky F., *Phys. Rev.*, **43** (1933) 270.
[19] Couëdel L., Zhdanov S., Nosenko V., Ivlev A. V., Thomas H. M. and Morfill G. E., *Phys. Rev. E*, **89** (2014) 053108.
[20] Kuramoto Y., *Chemical Oscillations, Waves, and Turbulence* (Springer, New York) 1984.
[21] Walker T. J., *Science*, **166** (1969) 891.
[22] Wiesenfeld K., Colet P. and Strogatz S. H., *Phys. Rev. Lett.*, **76** (1996) 404.
[23] Kuramoto Y., *Prog. Theor. Phys. Suppl.*, **79** (1984) 223.
[24] Schella A., Mulsow M., Melzer A., Schablinski J. and Block D., *Phys. Rev. E*, **87** (2013) 063102.
[25] Laut I., Räth C., Wörner L., Nosenko V., Zhdanov S. K., Schablinski J., Block D., Thomas H. M. and Morfill G. E., *Phys. Rev. E*, **89** (2014) 023104.
[26] Melzer A., Schweigert V. and Piel A., *Phys. Rev. Lett.*, **83** (1999) 3194.
[27] Ivlev A. V. and Morfill G., *Phys. Rev. E*, **63** (2000) 016409.
[28] Zhdanov S. K., Ivlev A. V. and Morfill G., *Phys. Plasmas*, **16** (2009) 083706.
[29] Couëdel L., Zhdanov S. K., Ivlev A. V., Nosenko V., Thomas H. M. and Morfill G. E., *Phys. Plasmas*, **18** (2011) 083707.
[30] Schablinski J., Block D., Carstensen J., Greiner F. and Piel A., *Phys. Plasmas*, **21** (2014) 073701.
[31] Totsuji H., Totsuji C. and Tsuruta K., *Phys. Rev. E*, **64** (2001) 066402.
[32] Ivlev A. V., Konopka U., Morfill G. E. and Joyce G., *Phys. Rev. E*, **68** (2003) 026405.
[33] Röcker T. B., Couëdel L., Zhdanov S. K., Nosenko V., Ivlev A. V., Thomas H. M. and Morfill G. E., *EPL*, **106** (2014) 45001.
[34] Ott T., Bonitz M., Stanton L. G. and Murillo M. S., *Phys. Plasmas*, **21** (2014) 113704.
[35] Donkó Z., Kalman G. J. and Hartmann P., *J. Phys.: Condens. Matter*, **20** (2008) 413101.
[36] Fukuda H., Morimura H. and Kai S., *Physica D*, **205** (2005) 80.
[37] Ivlev A. V., Röcker T. B., Couëdel L., Nosenko V. and Du C.-R., *Phys. Rev. E*, **91** (2015) 063108.
[38] Zhdanov S. K., *Anisotropic confinement effects in a two-dimensional plasma crystal*, in preparation (2015).
[39] Peeters F. M. and Wu X., *Phys. Rev. A*, **35** (1987) 3109.
[40] Hong H. and Strogatz S. H., *Phys. Rev. Lett.*, **106** (2011) 054102.
[41] Giver M., Jabeen Z. and Chakraborty B., *Phys. Rev. E*, **83** (2011) 046206.

Anisotropic confinement effects in a two-dimensional plasma crystal (Ref. [113])

I. Laut, S. K. Zhdanov, C. Räth, H. M. Thomas and G. E. Morfill. *Anisotropic confinement effects in a two-dimensional plasma crystal*, Physical Review E **93**, 013204 (2016) http://dx.doi.org/10.1103/PhysRevE.93.013204
©2016 American Physical Society

PHYSICAL REVIEW E **93**, 013204 (2016)

Anisotropic confinement effects in a two-dimensional plasma crystal

I. Laut,[1,*] S. K. Zhdanov,[2] C. Räth,[1] H. M. Thomas,[1] and G. E. Morfill[2,3]
[1]*Deutsches Zentrum für Luft- und Raumfahrt, Forschungsgruppe Komplexe Plasmen, 82234 Weßling, Germany*
[2]*Max Planck Institute for extraterrestrial Physics, 85741 Garching, Germany*
[3]*BMSTU Centre for Plasma Science and Technology, Moscow, Russia*
(Received 3 November 2015; published 8 January 2016)

The spectral asymmetry of the wave-energy distribution of dust particles during mode-coupling-induced melting, observed for the first time in plasma crystals by Couëdel *et al.* [Phys. Rev. E **89**, 053108 (2014)], is studied theoretically and by molecular-dynamics simulations. It is shown that an anisotropy of the well confining the microparticles selects the directions of preferred particle motion. The observed differences in intensity of waves of opposed directions are explained by a nonvanishing phonon flux. Anisotropic phonon scattering by defects and Umklapp scattering are proposed as possible reasons for the mean phonon flux.

DOI: 10.1103/PhysRevE.93.013204

I. INTRODUCTION

Complex or dusty plasmas are weakly ionized gases containing micron-sized particles. In a laboratory radio-frequency (rf) plasma, these particles are negatively charged and thus repel each other. In rf discharge complex plasmas, the particles are self-trapped in the plasma [1–3]. Due to their strong interactions with the plasma and with each other, they can form strongly coupled crystals [4,5], called *plasma crystals*. Complex plasmas are ideal model systems for phase transitions [6,7], transport processes [8–11], and self-organization [12,13]. In ground-based experiments, the particles levitate in the plasma sheath region above the lower electrode where they can form a horizontal two-dimensional (2D) monolayer under adequate experimental conditions [1–3]. Due to the finite vertical confinement of the crystal, the monolayer is not completely flat, allowing an out-of-plane wave mode that has an optical dispersion relation in addition to the two in-plane modes with acoustic dispersion.

The surrounding plasma strongly influences the particle-particle interaction, making it anisotropic. While the mutual repulsion of equally charged particles is ascribed to a Yukawa potential [14], an attractive component stems from the plasma wake [15], which is formed beneath every particle downstream of the ion flow. In theory and simulations, the plasma wake is often modeled as a pointlike effective charge below each particle [16]. If the vertical particle confinement is small enough, a *mode-coupling instability* (MCI) can occur in such a model, coupling the out-of-plane mode to the longitudinal mode [16,17]. Near the intersection of the modes, the unstable hybrid mode grows until the crystalline order breaks. The experimental observations are in very good agreement with the predictions of the model [18,19].

In an ideal hexagonal lattice, the MCI is equally strong in all three main directions of the crystal, reflecting its sixfold symmetry [19]. In Ref. [20], however, the instability was well pronounced dominantly in only one direction. A synchronization pattern of alternating in-phase and anti-phase oscillations accompanied the asymmetric triggering of MCI. Similar symmetry-breaking patterns were observed in colloids on global [21] and intermediate [22] scales. A lattice deformation was suggested in Ref. [20] as a possible explanation for the symmetry breaking, though it was experimentally difficult to study. It was shown in simulations that the asymmetry of MCI can be caused by an anisotropy of the horizontal confinement [23]. Under adequate conditions, the instability can be active only in the direction of the compression of the crystal. The main conclusion was that for an appropriate orientation of the anisotropy, MCI could be triggered in two directions, which leads to competing synchronization patterns. If MCI is triggered in one direction, a single pattern dominates. It was not possible, however, to explain a left-right asymmetry of opposed directions, which was also present in the spectra [23].

In theoretical treatments the presence of the *finite* horizontal confinement of the crystal is often ignored. For doing so there are certain arguments in addition to facilitating the theoretical description: (i) The horizontal confinement is known to be 100–200 times weaker than the vertical confinement [24], allowing systems that are very extended in the horizontal direction. (ii) "Confinement-free" systems (so-called Yukawa systems) of mutually repelling particles are an excellent substitute to explain many, sometimes very delicate effects observed in experiments. (iii) The results obtained seem to be universal and important for many applications.

Still, the simplification of an infinite plasma crystal is not always justified. In the problem considered here the finite confinement is explicitly taken into account. The competition of the sixfold symmetry of the crystal lattice and the radial symmetry of the horizontal confinement leads to defects and inhomogeneities in the crystal. The actual configuration of the confining fields affects the structure of the microparticle cloud.

In this paper we would like to highlight and report on the physics of *spontaneous breaking of spectral symmetry* of the wave energy distribution of an anisotropically confined plasma crystal during the early stage of MCI. This asymmetry plays an eminent role in the understanding of the synchronization processes observed in experiments [20] and simulations [23] and may give hints to the connection to the recently discovered *chimera states* that further fueled the interest in oscillator networks with controllable eigenfrequencies, coupling and topology [25–28].

*Ingo.Laut@dlr.de

 ©2016 American Physical Society

The paper is organized as follows. In Sec. II, the numerical algorithm and the simulation procedure are described. In Sec. III, the spectral asymmetry of a simulated complex plasma crystal is analyzed and compared to a theoretical model. In Sec. IV, the origin of this symmetry breaking is investigated in detail. The anisotropic phonon scattering by defects and the anisotropic Umklapp scattering are identified as two possible mechanisms introducing the asymmetry. Finally, in Sec. V, we conclude with a summary and discussion of our results.

II. SIMULATION PARTICULARS

A. Governing equations

Molecular-dynamics simulations have proven to be an adequate tool to study and compare a wide range of experimental conditions. In the simulations, the potential well that confines the particles is treated as a tunable parameter, allowing control over the lattice configuration [29,30], crystal stability [31,32], and anisotropy effects [23]. A parabolic confinement well is often used to simulate a monolayer suspension [29,30,33–35]. To model a monolayer extended in the xy plane, a highly anisotropic three-dimensional confinement well, about 100 times stronger vertically than horizontally, is used [23,31,32]. In addition, the horizontal confinement can easily be made anisotropic as is explained below.

The equations of motion employed in simulations read [19,23]

$$M\ddot{\mathbf{r}}_i + M\nu\dot{\mathbf{r}}_i = \sum_{j\neq i}\mathbf{F}_{ji} + \mathbf{C}_i + \mathbf{L}_i, \tag{1}$$

where $\mathbf{r}_i$ is the position of the ith particle ($i = 1 \ldots N$, N the total number of particles), M the particle mass, and ν the damping rate. The particle dynamics are governed by the mutual particle-particle interactions ($\mathbf{F}_{ji}$), the external interactions which are enabling confinement of the particle cloud ($\mathbf{C}_i$), and a heat bath ($\mathbf{L}_i$).

To characterize the particle confinement, it is instructive to introduce the (isotropic) horizontal confinement parameter Ω_c as well as the strength p and the direction α of the loading asymmetry. The strength of the vertical confinement is characterized by Ω_z. The external confinement $\mathbf{C}_i = \{C_{i,x}, C_{i,y}, C_{i,z}\}$ then reads (cf. [23])

$$\begin{aligned} C_{i,x} &= -M\Omega_c^2 X_i, \quad C_{i,y} = -M\Omega_c^2 Y_i, \quad C_{i,z} = -M\Omega_z^2 z_i, \\ X_i &= x_i + p(x_i\cos 2\alpha + y_i \sin 2\alpha), \\ Y_i &= x_i + p(x_i \sin 2\alpha - y_i \cos 2\alpha). \end{aligned} \tag{2}$$

Horizontally, the simulated crystal can thus be dominantly compressed under any angle α measured from the x axis (see Fig. 1). For instance, at $\alpha = 0$ the horizontal confinement forces are distributed so that $C_{i,x} = -m\Omega_c^2 x_i(1+p)$, $C_{i,y} = -m\Omega_c^2 y_i(1-p)$, and therefore the confinement is $(1+p)/(1-p)$ times "stronger" in x direction than in y direction. It is also useful to define the confinement frequencies parallel $2\pi f_\parallel = \Omega_c\sqrt{1+p}$ and perpendicular $2\pi f_\perp = \Omega_c\sqrt{1-p}$ to the direction of the compression denoted by angle α.

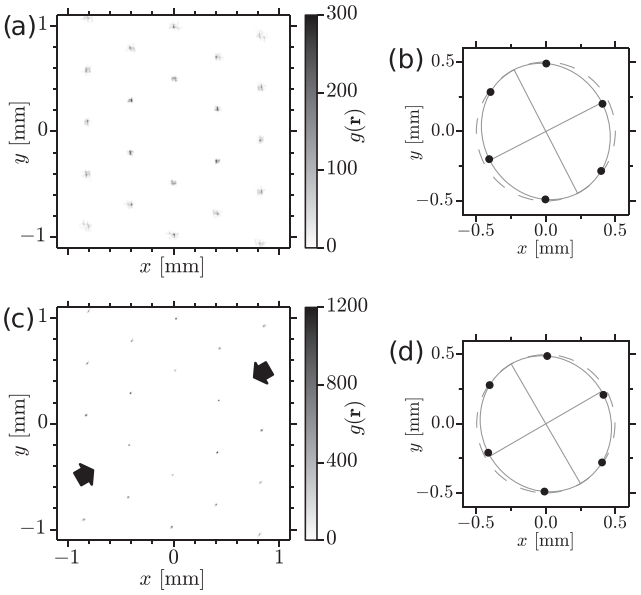

FIG. 1. Pair correlation function $g(\mathbf{r})$ for horizontally compressed crystals. (a) $g(\mathbf{r})$ in the horizontal plane of the experimental data of Ref. [20]. A central square of side length 13 mm was considered at time $t = 0$. (b) The first peaks of $g(\mathbf{r})$ are shown as solid circles. An ellipse (solid line) is fitted to the positions of the peaks; its deviation from a circle (dashed line) can be clearly seen. (c), (d) The same for the simulated data of run I (see Table I). Here, $t = 0$ corresponds to the starting point of the dynamical phase. In panel (c), the direction of the angle of compression α is indicated by black arrows.

Following Refs. [20,23], the force exerted by particle j (and its wake) on particle i is introduced as

$$\begin{aligned} \mathbf{F}_{ji} = {} & \frac{Q^2}{r_{ji}^2}\exp\left(-\frac{r_{ji}}{\lambda}\right)\left(1+\frac{r_{ji}}{\lambda}\right)\frac{\mathbf{r}_{ji}}{r_{ji}} \\ & - \frac{q|Q|}{r_{w_{ji}}^2}\exp\left(-\frac{r_{w_{ji}}}{\lambda}\right)\left(1+\frac{r_{w_{ji}}}{\lambda}\right)\frac{\mathbf{r}_{w_{ji}}}{r_{w_{ji}}}, \end{aligned} \tag{3}$$

where $Q < 0$ is the particle charge, λ is the screening length, $\mathbf{r}_{ji} = \mathbf{r}_i - \mathbf{r}_j$ and $\mathbf{r}_{w_{ji}} = \mathbf{r}_i - (\mathbf{r}_j - \delta\mathbf{e}_z)$, where $\mathbf{e}_z$ is the ("vertical") unit vector perpendicular to the monolayer plane. The pointlike wake charge q ($0 < q < |Q|$) is located at a distance δ ($\delta < \lambda$) below each particle. The particle charges, the screening length, and the wake parameters are considered as fixed in every simulation run (see Table I).

The particles are also coupled to a Langevin heat bath of temperature $T = 300$ K,

$$\langle \mathbf{L}_i(t)\rangle = 0, \quad \langle \mathbf{L}_i(t+\tau)\mathbf{L}_j(t)\rangle = 2\nu m T\delta_{ij}\delta(\tau). \tag{4}$$

δ_{ij} is the Kronecker δ and $\delta(\tau)$ is the δ function. It is a commonly used approximation that allows one to simulate the random excitations stemming from the gas surrounding the particles [34,35] (or plasma, as necessary [30]).

B. Simulation procedure

The equations of motion [Eq. (1)] were integrated using the Beeman algorithm with predictor-corrector modifications [36,37]. The code is parallelized using OpenMP. The vertical

TABLE I. Parameters of the simulation runs.

Parameter	Run I	Run II
N	16384	10000
M (pg)	610	610
Q (e)	−19000	−19000
ν (s^{-1})	1.26	1.26
λ (μm)	380	380
$q/\lvert Q\rvert$	0.2	0.2
δ/λ	0.3	0.3
α (°)	30	0
	Equilibration phase	
f_z (Hz)	23.0	22.0
$f_\parallel$ (Hz)	0.145	0.19
$f_\perp$ (Hz)	0.145	0.19
	Deformation phase	
f_z (Hz)	23.0	22.0
$f_\parallel$ (Hz)	0.156	0.20
$f_\perp$ (Hz)	0.137	0.18
	Dynamical phase	
f_z (Hz)	20.0	19.5
$f_\parallel$ (Hz)	0.156	0.20
$f_\perp$ (Hz)	0.137	0.18

confinement frequency was about two orders of magnitude larger than the horizontal confinement frequencies, leading to the formation of quasi-2D monolayers.

Every simulation run was divided into three main phases characterized by three confinement frequencies each; see Table I. The particles were initially positioned on a hexagonal grid. During the equilibration phase, which is characterized by an anisotropic horizontal confinement and a large vertical confinement that prevents the onset of MCI, the crystal was allowed to relax. The competition of the hexagonal symmetry and the radial confinement lead to the melting of the outer region of the crystal, which then recrystallized to different domains divided by strings of defects. The central region kept the crystal structure. After equilibration, during the deformation phase, the horizontal confinement well was modified to a desirable anisotropic configuration while the strong vertical confinement was kept untouched, and the particle cloud was allowed to relax further. Finally, after reaching the stable deformed configuration, the vertical confinement was reduced in the dynamical phase to trigger the MCI. The temperature of the heat bath and all other parameters were fixed in the simulation runs.

III. RESULTS

A. Pair correlations under loading asymmetry

In simulation run I (see Table I), a monolayer of 16 384 particles, each with a mass of $M = 6.1 \times 10^{-13}$ kg, was formed during the equilibration phase at $f_\parallel = f_\perp = 0.145$ Hz and $f_z = 23$ Hz. The horizontal frequencies were then changed to $f_\parallel = 0.156$ Hz parallel to direction $\alpha = 30°$ and $f_\perp = 0.137$ Hz perpendicular to it in order to introduce an anisotropy corresponding to the loading asymmetry of about $p = 14\%$. Finally, in the dynamical phase, the vertical confinement was reduced to $f_z = 20$ Hz in order to start the instability; see Ref. [23] for details.

The particle positions are analyzed in a window containing about 800 particles near the center of the crystal that showed synchronized motion. Both in experiments and in simulations the first peaks of the radial pair correlation function $g(r)$ are split in two compared to the expected peaks for an ideal hexagonal lattice [20,23]. Indeed, from the 2D pair correlation function $g(\mathbf{r})$ (see Fig. 1) it can be seen that the distance to the nearest neighbors is about 7% smaller under an angle of 30° than in the other two directions. The good agreement of experiment and simulation demonstrates that the asymmetry of $g(\mathbf{r})$ can be attributed to an anisotropic compression of the crystal in the horizontal plane.

B. Asymmetric energy distribution

The distribution of the fluctuation energy of the simulated crystal (as well as in the experiments of Ref. [20]) is dominated by the hot dots (HDs), moreover it is highly asymmetric. To visualize the intensity of the particle current fluctuations $I_{\mathbf{k},\omega}$, it is instructive to average over a frequency range around the hybrid frequency of the coupled longitudinal and transversal modes $f_{\mathrm{hyb}} = (16 \pm 1)$ Hz. The 2D map of the averaged intensity $\bar{I}_{\mathbf{k}}$ in the $k_x k_y$ plane is shown in Fig. 2, top panel. As can be seen in this map, HDs are apparent in only two of the three main directions of the hexagonal lattice. The current fluctuation spectra $I_{\mathbf{k},\omega}$ are calculated from the Fourier transform of the particle currents [20,38]. The border of the first Brillouin zone (fBz) is calculated from the static structure factor $S(\mathbf{k}) = N^{-1}\langle\sum_{l,m} e^{i\mathbf{k}\cdot(\mathbf{r}_l - \mathbf{r}_m)}\rangle$, where the sum runs over all pairs of particles, and the averaging is performed over time. The HDs appear as regions of high intensity inside the fBz.

Note that the HDs at $\theta \simeq 0°$ and $\theta \simeq 180°$ are slightly brighter than the HDs at $\theta \simeq 54°$ and $\theta \simeq 234°$; see Fig. 2, top panel. To further study the anisotropy of the fluctuation spectra, in the middle panels of Fig. 2 the intensity $I_{\mathbf{k},\omega}$ is shown as a function of the modulus of the wave vector k and of frequency f in those directions. By averaging the one-dimensional spectra over the frequency range of interest (indicated as horizontal lines in Fig. 2) one can compare the intensities of the peaks; see Fig. 2, bottom panels. It becomes apparent that the HD intensities in the direction of the x axis ($\theta = 0°, 180°$) are more than a factor of two stronger than the intensities of the HDs in the other direction ($\theta = 54°, 234°$).

Also note that while the HDs on the x axis are nearly equally bright, the HDs at $\theta = 54°$ and $\theta = 234°$ are highly asymmetric; see Fig. 2, bottom panels. Strictly speaking, the HD energy distribution is neither mirror nor rotationally symmetric, indicating strong symmetry breaking. All these results are in a very good qualitative agreement with experimental observations [20,23]. The character of asymmetry indicates the presence of the dominant phonon flux in the ≈234° direction; see Sec. III D.

C. Interaction range of the confined crystal

The anisotropy of the spectral intensity of the particle velocity fluctuations caused by the weakly angle-dependent loading indicates that the MCI is sensitive to a variation of

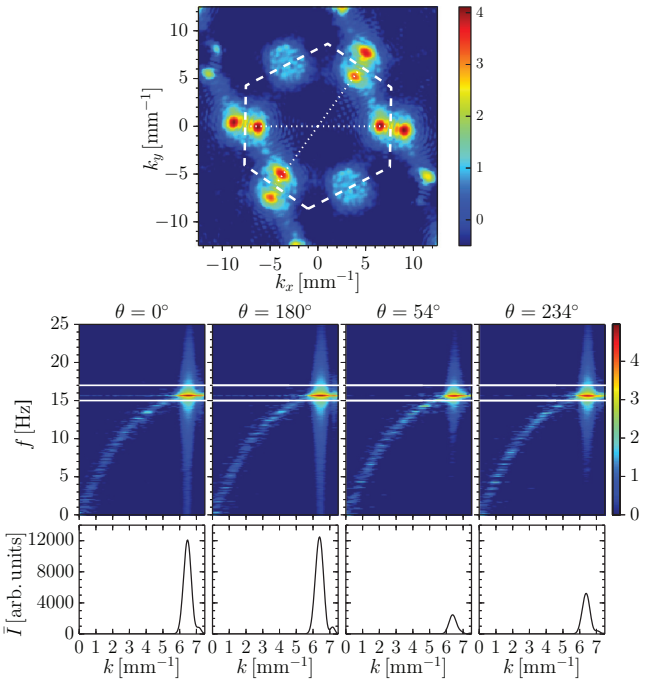

FIG. 2. Asymmetry of the MCI for compressed crystals. Top panel: Intensity $\bar{I}_{\mathbf{k}}$ of the velocity fluctuation spectrum in the $k_x k_y$ plane for the simulated data of run I (see Table I), averaged over the interval 15 Hz $< f <$ 17 Hz. The white dashed line indicates the border of the first Brillouin zone. The dotted lines with angles of $\theta = 0°, 54°$ measured from the x axis are shown to emphasize the symmetry of the hot-dot locations. Middle panels: Velocity fluctuation spectra as a function of k and f in the directions $\theta = 0°, 180°, 54°, 234°$. Bottom panels: Intensity of the fluctuation spectra shown in the middle panels, averaged over the range 15 Hz $< f <$ 17 Hz indicated by the horizontal lines. To compute the spectra, the first 25 s of the dynamical phase were used in a central region of the crystal containing about 800 particles. Only longitudinal modes are shown. The color bars are in a logarithmic scale with base 10 in arbitrary units.

the confinement strength [23]. The horizontal confinement of the crystal is often assumed to be insignificant in theoretical considerations; see, e.g., Refs. [17,39]. On the contrary, the finiteness and symmetry of the confinement have a great influence on the delicate symmetry breaking effects.

The cluster density and its spatial distribution varies with the strength of the horizontal confinement Ω_c, making the particle cluster internally inhomogeneous. It is not difficult to examine the character of this deformation. The confinement technique implemented in the simulations, caging the particle cluster in a parabolic potential, is actually well known, as well as the scaling laws controlling the structure of such Yukawa-interacting particle clusters; see, e.g., Refs. [29,40,41] and the references therein. According to Refs. [29,30,42] at fixed particle charge (Q), screening length (λ), and number of particles (N), the following approximate relationships hold:

$$\frac{c_l^2}{\Omega_c^2 R a} \propto \frac{a}{R} \propto \left(\frac{\kappa c_l}{c_q}\right)^2 \simeq \text{const}, \tag{5}$$

where c_l is the longitudinal sound speed, R the cluster size, a the crystal constant, $\kappa = a/\lambda$ the interaction range, $c_q = |Q|/\sqrt{M\lambda}$, and a "const" to the right means a function that rather weakly depends on κ. To the same accuracy, from Eq. (5) it follows immediately that

$$\Omega_c \kappa^2 \simeq \text{const}, \tag{6}$$

and the direct dependence of the cluster interaction range κ on the confinement strength becomes apparent. The large-scale density distribution is readily studied more rigorously, in analogy to Refs. [29,43], by minimizing the cluster interaction energy; see Appendix A for details.

Since the MCI threshold critically depends on the crystal interaction range κ [19], relationship Eq. (6) makes the critical vertical confinement $\Omega_{z,\text{crit}}$ (below which the instability is triggered) directly dependent on the horizontal confinement strength. It has been shown in Ref. [23] that

$$\frac{\delta\Omega_{z,\text{crit}}}{\Omega_{z,\text{crit}}} \approx \frac{\delta\Omega_c}{\Omega_c}. \tag{7}$$

Under the anisotropic loading, the horizontal confinement strength as well as the crystal interaction range are angle-dependent (elliptic-shaped; see Appendix B), and, as a consequence, the MCI ignition becomes anisotropic. Given the angular dependence of the crystal structure is rather weak (see Fig. 1), the spectral anisotropy of the MCI increment can be properly addressed by a modification of the "isotropic" MCI theory relationships [17]. The results of such simple implementation are shown in Fig. 3. Compared to the hexagonally symmetric HD distribution in the case of isotropic loading [Fig. 3(a)], the asymmetric loading [Figs. 3(b) and 3(c)] breaks the hexagonal symmetry. For an appropriate orientation of the loading direction α, the MCI is triggered in one direction, and only one pair of HD appears [see Fig. 3(b)] and a single oscillation pattern dominates. If the MCI is triggered in two directions, there are two pairs of HD and, therefore, two competing synchronization patterns. These observations agree very well with the experiments and simulations [20,23].

The distributions of Figs. 3(a)–3(c) explain fairly well all simulated and observed anisotropy effects but the rotational asymmetry of the measured spectra: The hot-dot "twins," which are oriented in opposite directions one to another, have exactly the same intensity in the model. This twofold symmetry is broken by adding a nonzero flux as we discuss below.

D. Phonon flux

The anisotropy of the compression phonon spectrum $I_{\mathbf{k},\omega}$ is directly related to the kinetic temperature gradient which is, in turn, proportional to the mean phonon flux $\langle \mathbf{u} \rangle$:

$$\left.\frac{\nabla T}{T}\right|_{\omega=\omega_{\text{HD}}} \propto \langle \mathbf{u} \rangle = \frac{\langle \mathbf{q} \rangle}{\mathcal{E}},$$
$$\langle \mathbf{q} \rangle = \int_{\Delta\omega} d\omega \int dk_x dk_y \, \omega \, \mathbf{u} \, \mathcal{N}_{\mathbf{k},\omega}, \; \mathbf{u} = \partial_{\mathbf{k}} \omega, \tag{8}$$
$$\mathcal{E} = \int_{\Delta\omega} d\omega \int dk_x dk_y \, \omega \mathcal{N}_{\mathbf{k},\omega}, \; \omega_{\mathbf{k}} \mathcal{N}_{\mathbf{k},\omega} = I_{\mathbf{k},\omega}.$$

Here $\mathcal{N}_{\mathbf{k},\omega}$ is the phonon number density, $\langle \mathbf{q} \rangle$ is the mean energy flux, $\mathcal{E}$ the total wave energy, $\mathbf{u}$ the phonon speed, and

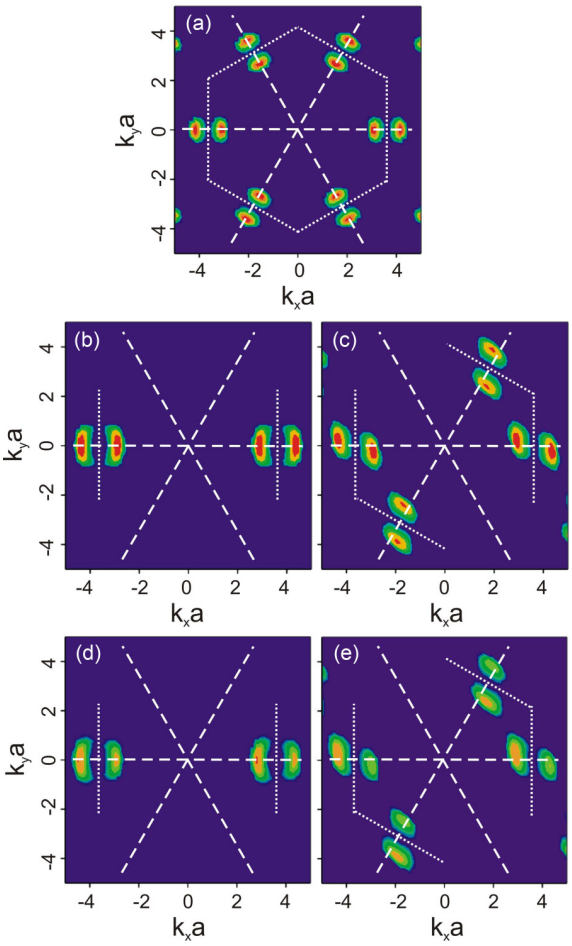

FIG. 3. Symmetry of the MCI increment in reduced $k_x k_y$ maps calculated for the theoretical model. In (a), the increment is calculated for isotropic loading as in Ref. [17]. In (b) and (c), there is an anisotropic loading of strength $p = 14\%$ in the direction $\alpha = 0^\circ$ and $\alpha = 30^\circ$, respectively. Panels (d) and (e) show the same as (b) and (c), only with a nonzero phonon flux in x direction. See Table II for the parameters of the calculation. The dashed and dotted lines indicate the main crystallographic directions and the first Brillouin zone boundary of the unperturbed lattice.

TABLE II. Asymmetry of the theoretical spectra. The lines correspond to the different panels in Fig. 3. The parameters Ω_z/Ω_Q and α were used to calculate the spectra. The wave group-to-phase velocity ratio at the hot dots $u/u_{\rm HD}$, the growth rate ratio of the twin hot dots $\delta\gamma/\langle\gamma\rangle$, and the hot-spot positions $\langle k_{\rm HD}a\rangle$ are calculated for the angles θ specified in the fourth row. The MCI increments are computed assuming $\delta/\lambda = 0.33$, $q/|Q| = 0.3$, $\kappa = 1$. Designations: $\Omega_Q = |Q|/\sqrt{M\lambda^3}$, $\delta\gamma/\langle\gamma\rangle = 2(\gamma_\theta - \gamma_{\theta+\pi})/(\gamma_\theta + \gamma_{\theta+\pi})$.

Panel	Ω_z/Ω_Q	α	θ	$u/u_{\rm HD}$	$\delta\gamma/\langle\gamma\rangle$	$\langle k_{\rm HD}\rangle a$
a	4.15	0	0	0	0	3.06
b	4.2	0	0	0	0	2.86
c	4.2	$\pi/6$	0	0	0	2.94
d	4.2	0	0	0.28	0.09	2.87
e	4.2	$\pi/6$	0	0.25	0.17	2.94
e	4.2	$\pi/6$	$\pi/3$	0.32	0.09	2.98

$\Delta\omega$ the MCI-resonance width. (Here, and further on, $\hbar = 1$ [44].) The distances of the HDs inside the fBz from the origin are approximately the same, $k \simeq k_{\rm HD}$, as well as the modulus of the phonon speeds $|\mathbf{u}| \simeq u_{\rm HD}$. The phonon speed directions and the HD intensities are principally different, though, due to the anisotropy of the MCI of the deformed crystal [23]. It results in a nonzero energy flux, in distinction to the perfect crystals where the flux is zero by symmetry of the MCI [17].

The main reason for a nonvanishing phonon flux in the distribution of $I_{\mathbf{k},\omega}$ shown in Fig. 2 is the energy difference of the quasisymmetric HDs, the "twins." There are only two such pairs of twins, one at $\theta \simeq 0^\circ$ and $\theta \simeq 180^\circ$, the other at $\theta \simeq 54^\circ$ and $\theta \simeq 234^\circ$. Using Eq. (8), the resulting phonon flux can be estimated from the spectrum shown in Fig. 2 as

$$\frac{\langle\mathbf{u}\rangle}{u_{\rm HD}} \approx -(0.06\mathbf{e}_1 + 0.13\mathbf{e}_2), \quad \frac{|\langle\mathbf{u}\rangle|}{u_{\rm HD}} \approx 0.17, \tag{9}$$

where $\mathbf{e}_{1,2} = \frac{\mathbf{u}}{u}|_{\theta=0,\frac{1}{3}\pi}$. The flux is normalized by the phonon speed $u_{\rm HD}$, which remains unknown in this approach. It must be approximated differently; see below. The angle $\arg(\langle\mathbf{u}\rangle/u_{\rm HD}) = 223^\circ$ is close to $\theta = 234^\circ$ as could be expected from Fig. 2.

Adding a nonvanishing phonon drift to the theoretical model results in an asymmetric, direction-dependent spectrum; see Figs. 3(d) and 3(e). Qualitatively (detailed analysis will be published elsewhere) a weak nonzero drift, say, along the main instability direction would result in a difference of the maximal phonon energy of the order of $\delta\omega_h \approx 2k_{\rm HD}u$, where $k_{\rm HD}$ is the HD (i.e., resonant) wave number, $k_{\rm HD}a < k_b a = 2\pi/\sqrt{3} \simeq 3.63$. Therefore, the resonant condition of the horizontal and vertical mode crossing would be satisfied a bit earlier at the "hotter" edge of the fBz:

$$\frac{\delta\Omega_{z,\rm crit}}{\Omega_{z,\rm crit}} \approx \frac{2k_{\rm HD}u}{\omega_{\rm HD}} = 2\xi_{\rm HD}\frac{u}{u_{\rm HD}}, \tag{10}$$

where $\xi_{\rm HD} = (u/u_{ph})_{\rm HD}$ is the compression wave group-to-phase velocity ratio (see Fig. 4). In the vicinity of the HDs, $u \ll \omega_{\rm HD}/k_{\rm HD}$ [17]; therefore, the magnitude of the effect is not large, as expected.

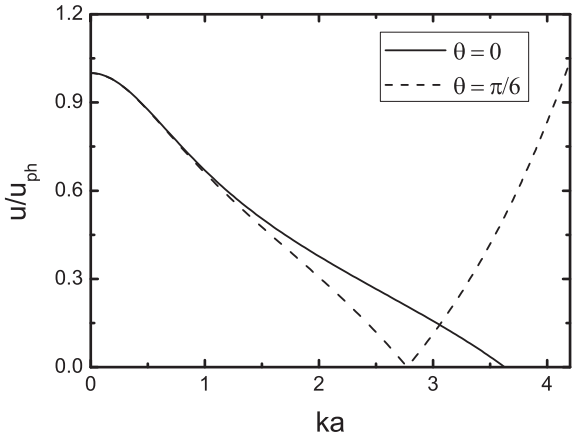

FIG. 4. Compression wave group-to-phase velocity ratio u/u_{ph} vs. reduced wave number ka calculated for the two directions $\theta = 0^\circ, 60^\circ$ [17]. For Fig. 2: $k_{\rm HD}a = 3.08$, $u/u_{ph}|_{\theta=0} \simeq u/u_{ph}|_{\theta=\frac{1}{3}\pi} \simeq 14\%$.

IV. POSSIBLE ORIGIN OF SYMMETRY BREAKING

The goal of this section is to properly address the question where the spectral asymmetry stems from. To answer this question it is necessary to thoroughly explore the main features of the HDs: (i) the structure of the velocity fluctuation spectra in reciprocal space, (ii) the energy distribution inside of the HDs, and (iii) the main dynamical processes responsible for the energy transport between the HDs.

A. HD twins: the universality of the anisotropy mechanism

To analyze the spectral asymmetry, a second crystal with a more pronounced asymmetry is considered. The simulation run II was performed for a smaller number of particles $N = 10\,000$; see Table I. While the larger crystal of run I equilibrates to a structure with large defect lines around the center, which reflects the sixfold symmetry of the lattice, the smaller crystal forms a less homogeneous dislocation pattern. The loading direction was set to $\alpha = 0°$, which selects only the HDs along the x axis at a weak MCI [23]. In order to activate the MCI also in the other directions, a smaller value of $f_z = 19.5$ Hz was used during the dynamical phase of run II.

In the beginning of the dynamical phase, the particle kinetic energy grows exponentially with a relatively small growth rate (see Fig 5, top panel). The fluctuation energy of the monolayer starts to collapse, leading to the emergence of multiple HDs (see Fig. 5, middle and bottom panels). After about 4 s, the growth rate changes to a larger value. At $t \approx 8$ s, the high kinetic energy of the particles leads to the breaking of the crystalline order.

The fluctuation spectrum reveals not only a pair of HD twins at $\theta \simeq 0°, 180°$ as in Ref. [23], a comparatively weaker pair at $\theta \simeq 56°, 236°$ is also present (see Fig 5). The HD twins of the weaker pair have very different intensities. This feature, in particular, is useful to demonstrate the universality of the anisotropic MCI. Figure 6 shows the intensities of the HDs at two different time steps. The chirality of the fluctuation pattern becomes apparent when comparing the respective twins at $\theta = 0°, 180°$ and $\theta = 56°, 236°$.

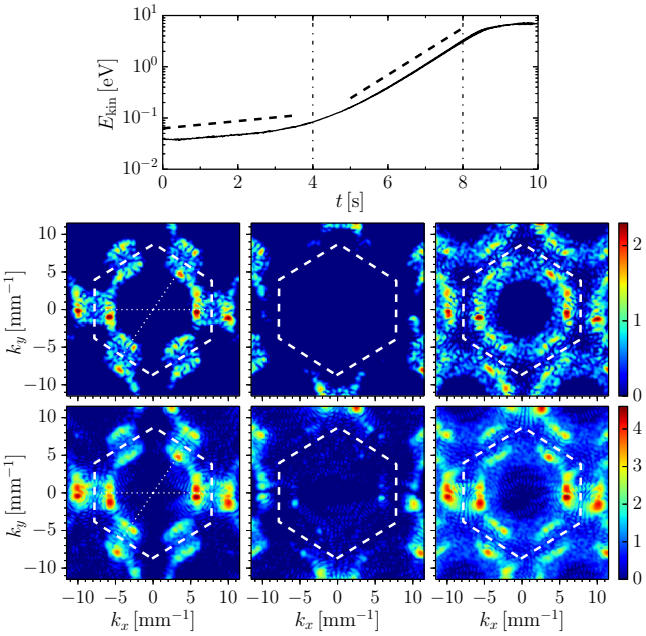

FIG. 5. Time evolution of velocity fluctuation spectra during the dynamical phase of simulation run II (see Table I). Top panel: Kinetic energy as a function of time t on a semilogarithmic scale. The vertical dash-dotted lines at $t = 4$ s and $t = 8$ s indicate the time intervals used for the calculation of the spectra. The dashed lines correspond to growth rates $\dot{E}/E = 0.17\,\mathrm{s}^{-1}$ and $1.1\,\mathrm{s}^{-1}$. Middle panels: Intensity of the fluctuation spectra $\bar{I}_{\mathbf{k}}$ for longitudinal (left), transverse horizontal (center), and transverse vertical (right) modes at $t = 4$ s, averaged over the frequency range $15\,\mathrm{Hz} < f < 17\,\mathrm{Hz}$ and color coded on a logarithmic scale in arbitrary units. The white dashed line indicates the border of the first Brillouin zone. White dotted lines appear for the longitudinal mode at angles of $\theta = 0°, 56°$. Bottom panels: The same for spectra calculated at $t = 8$ s. Note a weak hot-dot-induced shear intensity in the transverse horizontal mode for $t = 8$ s.

B. Hot-dot energy distribution

1. *Hot-dot core structure*

Despite the asymmetry in the energy distribution between the HDs evidenced above, all HDs are equally, though quite delicately, structured. The frequency-averaged energy distribution $\bar{I}_k$ in the main directions of the crystal consists of a core and a turbulent halo, as can be seen in Fig. 7. The core of the HD is well described by a Gaussian:

$$\bar{I}_k \propto \exp\left(-\frac{(k - k_{\mathrm{HD}})^2}{2\mu^2}\right). \tag{11}$$

The core, by energy content, is the dominant part of the HD, and, therefore, the width of the Gaussian core $\mu = \langle \delta k_{\mathrm{HD}}^2 \rangle^{\frac{1}{2}}$ can be ascribed to the size of the HD in $\mathbf{k}$ space. Typically, it is $\mu = 0.2$–$0.4\,\mathrm{mm}^{-1}$, that is, about 10–30 times smaller than the typical wave number of phonons comprising the HD, $\mu \ll k_{\mathrm{HD}} \simeq 6\mathrm{mm}^{-1}$; see Table III. It is a crucial feature of the MCI in the weakly nonlinear regime. Such an island-like distribution of the wave energy helps a lot to simplify the description of the wave dynamics. The gain of phonon energy is due to MCI, while the loss is due to diffusion activated by

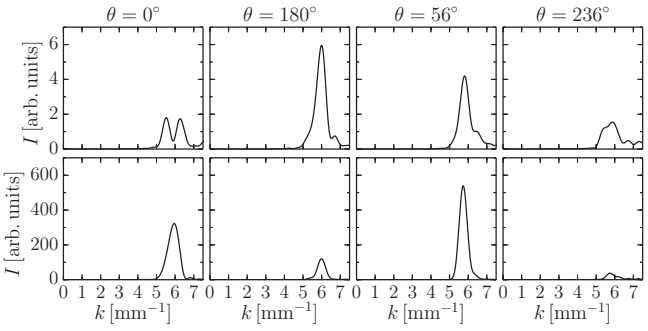

FIG. 6. Intensities of fluctuation spectra in the main directions of the crystal for the simulated data of run II. Top panels: $\bar{I}_{\mathbf{k}}$ calculated at $t = 4$ s at the angles of $\theta = 0°, 180°, 56°, 236°$, averaged over the frequency interval $15\,\mathrm{Hz} < f < 17\,\mathrm{Hz}$. Only the longitudinal mode was considered. Bottom panels: The same for a later time step $t = 8$ s.

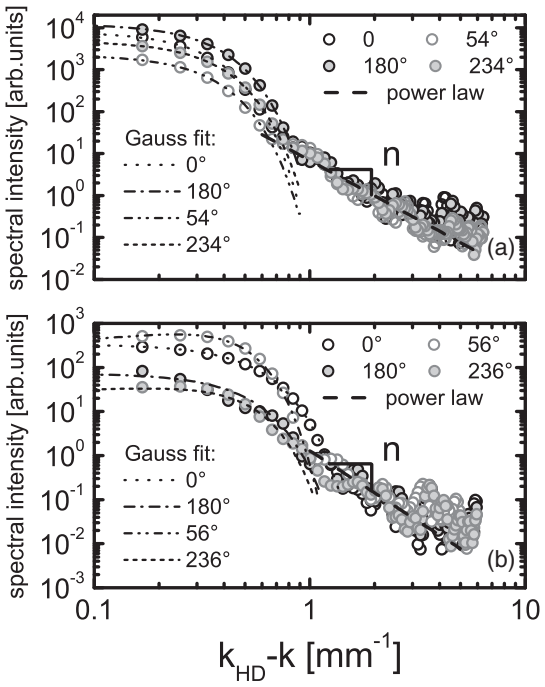

FIG. 7. Fine structure of the hot-dot energy distribution $\bar{I}_k$ for different directions θ as a function of deviation from the hot-dot center $k_{\rm HD} - k$. (a) Run I, $t = 25$ s of the dynamical phase; see Fig. 2. (b) Run II, $t = 8$ s of the dynamical phase; see Fig. 6. The cores of the hot dots are individually fitted to Gauss distributions, the widths μ are collected in Table III. The tails of the curves are fitted to a power law with exponent $n = 2.80 \pm 0.08$ (run I) and $n = 3.2 \pm 0.2$ (run II).

phonon scattering [62]:

$$\partial_t \bar{I}_k = \gamma_k^{\rm MCI} \bar{I}_k + \mathcal{D}^{(k)} \partial_k^2 \bar{I}_k, \tag{12}$$

where $\gamma_k^{\rm MCI}$ is the MCI increment and $\mathcal{D}^{(k)}$ is the diffusion coefficient in $\mathbf{k}$ space. Assuming a uniform energy gain, $\bar{I}_k \propto \exp(\gamma t)$, where γ is the actual growth rate of fluctuations, and making use of relationship Eq. (11), it is easy to observe that

$$\gamma = \gamma_k^{\rm MCI} + \frac{\mathcal{D}^{(k)}}{\mu^2}\left(\frac{\xi^2}{\mu^2} - 1\right), \quad \xi = k - k_{\rm HD}. \tag{13}$$

The excitation region is limited in size,

$$|k - k_{\rm HD}| \leqslant \xi_{\rm max} = \mu\sqrt{1 + \frac{\gamma\mu^2}{\mathcal{D}^{(k)}}}, \tag{14}$$

which is also in a fairly good agreement with theoretical model (see Fig. 3).

To make a numerical example, let us consider the data from run II. The theory of Ref. [17] predicts $\max[\gamma_k^{\rm MCI}] \simeq 5.26\,{\rm s}^{-1}$ for the parameter set of run II. The growth rate of the fluctuations can be approximated by the kinetic energy growth rate from Fig. 5. Given the averaged HD size $\langle\mu\rangle = 0.38\,{\rm mm}^{-1}$ and $\gamma = 0.17\,{\rm s}^{-1}$ at $0\,{\rm s} < t < 4\,{\rm s}$, from relationship Eqs. (13) and (14) it follows immediately for the diffusion coefficient $\mathcal{D}^{(k)} \simeq 0.73\,{\rm mm}^{-2}\,{\rm s}^{-1}$ and for the size of the excitation region $\xi_{\rm max} \simeq 0.39\,{\rm mm}^{-1}$. In the period $4\,{\rm s} < t < 8\,{\rm s}$, given $\langle\mu\rangle = 0.28\,{\rm mm}^{-1}$ and $\gamma = 1.1\,{\rm s}^{-1}$, it yields a lower value $\mathcal{D}^{(k)} \simeq 0.33\,{\rm mm}^{-2}\,{\rm s}^{-1}$, which is not surprising considering the enhanced energy growth rate. The size of the excitation region is estimated as $\xi_{\rm max} \simeq 0.31\,{\rm mm}^{-1}$.

The growth rates γ can also be obtained for each HD individually from the evolution of the fluctuation spectra, the resulting values for $\mathcal{D}^{(k)}$ and $\xi_{\rm max}$ are shown in Table III.

TABLE III. Characteristics of the hot-dot energy distribution. The time-averaged growth rate $\gamma = \langle \dot{I}/I \rangle$ is calculated from the velocity fluctuation spectra (see Figs. 2 and 6) for the direction given in the second column. The hot-dot size in k space, $\mu \equiv \langle \delta k_{\rm HD}^2 \rangle^{1/2}$, is obtained by using data of Fig. 7. The size of the excitation region $\xi_{\rm max}$ and the diffusion coefficient $\mathcal{D}^{(k)}$ in k space are estimated with Eqs. (13) and (14). γ was calculated at $t = 12.5$–25 s (run I) and $t = 4$–8 s (run II). The relative errors are 10% for γ, 5% for μ, 12% for $\xi_{\rm max}$, and 20% for $\mathcal{D}^{(k)}$.

Run	θ (°)	γ (s^{-1})	μ (mm^{-1})	$\xi_{\rm max}$ (mm^{-1})	$\mathcal{D}^{(k)}$ ($mm^{-2}\,s^{-1}$)
	0	0.34	0.20	0.21	0.20
I	180	0.35	0.22	0.23	0.24
	54	0.33	0.21	0.22	0.22
	234	0.47	0.22	0.23	0.23
	0	1.3	0.35	0.40	0.49
II	180	0.75	0.32	0.35	0.46
	56	1.2	0.21	0.24	0.18
	236	0.80	0.26	0.28	0.30

2. HD turbulent halo

The turbulent suprathermal halo, essentially an isotropic feature associated with every HD, is well recognizable in the log-log plot of Fig. 7 by an abrupt change in the slope of the energy spectrum. The fluctuation energy is power-law distributed in the halo, $\bar{I}_k \propto |k_{\rm HD} - k|^{-n}$. It is worth noting that the exponent deviates not much from the value $n \simeq 3$, which is typical for frictional turbulence [45–47]. It is natural to associate the appearance of these quanta at least partly with the Umklapp scattering of high-energy HD phonons. For quasiequilibrium situations this kind of scattering process is well studied; see, e.g., Ref. [48]. Note that the halo intensifies with time at the nonlinear stage of MCI.

C. Anisotropic phonon scattering by defects

By virtue of relationship Eq. (13), since the actual growth rates γ and the core sizes μ are only slightly different for HD twins (see Table III), the intensity asymmetry might also stem from the anisotropic phonon diffusivity governed, e.g., by anisotropic interaction of phonons and dislocations, or by Umklapp processes that lead to a loss of high-energy HD quanta. We start with an analysis of the role of the defects.

1. Role of defects

Phonon scattering on defects, apart from nonlinear phonon interactions and finite-size effects, is known as one possible mechanism of energy redistribution between the phonons and their anisotropic transport [49–51]. It is also a well-known fact that the anisotropy of the thermal conductivity is closely connected to the special features of the phonon spectra

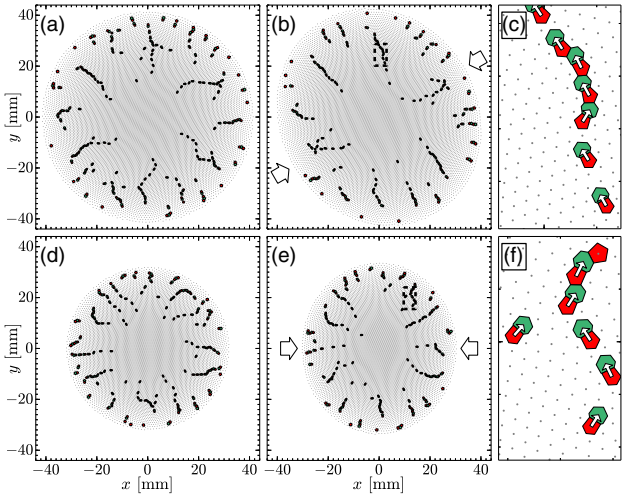

FIG. 8. Asymmetric dislocation pattern of the compressed crystals. Shown is the crystal of simulation run I at the beginning of the deformation phase (a) and at the beginning of the dynamical phase (b). The dashed square is magnified by a factor of 10 in (c). The particle positions are shown as gray dots, and the Voronoi cells of the fivefold and sevenfold defects are shown in red (dark gray) and green (light gray), respectively. In (c), the dipoles **d** as defined in the text are also shown as white arrows. Note an apparent trend of dislocation chains to align transversally to the compression direction α, which is indicated by arrows in (b). (d)–(f) The dislocation patterns for run II.

determined by phonon scattering by oriented dislocations [52]. For instance, no interaction occurs between the longitudinal wave and the dislocation when an incident wave propagating in a direction parallel or perpendicular to the Burgers vector [50]. If the phonon flux is normal to the orientation of chains of dislocations, the scattering is stronger [51].

The anisotropic heat transport in a plasma crystal has been studied in Refs. [10,11]. In our simulated crystals phonon scattering by defects might be quite well pronounced because the dislocation chains [53,54] (or dislocation "scars" [55]) that form during the equilibration and deformation phases exhibit a preferred orientation, which tends to be perpendicular to the direction of dominant loading. This is evidenced in Fig. 8, where snapshots of the two simulation runs at the beginning of the deformation phase and of the dynamical phase are shown.

If the dislocation pattern inside the crystal is random, the wave is only expected to be attenuated through diffusive scattering. If, however, the pattern is asymmetric, phonon scattering can lead to a broken parity symmetry. To measure the asymmetry in the dislocation pattern, we calculate the center of mass $\mathbf{R}_d = \langle \mathbf{r}_7 \rangle$, where $\mathbf{r}_7$ are the positions of the sevenfold defect cells. The apparent defects at the very border of the crystal are not considered for the calculation. Magnitude and argument of this vector are indicated in Table IV for the defect patterns shown in Fig. 8. It can be seen that both values change drastically during the deformation phase of run I. Still, the magnitude $|\mathbf{R}_d|$ stays relatively small. Despite the smaller crystal size in run II, the value of $|\mathbf{R}_d|$ is larger, indicating a more pronounced inhomogeneity of the dislocation pattern.

TABLE IV. Center of mass $\mathbf{R}_d$ and polarization **D** of the dislocation patterns shown in Fig. 8. See text for the definitions.

Run	Phase	$\lvert\mathbf{R}_d\rvert$ (mm)	arg($\mathbf{R}_d$) (°)	$\lvert\mathbf{D}\rvert$ (mm)	arg(**D**) (°)
I	Deformation	0.57	110	1.0	354
I	Dynamical	1.3	19	5.6	14
II	Deformation	1.3	81	5.7	76
II	Dynamical	1.1	90	4.3	169

2. *Polarized dislocation patterns*

When considering the influence of defects, it is important to note that their positions in the monolayer follow certain patterns closely connected to the external confinement. Every dislocation consists of a coupled pair of sevenfold and fivefold cells. It is characterized by the Burgers vector **b**, whose orientation defines the dislocation gliding direction [56], or, equivalently, by the dislocation dipole vector, traditionally introduced as $\mathbf{d} = \mathbf{r}_7 - \mathbf{r}_5$ [57], where $\mathbf{r}_{7,5}$ are the positions of the centers of the sevenfold and fivefold defect cells. For a single dislocation in an otherwise ideal lattice, $\mathbf{d} = \mathbf{b} \times \mathbf{e}_z$. Any applied external force with a nonzero component along the Burgers vector (transversal to the dipole vector) causes dislocation *glide* [56]. (Dislocation transversal *creep* is much less probable). For both run I and run II, the slip events are rare and the dislocation patterns are quasistationary even during the dynamical phase.

A curious peculiarity is evident at close observation of the dislocation pattern: The majority of the dislocation pairs are ordered in such a way that their fivefold components are located closer to the cluster center than their sevenfold counterparts [see Figs. 8(c) and 8(f)]. The system of dislocation dipoles is therefore polarized by the external confinement. To quantify this effect, the global polarization is calculated as $\mathbf{D} = \sum \mathbf{d}$, where the sum is performed over all polarization vectors **d**. We follow a rather simple rule for counting the polarization vectors. In chains of more than two defects, going radially outward, each sevenfold defect is connected to at most one fivefold defect. In cases where there are more fivefold defects than sevenfold defects, as in the upper part of Fig. 8(f), the outmost defect is thus not considered. The magnitude and argument of **D** are shown in Table IV. $|\mathbf{D}|$ increases substantially during the deformation phase of run I. Similar to the development of $|\mathbf{R}_d|$, the magnitude of the average polarization slightly decreases from an initially relatively large value during the deformation phase of run II.

D. Asymmetric Umklapp scattering

If the crystal is perfect, without defects or strains in its structure, the scattering of phonons will only be caused by three-phonon processes in which two phonons coalesce to give one, or one splits up to give two [58,59]. Such nonlinear phonon scattering can be described by integral equations (see, e.g., Ref. [44]), which take into account the *Umklapp* processes, or U processes, that result from the periodicity of the lattice [58,59]. Three-phonon U processes are known as the main intrinsic thermalresistive processes in crystals [60].

They are apparently important and unavoidable during MCI in a plasma crystal because this instability generates phonons dominantly in the very proximity of the fBz boundary [17]. For instance, in Fig. 2, the energy of the wave fluctuations is concentrated at $k_{\mathrm{HD}}a > k_b a/2$, which is close to the fBz boundary $k_b a = 2\pi/\sqrt{3}$. The second harmonic must be expected at $k_s a \simeq 2k_{\mathrm{HD}}a - 2k_b a < 0$, that is, in the opposite direction due to a U process. The high-energy fundamental phonons, when coalesced, should formally disappear. On the other hand, elimination of high-energy phonons by Umklapp processes can be well compensated by the generation caused by the MCI.

The U processes are less important at the initial stage of the instability since U processes are three-wave interactions leading to the generation of second harmonics, hence, they are at least of the second order by perturbation amplitude [61]. At this stage, the anisotropic scattering by dislocations could be the only cause of spectral asymmetry.

Further on, at the weakly nonlinear stage of MCI, U scattering intensifies and, in analogy with Ref. [48], scattering of HD phonons caused by U processes leads mainly to the relaxation of their distribution function, that is, to an effective nonlinear damping. The phonon fluxes of two hot-dot twins are not negligible, though mainly counter-directed. An important contribution to the phonon drift is thus only possible if the spectral pattern is asymmetric.

V. CONCLUSION

The main features in the particle current fluctuation spectra (which are also observed in the experiments of Ref. [20]) were reproduced by a simple theoretical model incorporating the angle-dependence of the crystal interaction range. An anisotropic confinement of the crystal enhances the MCI increment in the direction of the compression and leads to hot dots of different intensities. The broken left-right symmetry of pairs of hot dots (twins) was reproduced by taking into account a nonvanishing phonon flux.

Two possible explanations for such a mean phonon flux were presented. The first one is the Umklapp process resulting in a turbulent power-law distributed halo surrounding the hot dots. Phonon scattering by defects was presented as a second mechanism producing a phonon flux. The analysis of the dislocation pattern showed that most pairs of fivefold and sevenfold defects are "polarized" such that their fivefold components are located closer to the cluster center. Simple measures relying on the center of mass and dipole moment of the defect pattern were proposed to quantify the influence of this effect. A more detailed analysis of the structure of the defect chains will be necessary for further insights.

It depends mostly on the symmetry of the hot-dot positions in the first Brillouin zone whether the total phonon drift caused by Umklapp processes cancels or not. For a highly ordered hot-dot pattern (see Fig. 2) this is certainly the case, and the nonvanishing phonon drift originates mainly from an anisotropic scattering by dislocations rather than Umklapp processes.

For a less symmetric pattern of hot dots (see Fig. 5), the situation is not that simple. The hot-dot twins are not only different in their energy content, but they are also positioned asymmetrically in the first Brillouin zone. Umklapp scattering may thus be another reason for the systematic phonon drift in run II. The different growth rates of the kinetic energy observed in Fig. 5 may hint toward a transition from an initial regime where the phonon flux is dominated by scattering on defects to a regime where three-phonon Umklapp scattering plays an important role. Analyzing higher harmonics of the hot dots may give additional insights, which will be subject to further studies.

To conclude, we have analyzed the spectral asymmetry of compressed plasma crystals. The finiteness of the crystal was explicitly taken into account, since it has an impact on the hot-dot positions in reciprocal space and enables the formation of an ordered dislocation pattern. Both effects can explain the spectral asymmetry observed in experiments and simulations.

ACKNOWLEDGMENTS

We thank Lénaïc Couëdel for helpful discussions. This work was supported by the German Federal Ministry for Economy and Technology under Grant No. 50WM1441 and by the European Research Council under the European Union's Seventh Framework Programme (FP7/2007-2013)/ERC Grant Agreement No. 267499.

APPENDIX A: INTERACTION ENERGY MINIMIZATION

The energy of the two-dimensional N-particle "cold" cluster (assuming the infinitely strong vertical confinement) in a parabolic well is

$$W = \frac{1}{2}Q^2 \sum_{i\neq j}^{N} R_{i,j}^{-1} \exp(-\lambda^{-1} R_{i,j}) + \frac{1}{2} M\Omega_c^2 \sum_{i}^{N} r_i^2, \quad \text{(A1)}$$

where $R_{i,j} = |\mathbf{r}_i - \mathbf{r}_j|, i, j = 1 \ldots N$, and N is the number of particles. To minimize the cluster energy, one has to consider the system of N equations $\delta_{\mathbf{r}_i} W = 0, i = 1 \ldots N$, which can be solved numerically provided that N is not too large. Equation (A1) can be significantly simplified in the mean-field approximation. The sums over particle positions are replaced by integrals over the particle number density per unit area, $n(\mathbf{r})$, where the integration is performed over the cluster area S_c [29]:

$$\begin{aligned} W &= W_{\mathrm{int}} + W_{\mathrm{ext}}, \\ W_{\mathrm{int}} &= \frac{1}{2}Q^2 \int_{S_c} d\mathbf{r}' d\mathbf{r} n(\mathbf{r}') n(\mathbf{r}) R^{-1} \exp(-\lambda^{-1} R), \\ W_{\mathrm{ext}} &= \frac{1}{2} M\Omega_c^2 \int_{S_c} d\mathbf{r} n(\mathbf{r}) r^2, \\ N &= \int_{S_c} d\mathbf{r} n(\mathbf{r}). \end{aligned} \quad \text{(A2)}$$

In order to validate relationship Eq. (6), it is enough to consider a uniform number density distribution,

$$n(r) = \begin{cases} \langle n \rangle & \text{for} \quad r \leqslant R_c \\ 0 & \text{for} \quad r > R_c \end{cases}, \quad \text{(A3)}$$

where R_c is the cluster radius and $\langle n\rangle \propto a^{-2}$ the mean cluster number density. Under this assumption, one obtains

$$N = \langle n\rangle S_c, \quad W_{\rm ext} = \frac{1}{4\pi} M N S_c \Omega_c^2. \tag{A4}$$

To calculate $W_{\rm int}$, let us recall the useful relationship:

$$\begin{aligned} R^{-1}\exp(-\lambda^{-1}R) &= \lambda\int_0^\infty \frac{kdk}{\sqrt{1+k^2\lambda^2}} J_0(kR), \\ J_0(kR) &= J_0(kr)J_0(kr') \\ &\quad + 2\sum_{s=1}^{\infty} J_s(kr)J_s(kr')\cos(\phi), \\ R &= \sqrt{r^2+r'^2-2rr'\cos(\phi)}, \end{aligned} \tag{A5}$$

where J_s is the Bessel function. Then

$$W_{\rm int} = \frac{q^2N^2}{\lambda} F(\xi), \quad F(\xi) = \int_0^\infty \frac{2\xi dk}{k\sqrt{1+\xi k^2}} J_1^2(k), \tag{A6}$$

where $\xi = S_\lambda/S_c$, $S_\lambda = \pi\lambda^2$. For large cluster (as normally the case in experiments and simulations) $\xi \ll 1$, therefore $F(\xi) \simeq \xi$, $W_{\rm int} \simeq \frac{q^2N^2}{\lambda}\xi$, and the total cluster energy is

$$W = W_{\rm ext} + W_{\rm int} = \frac{1}{4\pi} M N S_c \Omega_c^2 + \frac{q^2N^2}{\lambda}\frac{S_\lambda}{S_c}. \tag{A7}$$

The total energy W as a function of S_c has a minimum at

$$S_c = 2S_\lambda\sqrt{N}\frac{\Omega_q}{\Omega_c}, \tag{A8}$$

if all other parameters are kept fixed. Since $S_c/S_\lambda \propto \kappa^2$ we have $\kappa^2 \propto \Omega_c^{-1}$, restoring Eq. (6).

APPENDIX B: SQUEEZED CLUSTER: ECCENTRICITY OF THE STRUCTURE

Let us consider the slightly deformed crystal assuming an elliptic-shaped confining well:

$$\Omega_c = \Omega_c(\theta) = \Omega_{c,0}\sqrt{1+p\cos(2\theta)}, \quad p \ll 1, \tag{B1}$$

with p as an asymmetry measure and an eccentricity:

$$e_c^2 = \frac{2p}{1+p} \equiv 1 - \frac{\Omega_{c,\min}^2}{\Omega_{c,\max}^2}, \tag{B2}$$

By virtue of Eq. (6), the crystal interaction range is also weakly angle-dependent:

$$\kappa = \kappa(\theta) = \frac{\kappa_0}{\sqrt[4]{1+p\cos(2\theta)}}. \tag{B3}$$

The eccentricity of this distribution is

$$e_\kappa^2 = 1 - \frac{\kappa_{c,\min}^2}{\kappa_{c,\max}^2} \equiv 1 - \frac{\Omega_{c,\min}}{\Omega_{c,\max}}. \tag{B4}$$

In Eqs. (B1) and (6), $\Omega_{c,0}$ and κ_0 are angle-independent constants. They can be related to the "unperturbed" crystal. For instance, for a pure shear deformation a constraint,

$$2\pi\kappa_{p=0}^2 = \int_0^{2\pi}\kappa^2(\theta)d\theta = \kappa_0^2\int_0^{2\pi}\frac{d\theta}{\sqrt{1+p\cos(2\theta)}}, \tag{B5}$$

allows one to obtain the interaction range $\kappa_0 = \kappa_0(p)$ for any given asymmetry parameter p through $\kappa_{p=0}^2$ of the unperturbed crystal.

[1] J. H. Chu and L. I, Phys. Rev. Lett. **72**, 4009 (1994).
[2] H. Thomas, G. E. Morfill, V. Demmel, J. Goree, B. Feuerbacher, and D. Möhlmann, Phys. Rev. Lett. **73**, 652 (1994).
[3] Y. Hayashi and K. Tachibana, Jpn. J. Appl. Phys. **33**, L804 (1994).
[4] V. E. Fortov, A. V. Ivlev, S. A. Khrapak, A. G. Khrapak, and G. E. Morfill, Phys. Rep. **421**, 1 (2005).
[5] G. E. Morfill and A. V. Ivlev, Rev. Mod. Phys. **81**, 1353 (2009).
[6] H. M. Thomas and G. E. Morfill, Nature (London) **379**, 806 (1996).
[7] V. A. Schweigert, I. V. Schweigert, A. Melzer, A. Homann, and A. Piel, Phys. Rev. Lett. **80**, 5345 (1998).
[8] S. Nunomura, D. Samsonov, and J. Goree, Phys. Rev. Lett. **84**, 5141 (2000).
[9] T. Misawa, N. Ohno, K. Asano, M. Sawai, S. Takamura, and P. K. Kaw, Phys. Rev. Lett. **86**, 1219 (2001).
[10] S. Nunomura, D. Samsonov, S. Zhdanov, and G. Morfill, Phys. Rev. Lett. **95**, 025003 (2005).
[11] V. Nosenko, S. Zhdanov, A. V. Ivlev, G. Morfill, J. Goree, and A. Piel, Phys. Rev. Lett. **100**, 025003 (2008).
[12] K. O. Menzel, O. Arp, and A. Piel, Phys. Rev. Lett. **104**, 235002 (2010).
[13] J. D. Williams, Phys. Rev. E **90**, 043103 (2014).
[14] H. Ikezi, Phys. Fluids **29**, 1764 (1986).
[15] A. Melzer, V. A. Schweigert, and A. Piel, Phys. Rev. Lett. **83**, 3194 (1999).
[16] A. V. Ivlev and G. Morfill, Phys. Rev. E **63**, 016409 (2000).
[17] S. K. Zhdanov, A. V. Ivlev, and G. Morfill, Phys. Plasmas **16**, 083706 (2009).
[18] L. Couëdel, V. Nosenko, A. V. Ivlev, S. K. Zhdanov, H. M. Thomas, and G. E. Morfill, Phys. Rev. Lett. **104**, 195001 (2010).
[19] L. Couëdel, S. K. Zhdanov, A. V. Ivlev, V. Nosenko, H. M. Thomas, and G. E. Morfill, Phys. Plasmas **18**, 083707 (2011).
[20] L. Couëdel, S. Zhdanov, V. Nosenko, A. V. Ivlev, H. M. Thomas, and G. E. Morfill, Phys. Rev. E **89**, 053108 (2014).
[21] C. Reichhardt and C. J. O. Reichhardt, Europhys. Lett. **68**, 303 (2004).
[22] T. Bohlein and C. Bechinger, Phys. Rev. Lett. **109**, 058301 (2012).
[23] I. Laut, C. Räth, S. Zhdanov, V. Nosenko, L. Couëdel, and H. M. Thomas, Europhys. Lett. **110**, 65001 (2015).
[24] D. Samsonov, S. Zhdanov, and G. Morfill, Phys. Rev. E **71**, 026410 (2005).
[25] Y. Kuramoto and D. Battogtokh, Nonlinear Phenom. Complex Syst. **5**, 380 (2002).
[26] D. M. Abrams and S. H. Strogatz, Phys. Rev. Lett. **93**, 174102 (2004).
[27] A. E. Motter, Nat. Phys. **6**, 164 (2010).

[28] A. M. Hagerstrom, T. E. Murphy, R. Roy, P. Hövel, I. Omelchenko, and E. Schöll, Nat. Phys. **8**, 658 (2012).
[29] H. Totsuji, C. Totsuji, and K. Tsuruta, Phys. Rev. E **64**, 066402 (2001).
[30] S. K. Zhdanov, M. H. Thoma, and G. E. Morfill, New J. Phys. **13**, 013039 (2011).
[31] A. V. Ivlev, U. Konopka, G. E. Morfill, and G. Joyce, Phys. Rev. E **68**, 026405 (2003).
[32] T. B. Röcker, A. V. Ivlev, S. K. Zhdanov, and G. E. Morfill, Phys. Rev. E **89**, 013104 (2014).
[33] S. Zhdanov, R. A. Quinn, D. Samsonov, and G. E. Morfill, New J. Phys. **5**, 74 (2003).
[34] T. E. Sheridan, Phys. Plasmas **15**, 103702 (2008).
[35] T. E. Sheridan, Phys. Plasmas **16**, 083705 (2009).
[36] P. Schofield, Comput. Phys. Commun. **5**, 17 (1973).
[37] D. Beeman, J. Comput. Phys. **20**, 130 (1976).
[38] Z. Donkó, G. J. Kalman, and P. Hartmann, J. Phys. Condens. Matter **20**, 413101 (2008).
[39] A. V. Ivlev, T. B. Röcker, L. Couëdel, V. Nosenko, and C.-R. Du, Phys. Rev. E **91**, 063108 (2015).
[40] C. Durniak and D. Samsonov, Phys. Rev. Lett. **106**, 175001 (2011).
[41] C. Durniak, D. Samsonov, J. F. Ralph, S. Zhdanov, and G. Morfill, Phys. Rev. E **88**, 053101 (2013).
[42] F. M. Peeters and X. Wu, Phys. Rev. A **35**, 3109 (1987).
[43] D. H. E. Dubin, Phys. Rev. E **55**, 4017 (1997).
[44] E. M. Lifshitz and L. P. Pitaevskii, *Physical Kinetics* (Pergamon, Oxford, 1981).
[45] U. Frisch, *Turbulence: The Legacy of A. N. Kolmogorov* (Cambridge University Press, Cambridge, 1995).
[46] M. Schwabe, S. Zhdanov, C. Räth, D. B. Graves, H. M. Thomas, and G. E. Morfill, Phys. Rev. Lett. **112**, 115002 (2014).
[47] S. Zhdanov, M. Schwabe, C. Räth, H. M. Thomas, and G. E. Morfill, Europhys. Lett. **110**, 35001 (2015).
[48] K. A. Matveev, A. V. Andreev, and M. Pustilnik, Phys. Rev. Lett. **105**, 046401 (2010).
[49] B. Yang and G. Chen, Phys. Rev. B **67**, 195311 (2003).
[50] A. Maurel, J.-F. Mercier, and F. Lund, J. Acoust. Soc. Am. **115**, 2773 (2004).
[51] A. Maurel, V. Pagneux, D. Boyer, and F. Lund, Proc. R. Soc. London A **462**, 2607 (2006).
[52] N. V. Lugueva and S. M. Luguev, High Temp. **42**, 54 (2004).
[53] C. A. Knapek, D. Samsonov, S. Zhdanov, U. Konopka, and G. E. Morfill, Phys. Rev. Lett. **98**, 015004 (2007).
[54] C. A. Knapek, C. Durniak, D. Samsonov, and G. E. Morfill, Phys. Rev. Lett. **110**, 035001 (2013).
[55] X. S. Ling, Nat. Mater. **4**, 360 (2005).
[56] C. Kittel, *Introduction to Solid State Physics*, 5th ed. (Wiley, New York, 1976)
[57] J. Paulose, B. G. Chen, and V. Vitelli, Nat. Phys. **11**, 153 (2015).
[58] R. Peierls, Ann. Physik **395**, 1055 (1929).
[59] R. Berman, F. E. Simon, and J. Wilks, Nature (London) **168**, 277 (1951).
[60] Y.-J. Han, Phys. Rev. B **54**, 8977 (1996).
[61] N. Bloembergen, *Nonlinear Optics: A Lecture Note and Reprint Volume* (Benjamin Inc., New York, 1965).
[62] We simplified the description omitting the gradient term from the Fokker-Plank Eq. (12). This term, though it might be important to explain a weak asymmetry of the HD core (see, e.g., Fig. 6), is small compared to the term accounting for diffusion.

Wake-mediated propulsion of an upstream particle in two-dimensional plasma crystals (Ref. [121])

I. Laut, C. Räth, S. Zhdanov, V. Nosenko, G. Morfill and H. Thomas. *Wake-mediated propulsion of an upstream particle in two-dimensional plasma crystals*, Physical Review Letters **118**, 075002 (2017) https://doi.org/10.1103/PhysRevLett.118.075002
©2017 American Physical Society

Wake-Mediated Propulsion of an Upstream Particle in Two-Dimensional Plasma Crystals

I. Laut,[1,*] C. Räth,[1] S. K. Zhdanov,[1] V. Nosenko,[1] G. E. Morfill,[2,3] and H. M. Thomas[1]
[1]*Institut für Materialphysik im Weltraum, Deutsches Zentrum für Luft- und Raumfahrt (DLR), 82234 Weßling, Germany*
[2]*Max Planck Institute for Extraterrestrial Physics, 85741 Garching, Germany*
[3]*BMSTU Centre for Plasma Science and Technology, Moscow 105005, Russia*
(Received 17 October 2016; published 14 February 2017)

The wake-mediated propulsion of an "extra" particle in a channel of two neighboring rows of a two-dimensional plasma crystal, observed experimentally by Du *et al.* [Phys. Rev. E **89**, 021101(R) (2014)], is explained in simulations and theory. We use the simple model of a pointlike ion wake charge to reproduce this intriguing effect in simulations, allowing for a detailed investigation and a deeper understanding of the underlying dynamics. We show that the nonreciprocity of the particle interaction, owing to the wake charges, is responsible for a broken symmetry of the channel that enables a persistent self-propelled motion of the extra particle. We find good agreement of the terminal extra-particle velocity with our theoretical considerations and with experiments.

DOI: 10.1103/PhysRevLett.118.075002

Introduction.—In ion beam physics, channeling effects can strongly influence the motion of ions or other charged particles in a crystalline solid [1,2]. Similarly, neutral atoms can be channeled in a standing wave of laser light [3,4]. In complex plasma crystals, experimental observations of the channeling effect showed that instead of slowing down, an extra particle *accelerates* in the channel [5–7]. This persistent motion was attributed to the nonreciprocity of the particle interactions but the exact origin of the propulsion was not resolved [5]. (Self-)propelled motion currently receives considerable attention both in macroscopic [8] and microscopic [9,10] systems.

Complex plasmas consist of micron-sized particles that are immersed in a weakly ionized gas. In a laboratory radio-frequency (rf) plasma, the particles are usually negatively charged and levitate in the plasma sheath region above the lower electrode where the gravitational force is balanced by the electric field. Thus confined, these strongly coupled systems can form two-dimensional (2D) crystalline structures which are called *plasma crystals* [11,12]. Large three-dimensional crystals can only be obtained under microgravity conditions, for example, during parabolic flights [13] or onboard the International Space Station [14]. Both two- and three-dimensional plasma crystals are ideal model systems for phase transitions [15,16], wave processes [17,18], and self-organization [19,20], as their dynamics can be resolved at the level of individual particles.

The sheath electric field not only levitates the crystal, but also causes an ion flow that strongly influences the particle interaction. In the bulk plasma, far away from the rf electrodes, the particle interaction is well described by a screened Coulomb (Yukawa) potential since the charged particles are surrounded by a cloud of positively charged ions [21]. In the sheath region, however, the downward-flowing ions distort the screening cloud, leading to a positive excess charge below each particle. This *ion wake* adds an attractive component to the mutual particle interactions [22] and makes them nonreciprocal. Ion wakes cause interesting effects like the formation of particle strings in a vertically extended system [23], the mode-coupling instability in a monolayer [24] and the coexistence of two distinct kinetic temperatures in a binary mixture [25]. A common way to model the ion wake is by a positive pointlike charge that is positioned a fixed distance below each particle. The intuitive picture of a pointlike wake charge allows for the rigorous analysis of the mode-coupling instability [26] and of the slightly bowl-like shape [27] of plasma crystal monolayers.

It was suggested that the ion wake be also responsible for the channeling effect in plasma crystals that was first observed in experiments by Du *et al.* [5], but the exact driving mechanism was not known. An "extra" particle floated slightly above the plasma crystal (*upstream* with respect to the ion flow) and followed the channel formed by lines of neighboring particles. Despite ambient gas friction, the particle moved at a nearly constant velocity, provoking lateral waves and an increase of kinetic temperature in the crystal [5,6].

In this Letter, we reproduce in simulations the wake-mediated propulsion of an upstream extra particle in a 2D plasma crystal. We use the simple model of a pointlike ion wake charge which enables an intuitive picture and an analytical analysis of the underlying dynamics. The attraction between the extra-particle wake and the particles in the crystal results in a symmetry-breaking deformation of the channel which accelerates the extra particle. We study the terminal velocity reached by the propulsion process and compare it to our theoretical considerations and to experiments.

Simulation particulars.—Molecular-dynamics (MD) simulations are well suited for modeling the dynamical

 © 2017 American Physical Society

effects in complex plasmas [28–31]. In the simulation of a 2D plasma crystal in the horizontal xy plane, the equation of motion for particle i reads

$$M\ddot{\mathbf{r}}_i + M\nu\dot{\mathbf{r}}_i = \sum_{j\neq i}\mathbf{F}_{ji} + \mathbf{C}_i^{p,t} + \mathbf{L}_i, \tag{1}$$

where $\mathbf{r}_i$ is the three-dimensional particle position, M the mass, and ν the damping rate. The forces acting on the particle are the mutual particle interactions $\mathbf{F}_{ji}$, the confinement force $\mathbf{C}_i^{p,t}$ derived from an external potential, and a Langevin heat bath $\mathbf{L}_i$.

To include the ion wake in the mutual particle interaction, a positive pointlike charge q is placed a fixed vertical distance δ below each particle, while the particle itself is modeled as a negative pointlike charge $Q<0$. The force exerted by particle j (and its wake) on particle i is thus modeled as

$$\mathbf{F}_{ji} = Q^2 f(r_{ji})\frac{\mathbf{r}_{ji}}{r_{ji}} + qQf(r_{w_{ji}})\frac{\mathbf{r}_{w_{ji}}}{r_{w_{ji}}} \equiv F_p\frac{\mathbf{r}_{ji}}{r_{ji}} + F_w\frac{\mathbf{r}_{w_{ji}}}{r_{w_{ji}}}, \tag{2}$$

where $f(r)=\exp(-r/\lambda)(1+r/\lambda)/r^2$, λ the screening length, $\mathbf{r}_{ji}=\mathbf{r}_i-\mathbf{r}_j$ and $\mathbf{r}_{w_{ji}}=\mathbf{r}_i-(\mathbf{r}_j-\delta\mathbf{e}_z)$. Here and in the following, r denotes the magnitude of vector $\mathbf{r}$, and $\mathbf{e}_{x,y,z}$ are the unit vectors of the coordinate system.

The confinement force reads $\mathbf{C}_i^{p,t}=-\boldsymbol{\nabla}(V_i^{p,t}+V_i^z)$, where $V_i^{p,t}$ is the horizontal confinement and V_i^z the vertical confinement. Very regular crystals with few defects are obtained with a horizontal tenth-order potential $V_i^t=0.5M\Omega_h^2\rho_i^{10}/R^8$, where $\rho_i=\sqrt{x_i^2+y_i^2}$ is the horizontal position of particle i and R is approximately the radius of a crystal with the same number of particles in a parabolic horizontal confinement with frequency Ω_h [32]. The parabolic horizontal potential $V_i^p=0.5M\Omega_h^2\rho_i^2$ leads to a crystal where the interparticle distance increases with the distance from the crystal center [28,29,31]. While the global structure of a plasma crystal is well described by a parabolic confinement [33], the tenth-order potential is well suited to reproduce the regular central region.

The vertical confinement of the particles stems from the interplay of the gravitational force and the electrostatic forces of the sheath field which are oriented in opposite directions. This strong confinement is often modeled as a parabolic confinement $V_i^z=0.5M\Omega_z^2(z_i-z_{\mathrm{eq}})^2$, where the equilibrium position is $z_{\mathrm{eq}}=0$ [28,29,34]. In order to reproduce an upstream particle in simulations, we used a different equilibrium position $z_{\mathrm{eq}}=h$ for the extra particle than for the other particles that were confined at $z_{\mathrm{eq}}=0$.

The Langevin force $\mathbf{L}_i(t)$ is defined by $\langle\mathbf{L}_i(t)\rangle=0$ and $\langle\mathbf{L}_i(t+\tau)\mathbf{L}_j(t)\rangle=2\nu MT\delta_{ij}\delta(\tau)$, where T is the temperature of the heat bath, $\delta(t)$ the delta function, and δ_{ij} the Kronecker delta.

In a simulation run, $N-1$ particles are initially equilibrated. The x and y axes are oriented so that there is a line of nearest neighbors (and a channel) in the x direction, see Fig. 1(c). Then, at $t=0$, the extra particle is added to the crystal with an initial velocity $\mathbf{v}(t=0)=v_0\mathbf{e}_x$ in the x direction. The simulation is stopped before the extra particle reaches the boundary of the crystal.

The simulated crystal consisted of $N=10\,001$ particles, the particle mass $M=0.61\times10^{-12}$ kg, charge $Q=-18500e$ and screening length $\lambda=380$ μm was in the parameter range of the experimental observations of Refs. [5,6]. If not stated otherwise, the friction coefficient was $\nu=1.26$ s^{-1}, corresponding to a typical gas pressure of 1.0 Pa [35]. The wake charge q and distance δ are not known in experiments—in theory and simulations they are

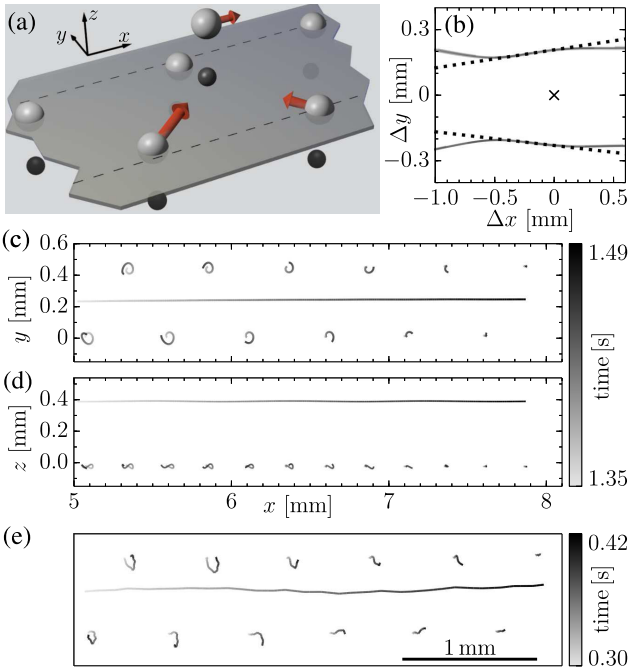

FIG. 1. Channeling of an extra particle in a simulated complex plasma crystal. (a) The particles are sketched in gray, their wake charges in black. The unperturbed channel is visualized by dashed lines on the semitransparent crystal plane. During the passage of the extra particle floating above the crystal from left to right, its wake attracts the channel particles (thick arrows shown for two particles). Because of the small displacement δy of the channel particles, the repulsive particle interaction is stronger behind the extra particle than in front of it, leading to a propulsion of the extra particle (thin arrow). (b) Horizontal particle positions with respect to the extra particle between $t_1=1.35$ and $t_2=1.49$ s. The position of the extra particle is indicated by a cross. The relative positions were fitted by straight dotted lines for -0.4 mm $<\Delta x<0$. (c) Horizontal (top view) particle positions color coded with respect to time between t_1 and t_2. (d) The same for the xz projection (side view); here, only the extra particle and the two neighboring rows that form the channel are shown. (e) Horizontal particle positions from experiment 5 of Ref. [5].

assumed to be a fraction < 1 of the particle charge and of the screening length, respectively [26,31,34]. Here, $q = 0.6|Q|$ and $\delta = 0.4\lambda$ was used. The parameters of the confinement were $\Omega_h = 2\pi \times 0.12\ \mathrm{s}^{-1}$, $\Omega_z = 2\pi \times 22\ \mathrm{s}^{-1}$, $h = 350\ \mu$m, and $R = 27$ mm.

Channeling effect.—The horizontal trajectory of the extra particle between $t_1 = 1.35$ and $t_2 = 1.49$ s can be seen in Fig. 1(c). The extra particle was added to the crystal at the position $\mathbf{r}_e(t = 0) = (-18, 0.21, 0.39\ \mathrm{mm})$ with an initial velocity $v_0 = 10$ mm/s. The particles were confined by the tenth-order potential V_i^t and formed a very regular lattice with an interparticle distance of $a = 504 \pm 3\ \mu$m. It can be seen that the particles forming the channel (the *channel* particles in the following) move towards the extra particle shortly after its passage. They subsequently perform a circular motion. Although a friction force is applied to the extra particle, it moves in a straight line at a constant velocity. The horizontal trajectories agree well with the experimental data shown in Fig. 1(e). In Fig. 1(d), it can be seen that the channel particles oscillate also in the vertical direction, while the extra particle moves at an almost constant height.

To visualize the deformation of the channel, the horizontal particle positions with respect to the extra particle, $\Delta\mathbf{r}_i = \mathbf{r}_i - \mathbf{r}_e$, are shown in Fig. 1(b). It can be seen that behind the extra particle the channel is clearly deformed, breaking the forward-backward symmetry of the channel geometry. The channel is shaped as a cone in the vicinity of the extra particle. In a range $-0.4\ \mathrm{mm} < \Delta x < 0$, the deformed channel is fitted to straight lines which have angles of 9.4° and −7.1° measured from the x axis.

The sketch shown in Fig. 1(a) gives a first idea of the propulsion mechanism: During the passage of the extra particle floating above the crystal, the channel particles are attracted to the wake charge of the extra particle and thus deform the channel. Because of this symmetry-breaking deformation, the repulsion between the channel particles and the extra particle is stronger behind the extra particle than in front of it, leading to a net propelling force acting on the extra particle.

The density variations in the crystal caused by the extra particle are shown in Fig. 2. The density in the reference frame of the extra particle was averaged over times $t_1 < t < t_2$. Pronounced subsonic lateral wakes behind the extra particle can be clearly seen. They form due to the dispersion of waves that are excited by the extra particle and propagate in the crystal [36]. The structure of the density variations is very similar to the experimental observation in Ref. [5]. Just behind the extra particle, in a region $-1\ \mathrm{mm} < \Delta x < 0$ and $|\Delta y| < 0.5$ mm, the density is substantially increased. Similar lateral wakes have been produced in experiment and simulation by sweeping an external perturbation through the crystal [37].

The extra-particle energy balance is depicted in Fig. 3(a). The potential energy of the particle, given by the mutual

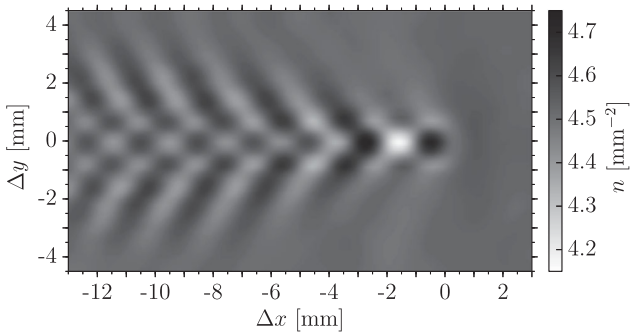

FIG. 2. Local particle density n in the reference frame of the extra particle, showing the pronounced wave structure behind the extra particle (lateral wake [36,37]).

particle interactions of Eq. (2) and the confinement $V_i^t + V_i^z$, does hardly change, it is only modulated by a slight vertical oscillation of the particle. The kinetic energy of the particle increases linearly in the first second of the channeling process, before saturating at an almost constant value.

In a different simulation, the crystal was confined by the parabolic horizontal confinement V_i^p. The extra particle was initially positioned near the center of the crystal with $v_0 = 10$ mm/s. The extra particle was confined in the channel which was slightly bent (see also Supplemental Material [38]). The energy balance is shown in Fig. 3(b). As the extra particle advances, it accumulates potential energy due to the parabolic confinement, but the propulsion effect is strong enough to accelerate the particle. Only near

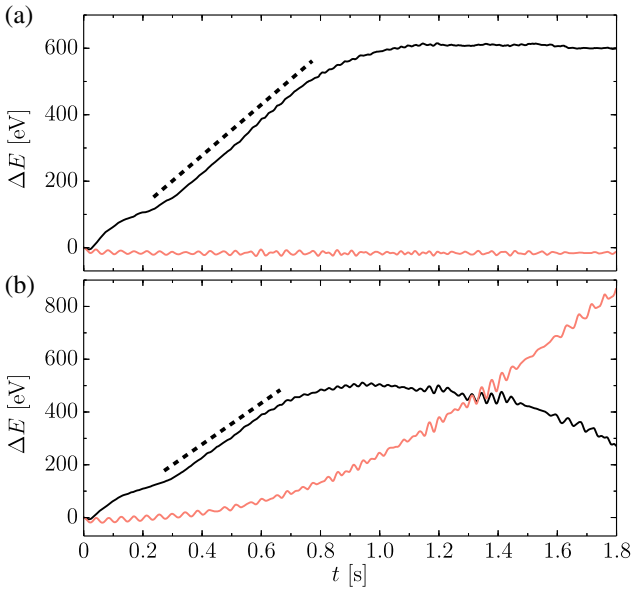

FIG. 3. (a) Variation of the kinetic energy (black) and the potential energy [red (gray)] of the extra particle as a function of time. The dashed line of slope 765 eV/s is to guide the eye. (b) The same for a crystal confined horizontally by a parabolic confinement. The dashed line has a slope of 781 eV/s.

the boundary of the crystal the velocity decreases as the confinement well becomes steeper.

Model for accelerated extra-particle motion.—In Fig. 4, the velocity of the extra particle v in a tenth-order horizontal confinement is shown as a function of time for five simulations with different initial velocities v_0 in the interval containing the longitudinal and transverse sound speeds $c_L = 23 \pm 1$ mm/s and $c_T = 6 \pm 1$ mm/s. In the cases where 10 mm/s $\leq v_0 \leq$ 25 mm/s, the extra particle is confined in the channel and its velocity saturates at $v_s = 20.5 \pm 0.3$ mm/s, where the propulsion effect is counterbalanced by friction. Note that v_s is also reached from above for particles with $v_0 > v_s$. In the simulation with $v_0 = 5$ mm/s (bold line in Fig. 4), the channel particles are displaced such that the repelling force exerted on the extra particle has a larger y component, leading to a less effective propulsion in the x direction. It also leads to a larger scattering angle in the channel, and as the extra particle accumulates enough kinetic energy it leaves the channel at $t \approx 1.4$ s. Upon exiting the channel, the extra particle is greatly accelerated such that it obtains a velocity $v > v_s$.

Below we establish a simple model for the propulsion mechanism in the channel. To estimate the small displacement δy of the channel particle, we assume the attraction to the wake of the extra particle $F_w(r_w)$ to be constant in the range $-a/2 < \Delta x < a/2$ and evaluate it at $\mathbf{r}_w = (a/2, b/2, h - \delta)$, i.e., when the particle distance in the x direction is half an interparticle distance [as sketched in Fig. 1(a)]. This yields $\delta y \approx F_w(r_w) b a^2/(4 r_w M v_s^2)$, where $b = (\sqrt{3}/2)a$ is the channel width. The net propelling force —stemming from the asymmetry of the repulsive particle interactions $F_p(r)$ before and after the passage—can then be estimated as $\Delta F \approx F_p(\tilde{r}) a/2\tilde{r} - F_p(r) a/2r$, where $\mathbf{r} = (a/2, b/2, h)$ and $\tilde{\mathbf{r}} = (a/2, b/2 - \delta y, h)$. For small δy we obtain $\Delta F \approx \delta y [(\partial/\partial \delta y) F_p(\tilde{r}) a/2\tilde{r}]_{\delta y = 0}$, and equating ΔF with the friction force, the terminal extra-particle velocity can be estimated as

$$v_{\text{theory}}^3 \approx \xi(r) \frac{F_p(r)}{r^3} \frac{F_w(r_w)}{r_w} \frac{b^2 a^3}{16 M^2 \nu}, \tag{3}$$

where $\xi(r) = (3 + 3r/\lambda + r^2/\lambda^2)/(1 + r/\lambda)$ depends rather weakly on r. For the simulation parameters, $v_{\text{theory}} = 23.9$ mm/s slightly overestimates the terminal extra-particle velocity. One reason for the discrepancy is that the particle-particle repulsion was not considered when estimating the wake-mediated displacement δy. A comparison of v_s and v_{theory} for different values of friction rate in the range 0.32 s^{-1} $< \nu <$ 2.21 s^{-1} can be seen in the inset of Fig. 4. The model always slightly overestimates the extra-particle velocity, but the predicted scaling $v_s \propto \nu^{-1/3}$ is in good agreement with simulations.

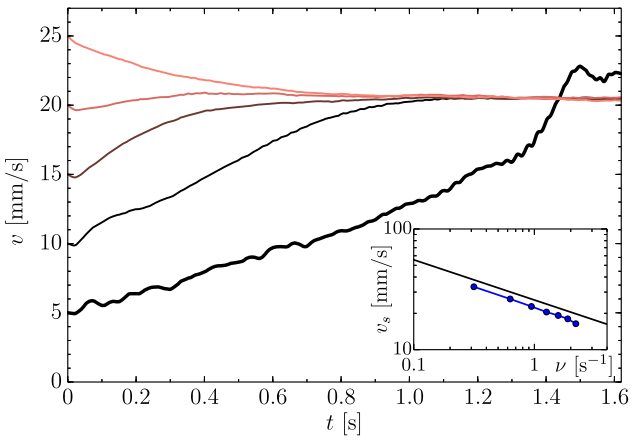

FIG. 4. Magnitude of the extra-particle velocity as a function of time, for different initial velocities v_0. The extra particle with $v_0 = 5$ mm/s (bold line) exits the channel at $t \approx 1.4$ s while the others stay in the same channel and reach a constant velocity v_s. The inset shows v_s as a function of damping rate ν. The error is no larger than the symbol size. The predicted value of Eq. (3) is shown as a black line.

Discussion.—It is expected that the extra particle floats above the crystal because it has a slightly smaller mass than the other particles [39]. Varying the mass (and charge) of the extra particle may yield further conclusions regarding the mass ratios in experiments. In order to fully understand the origin of the extra particles floating above or below the crystal layer, a more realistic particle confinement is needed that explicitly considers the balance of electric and gravitational forces in the vertical direction. The ion wake of the extra particle will be dynamically distorted when it is very close to a channel particle. The pointlike model may thus not be applicable in narrow channels (when a is very small) or during head-on collisions with a channel particle.

In Ref. [40], a particle-in-cell simulation was used to model the particle interactions in a crystal with an extra particle below the crystal plane. The propelled motion of this *downstream* particle was reproduced in MD simulations, but no intuitive picture was given for the mechanism. Here, with the aid of the pointlike wake charge model, this intuitive explanation was given for the persistent motion of an upstream particle. The propulsion mechanism based on the nonreciprocal particle interactions controls the terminal extra-particle velocity and enables the study of self-propelled motion in complex plasmas [41].

Reproducing the channeling effect in simulations also enables the study of the wave processes that are discussed in the Supplemental Material [42].

Equation (3) closely reproduces the extra-particle velocity v_s measured in experiments. Assuming the wake parameters to be $q/|Q| = 0.6$ and $\delta/\lambda = 0.4$ as in our simulations, we obtain $v_s/v_{\text{theory}} = 0.85$, 0.85, and 0.82 for experiments 1, 3, and 5 of Ref. [5], respectively (see Table 1 in Ref. [5]). Again, the predicted velocity is slightly above the observed value. In simulations, channeling was observed if the initial velocity v_0 was above the transverse sound speed c_T.

To conclude, we reproduced in MD simulations the propulsion of an extra particle in a 2D plasma crystal with the intuitive model of a pointlike ion wake charge. The nonreciprocal particle interactions, owing to the ion wake, lead to an asymmetric deformation of the channel and a net propelling force. The terminal velocity reached by the extra particle agrees well with our theoretical considerations and with experiments.

We thank Cheng-Ran Du for providing the experimental data. This work was supported by the German Federal Ministry for Economy and Technology under Grant No. 50WM1441. G. E. M. wishes to acknowledge support from RSF Grant No. 14-43-00053.

*Ingo.Laut@dlr.de

[1] D. S. Gemmell, Rev. Mod. Phys. **46**, 129 (1974).
[2] L. C. Feldman, J. W. Mayer, and S. T. A. Picraux, *Materials Analysis by Ion Channeling: Submicron Crystallography* (Academic, New York, 2012).
[3] C. Salomon, J. Dalibard, A. Aspect, H. Metcalf, and C. Cohen-Tannoudji, Phys. Rev. Lett. **59**, 1659 (1987).
[4] C. Keller, J. Schmiedmayer, A. Zeilinger, T. Nonn, S. Dürr, and G. Rempe, Appl. Phys. B **69**, 303 (1999).
[5] C.-R. Du, V. Nosenko, S. Zhdanov, H. M. Thomas, and G. E. Morfill, Europhys. Lett. **99**, 55001 (2012).
[6] C.-R. Du, V. Nosenko, S. Zhdanov, H. M. Thomas, and G. E. Morfill, Phys. Rev. E **89**, 021101(R) (2014).
[7] S. Zhdanov, C.-R. Du, M. Schwabe, V. Nosenko, H. M. Thomas, and G. E. Morfill, Europhys. Lett. **114**, 55002 (2016).
[8] J. Deseigne, O. Dauchot, and H. Chaté, Phys. Rev. Lett. **105**, 098001 (2010).
[9] V. Schaller, C. Weber, C. Semmrich, E. Frey, and A. R. Bausch, Nature (London) **467**, 73 (2010).
[10] I. Buttinoni, J. Bialké, F. Kümmel, H. Löwen, C. Bechinger, and T. Speck, Phys. Rev. Lett. **110**, 238301 (2013).
[11] J. H. Chu and L. I, Phys. Rev. Lett. **72**, 4009 (1994); H. Thomas, G. E. Morfill, V. Demmel, J. Goree, B. Feuerbacher, and D. Möhlmann, Phys. Rev. Lett. **73**, 652 (1994); Y. Hayashi and K. Tachibana, Jpn. J. Appl. Phys. **33**, L804 (1994).
[12] G. E. Morfill and A. V. Ivlev, Rev. Mod. Phys. **81**, 1353 (2009).
[13] A. Piel, M. Klindworth, O. Arp, A. Melzer, and M. Wolter, Phys. Rev. Lett. **97**, 205009 (2006).
[14] H. M. Thomas, G. E. Morfill, V. E. Fortov, A. V. Ivlev, V. I. Molotkov, A. M. Lipaev, T. Hagl, H. Rothermel, S. A. Khrapak, R. K. Suetterlin, M. Rubin-Zuzic, O. F. Petrov, V. I. Tokarev, and S. K. Krikalev, New J. Phys. **10**, 033036 (2008).
[15] V. A. Schweigert, I. V. Schweigert, A. Melzer, A. Homann, and A. Piel, Phys. Rev. Lett. **80**, 5345 (1998).
[16] C. Killer, T. Bockwoldt, S. Schütt, M. Himpel, A. Melzer, and A. Piel, Phys. Rev. Lett. **116**, 115002 (2016).
[17] S. Nunomura, S. Zhdanov, D. Samsonov, and G. Morfill, Phys. Rev. Lett. **94**, 045001 (2005).
[18] Y.-Y. Tsai, J.-Y. Tsai, and L. I, Nat. Phys. **12**, 573 (2016).
[19] K. O. Menzel, O. Arp, and A. Piel, Phys. Rev. Lett. **104**, 235002 (2010).
[20] J. D. Williams, Phys. Rev. E **90**, 043103 (2014).
[21] H. Ikezi, Phys. Fluids **29**, 1764 (1986).
[22] A. Melzer, V. A. Schweigert, and A. Piel, Phys. Rev. Lett. **83**, 3194 (1999).
[23] J. Kong, T. W. Hyde, L. Matthews, K. Qiao, Z. Zhang, and A. Douglass, Phys. Rev. E **84**, 016411 (2011).
[24] L. Couëdel, S. K. Zhdanov, A. V. Ivlev, V. Nosenko, H. M. Thomas, and G. E. Morfill, Phys. Plasmas **18**, 083707 (2011).
[25] A. V. Ivlev, J. Bartnick, M. Heinen, C.-R. Du, V. Nosenko, and H. Löwen, Phys. Rev. X **5**, 011035 (2015).
[26] A. V. Ivlev and G. Morfill, Phys. Rev. E **63**, 016409 (2000).
[27] T. B. Röcker, A. V. Ivlev, S. K. Zhdanov, L. Couëdel, and G. E. Morfill, Phys. Plasmas **21**, 073711 (2014).
[28] H. Totsuji, C. Totsuji, and K. Tsuruta, Phys. Rev. E **64**, 066402 (2001).
[29] A. V. Ivlev, U. Konopka, G. E. Morfill, and G. Joyce, Phys. Rev. E **68**, 026405 (2003).
[30] T. E. Sheridan, Phys. Plasmas **15**, 103702 (2008).
[31] I. Laut, S. K. Zhdanov, C. Räth, H. M. Thomas, and G. E. Morfill, Phys. Rev. E **93**, 013204 (2016).
[32] C. Durniak, D. Samsonov, N. P. Oxtoby, J. F. Ralph, and S. Zhdanov, IEEE Trans. Plasma Sci. **38**, 2412 (2010).
[33] S. Zhdanov, R. A. Quinn, D. Samsonov, and G. E. Morfill, New J. Phys. **5**, 74 (2003).
[34] T. B. Röcker, L. Couëdel, S. K. Zhdanov, V. Nosenko, A. V. Ivlev, H. M. Thomas, and G. E. Morfill, Europhys. Lett. **106**, 45001 (2014).
[35] B. Liu, J. Goree, V. Nosenko, and L. Boufendi, Phys. Plasmas **10**, 9 (2003).
[36] D. H. E. Dubin, Phys. Plasmas **7**, 3895 (2000).
[37] V. Nosenko, J. Goree, Z. W. Ma, D. H. E. Dubin, and A. Piel, Phys. Rev. E **68**, 056409 (2003).
[38] See Supplemental Material at http://link.aps.org/supplemental/10.1103/PhysRevLett.118.075002 for a movie of an extra particle in a crystal with parabolic confinement.
[39] S. Zhdanov, L. Couëdel, V. Nosenko, H. M. Thomas, and G. E. Morfill, Phys. Plasmas **22**, 053703 (2015).
[40] V. A. Schweigert, I. V. Schweigert, V. Nosenko, and J. Goree, Phys. Plasmas **9**, 4465 (2002).
[41] R. Bechinger, R. Di Leonardo, H. Löwen, C. Reichhardt, G. Volpe, and G. Volpe, Rev. Mod. Phys. **88**, 045006 (2016).
[42] See Supplemental Material at http://link.aps.org/supplemental/10.1103/PhysRevLett.118.075002, which includes Refs. [43–47], for a detailed analysis of the wave processes.
[43] Z. Donkó, G. J. Kalman, and P. Hartmann, J. Phys. Condens. Matter **20**, 413101 (2008).
[44] L. Couëdel, V. Nosenko, S. K. Zhdanov, A. V. Ivlev, H. M. Thomas, and G. E. Morfill, Phys. Rev. Lett. **103**, 215001 (2009).
[45] S. Nunomura, S. Zhdanov, G. E. Morfill, and J. Goree, Phys. Rev. E **68**, 026407 (2003).
[46] L. Couëdel, V. Nosenko, A. V. Ivlev, S. K. Zhdanov, H. M. Thomas, and G. E. Morfill, Phys. Rev. Lett. **104**, 195001 (2010).
[47] L. Couëdel, T. B. Röcker, S. K. Zhdanov, V. Nosenko, H. M. Thomas, and A. V. Ivlev, Europhys. Lett. **115**, 45002 (2016).

Time series with tailored nonlinearities (Ref. [126])

C. Räth and I. Laut. *Time series with tailored nonlinearities*, Physical Review E **92**, 040902(R) (2015) http://dx.doi.org/10.1103/PhysRevE.92.040902
©2015 American Physical Society

PHYSICAL REVIEW E **92**, 040902(R) (2015)

Time series with tailored nonlinearities

C. Räth* and I. Laut

Deutsches Zentrum für Luft- und Raumfahrt, Forschungsgruppe Komplexe Plasmen, Münchner Straße 20, 82234 Weßling, Germany

(Received 11 November 2014; revised manuscript received 27 August 2015; published 8 October 2015)

It is demonstrated how to generate time series with tailored nonlinearities by inducing well-defined constraints on the Fourier phases. Correlations between the phase information of adjacent phases and (static and dynamic) measures of nonlinearities are established and their origin is explained. By applying a set of simple constraints on the phases of an originally linear and uncorrelated Gaussian time series, the observed scaling behavior of the intensity distribution of empirical time series can be reproduced. The power law character of the intensity distributions being typical for, e.g., turbulence and financial data can thus be explained in terms of phase correlations.

DOI: 10.1103/PhysRevE.92.040902 PACS number(s): 05.45.Tp, 89.65.Gh, 95.75.Wx

Introduction. The clearest yet most general definition of nonlinearity in time series $g(t)$ is given in the Fourier representation

$$G(k) = \mathrm{FT}[g(t)] = \frac{1}{N}\sum_{t=0}^{N-1} g(t)e^{-i2\pi kt/N} \qquad (1)$$

of the data. Linear time series are fully characterized by the modulus $|G(k)|$ of the complex valued Fourier coefficients $G(k) = |G(k)|e^{i\phi(k)}$, while the phases $\phi(k)$ are uncorrelated and uniformly distributed in the interval $\phi \in [-\pi;\pi]$. *Any* nonlinearity is coded in the Fourier phases $\phi(k)$ and correlations among them. Deviation from the randomness of the phases is thus equivalent to the presence of nonlinearities in the time series. As yet, only little attention has been paid so far to the explicit analysis of the information contained in the Fourier phases to characterize nonlinearities, although a lot of insights about nonlinearities may be gained by better understanding the meaning of phases.

The definition of nonlinearity via the randomness of Fourier phases is,- on the other hand, at the heart of algorithms for generating so-called surrogate data sets, which were developed to test for weak nonlinearities in a model-independent way [1]. These surrogates are supposed to have the same linear properties as a given data set, while all nonlinearities are wiped out. The removal of the nonlinear correlations is achieved by replacing the phases $\phi(k)$ with a set of uncorrelated and uniformly distributed ones. Refinements of the Fourier-based methods for generating surrogates aimed at preserving both the power spectrum $|G(k)|^2$ and the amplitude distribution of the time series $g(t)$ in real space [1–4]. The addition of (iterative) rank-ordered remapping of the phase randomized data onto the original amplitude distribution led to surrogates with the desired amplitude spectrum [1,2]. Applying the iterated amplitude adjusted Fourier transform (IAAFT) method in the wavelet domain allowed for the generation of surrogates which also preserve the local mean and variance of the original signal [3,4].

However, it was found recently that these (iterated) amplitude adjusted [(I)AAFT] surrogates may not be linear, since the randomness of the phases is guaranteed only before the first remapping step. One can rather find phase correlations in surrogate realizations that may result in a nondetection of nonlinearities in time series [5]. But this obvious flaw of (I)AAFT surrogates became a virtue as significant correlations between phase statistics and a measure for nonlinearity were found for the first time (see [5] and insets in Fig. 2).

Connections between correlations among Fourier phases and higher order statistics could also be identified by analyzing the cosmic microwave background radiation (CMB). Several studies of both the WMAP and PLANCK data involving surrogates revealed that there are phase correlations at large scales in the CMB which lead to pronounced anisotropies (see, e.g., [6–8]). Recently it was demonstrated that the observed phase correlations can gradually be diminished when subtracting suitable best-fit (Bianchi-)template maps. The weaker phase correlations lead in turn to a vanishing signature of anisotropy as identified with higher order statistics [9]. The relations between phase information and higher order statistics in (I)AAFT surrogates and the CMB data were only found in a heuristic manner.

To allow for a systematic investigation of phase correlations and their corresponding nonlinearities in time series, it is desirable to start with the phases, constrain their correlations in a tunable and reproducible way, and study the effects on the nonlinear statistics.

Here, we present a method to generate time series with such tailored nonlinearities by imposing well-defined correlations on the Fourier phases and demonstrate how deviations from linearity can be understood in terms of phase information.

Methods. To address the relationship between phase correlations and measures for nonlinearity we calculate the nonlinear prediction error (NLPE) [10] as an example for a dynamical complexity measure with a good overall performance [11] and the average connectivity of (recurrence) networks as an example for a structural complexity measure [12,13]. The calculation of both measures relies on the representation of the time series in an artificial phase space, which is obtained using the method of delay coordinates [14]. This is accomplished by using time delayed versions of the observed time series as coordinates for the embedding space. The multivariate vectors in the d-dimensional space are expressed by $\vec{g}_t = (g_t, g_{t+\tau}, g_{t+2\tau}, \ldots, g_{t+(d-1)\tau})$, where τ is the delay time and g_t denotes the value of the (discretized) time series at time step t.

The comparison of the predicted behavior of the embedded time series based on the local neighbors with the real trajectory

*Corresponding author: christoph.raeth@dlr.de

 ©2015 American Physical Society

of the system leads to the definition of the NLPE ψ as

$$\psi = \psi(d,\tau,T,N) = \frac{1}{[M-T-(d-1)\tau]}\sqrt{\sum_{n=(d-1)\tau}^{M-1-T}[\vec{g}_{t+T}-F(\vec{g}_t)]^2}, \quad (2)$$

where F is a locally constant predictor, M is the length of the time series, and T is the lead time. The predictor F is calculated by averaging over future values of the $N = d+1$ nearest neighbors in the delay coordinate representation. We found that ψ remains rather constant for $T > 5$, thus a value of $T = 5$ was used for this study. The dimension of the embedding space d and the delay time τ have to be set appropriately. Since the time series of an active galactic nuclei (AGN) being studied in the following consists of less than 1600 data points, we use a low embedding dimension $d = 3$. Due to the long correlation time of this time series, we chose a relatively large delay time $\tau = 250$ according to the criterion of zero crossing of the autocorrelation function [15]. To allow for a direct comparison, we use the same values $d = 3$ and $\tau = 250$ for the other time series with imposed phase correlations. The structural complexity of a time series with a limited number of points can be characterized with recurrence networks [16]. They are based on recurrence plots [17], which describe how often pairs of points of a time series in the embedding space representation come close to each other. Linking such nearby points in a network representation of the data and omitting self-loops leads to the definition of the adjacency matrix $A_{i,j}$ of the recurrence network [12]

$$A_{i,j} = \Theta(\epsilon - \|\mathbf{g}_i - \mathbf{g}_j\|) - \delta_{i,j}, \quad (3)$$

where the $\{\mathbf{g}_n\}$ are the data points in embedding space and ϵ is an appropriate threshold. $A_{i,j}$ contains the whole information about the network. A common measure for the topological structure of the network is the average connectivity κ which is calculated by

$$\kappa = \frac{1}{n(n-1)}\sum_{v=0}^{n-1} k_v, \quad (4)$$

where $k_v = \sum_{i=0}^{n-1} A_{v,i}$ is the degree of node v. If the attractor of the nonlinear system is reconstructed with appropriate embedding parameters this network measure can be used as a test for nonlinearity. The threshold ϵ is chosen such that $\kappa = 0.01$ for the original time series. The same threshold is then used for the Gaussian time series with imposed phase correlations.

To get a visual impression of correlations among the Fourier phases it is convenient to make use of so-called phase maps [18]. A phase map is defined as a two-dimensional set of points $G = \{\phi_k, \phi_{k+\Delta}\}$ where ϕ_k is the phase of the kth mode of the Fourier transform and Δ a frequency delay. To quantify the degree of correlation between the phases ϕ and $\phi + \Delta$ we calculate the correlation coefficient $c(\Delta)$,

$$c(\Delta) = \frac{\langle\phi(k)\phi(k+\Delta)\rangle}{\sigma_{\phi(k)}\sigma_{\phi(k+\Delta)}}. \quad (5)$$

Note that by using $c(\Delta)$ as correlation measure we restrict ourselves to the simplest way of quantifying correlations among the phases that is only sensitive to linear correlations.

Time series with phase correlations. As outlined in [7], (I)AAFT surrogates can contain phase correlations leading to statistically significant high or low values of $c(\Delta)$. A closer look at the corresponding phase maps reveals that the (anti-)correlations originated from stripelike patterns along the diagonal (i.e., with slope of one) or shifted relative to it. These patterns thus indicate that phase pairs are linearly correlated with each other. One can further notice that for the time series stemming from x-ray observations of the AGN Mrk 766 the phase correlations are most pronounced for $\Delta = 1$. We reproduce such signatures by imposing correlations in the phase distribution in the following way: The values for the phases $\phi(k)$ are iteratively determined by relating $\phi(k+\Delta)$ with $\phi(k)$ by

$$\phi(k+\Delta) = \phi(k) + d\phi + \eta \quad (6)$$

with $d\phi$ being a shift constant ranging from $-\pi$ to π and η describing a (Gaussian) noise term with given standard deviation σ_η. In the phase map picture η controls the width of the stripes and $d\phi$ defines its position. The iteration is performed over the frequencies k, where k_s denotes the starting value and dk the step size of the iteration. $\phi(k_s)$ is drawn from a uniform distribution within the interval $[-\pi,\pi]$. The same is true for $\phi(k)$ if this phase has not been set in a previous iteration step. In our first example we are interested in only correlating adjacent phases. Thus we apply Eq. (6) with $\Delta = 1$ to a Gaussian time series with zero mean and standard deviation of one. The step size is chosen to be $dk = 2$. Thereby every phase is correlated to exactly one other phase for $\Delta = 1$, while the phases are not correlated for any frequency delay Δ greater than 1.

Figure 1 shows how these phase correlations alter the time series. It becomes clearly visible that the correlations of adjacent phases induce fluctuations of the variance. Specifically, one recognizes a time interval where the fluctuations are larger than for the noise and another region where the fluctuations are smaller. Note that the overall mean and standard deviation of the time series are exactly preserved since the power spectrum is kept constant. The shift constant controls the position of

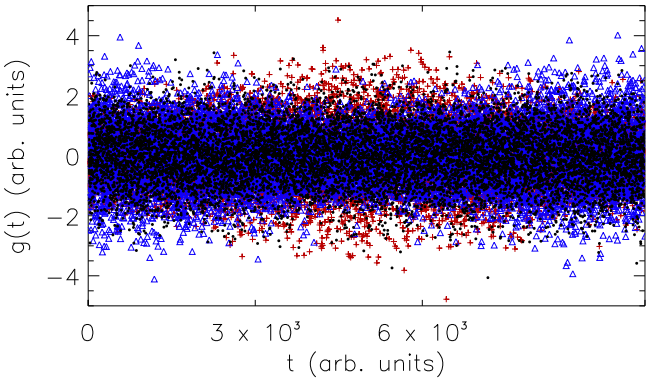

FIG. 1. (Color online) Gaussian random uncorrelated noise (black, filled circles). The colored points show time series with linear phase correlations among adjacent phases ($\Delta = 1$) with $\sigma_\eta = 1.0$ and $d\phi = 0$ (blue, triangles) and $d\phi = \pi$ (red, crosses).

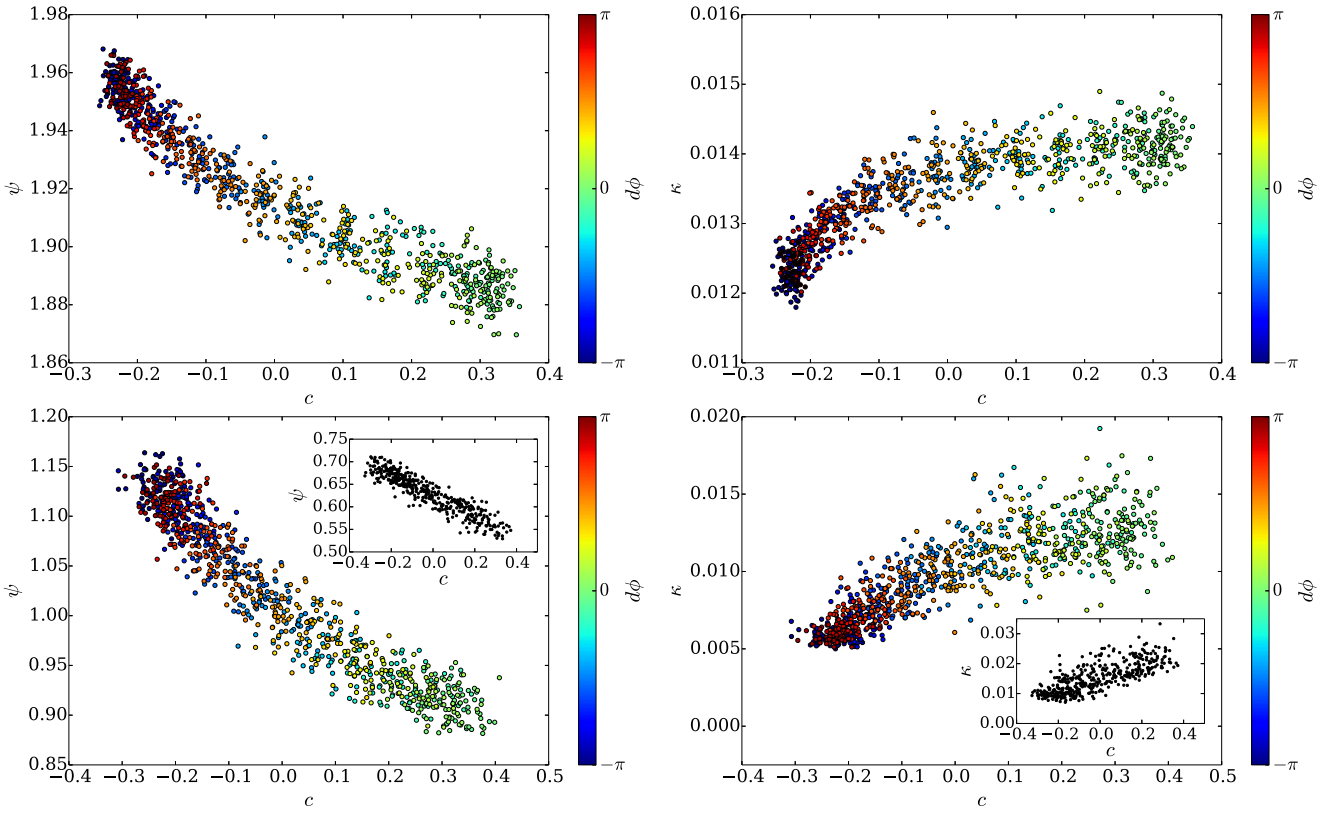

FIG. 2. (Color online) Upper row: Nonlinear prediction error ψ (upper left) and average connectivity κ (upper right) versus phase correlation coefficient $c(\Delta = 1)$ for 900 time series with imposed phase correlations derived from Gaussian noise as input time series $g(t)$. Lower row: Same as upper row but with the Mrk 766 x-ray observation as input time series $g(t)$. The data from revolution 999 was binned with a bin size of 50 s leading to a time series with 1540 points. The insets show the corresponding results for 400 IAAFT surrogates.

the region with higher fluctuations. If $d\phi = \pm\pi$, this region is located in the middle of the time series and it shifts towards the ends of the time series when $d\phi$ approaches 0. By testing different values of Δ we further found that the number of regions with high fluctuations is given by the value for Δ. In Fig. 2 we show the nonlinear prediction error ψ and the mean connectivity κ as a function of the correlation coefficient $c(\Delta = 1)$. The results are displayed for time series with imposed phase correlations (only) for $\Delta = 1$ and varying $d\phi$ as derived from Gaussian noise and from the x-ray observation of the AGN Mrk 766. One can see that the shift constant $d\phi$ controls the (anti-)correlations of the phases. More importantly, it becomes obvious that both the nonlinear prediction error and the mean connectivity are highly (anti-)correlated with the phase correlations as measured with $c(\Delta)$. Knowing that $d\phi$ also controls the position of the regions with higher and lower fluctuations, we can now get a much more detailed understanding of how the phase correlations influence the calculation of the NLPE and the average connectivity. The embedding with the delay time of $\tau = 250$ in three dimensions leads to a truncation of the last part of the time series. Depending on whether the remaining time series has larger ($d\phi \approx \pm\pi$) or lower ($d\phi \approx 0$) fluctuations, one obtains larger or lower values for the NLPE leading to the observed anticorrelation between ψ and c. Similarly, lower fluctuations in the time series lead to a more connected recurrence network and vice versa, correlating κ and $c(\Delta)$.

In a second example we extend the formalism to generate nonlinear time series with well-defined nonlinearities by simultaneously imposing linear phase correlations for a set of different frequency delays Δ. This is achieved by iteratively applying Eq. (6) starting with low values of Δ and then proceeding to higher ones. Iterating over increasing frequency delays Δ ensures that phase correlations that were imposed in previous iteration steps are at least in part preserved when new constraints for phase correlations at larger Δ are added. Table I summarizes the parameters for the six iterations used in our example. Figure 3 shows the time series which is obtained when the six constraints on phase correlations are

TABLE I. Parameters defining the imposed phase correlations.

	Δ	dk	k_s	$d\phi$	σ_η
1. Iteration	1	2	1	3.1415	0.1
2. Iteration	3	3	1	3.0	0.08
3. Iteration	3	3	2	3.0	0.3
4. Iteration	5	5	2	1.4	0.2
5. Iteration	7	7	3	3.1415	0.25
6. Iteration	50	50	2	3.0	0.1

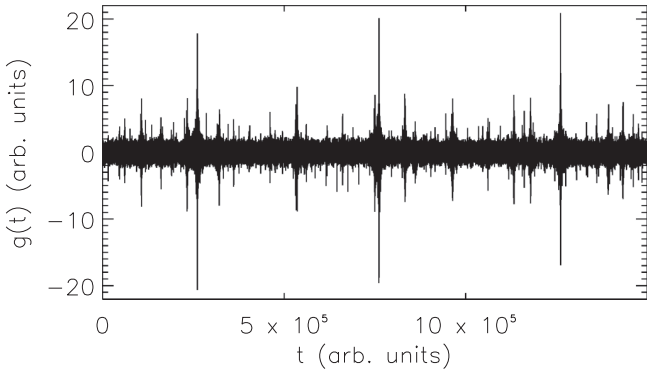

FIG. 3. Time series $g(t)$ that is obtained from white Gaussian noise by imposing a set of six different linear phase correlations.

imposed on white Gaussian noise. One has to note that the time series has no linear correlation as the modulus $|G(k)|$ of the Fourier transform of the original random time series is left untouched. In the time series with phase correlations one can clearly identify a number of time intervals with larger fluctuations whose number, position, and strength are controlled by the parameters Δ, dk, and η, respectively. The statistical properties of such a nonlinear time series can thus be tailored in a refined manner. The time series in this example was generated such that it resembles data often observed in economic time series [19], where especially data from stock indices show intermittent behavior, i.e., extreme events, patterns of volatility clustering and phase correlations, while the autocorrelation vanishes. The distribution of the fluctuations is further analyzed by calculating the cumulative probability distribution $P(g)$ of the normalized positive and negative values of $g(t)$ (see Fig. 4). We find the expected leptokurtic distribution whose tail can be fitted with a power law $P(g) \sim g^{-\alpha}$ with $\alpha = 3.25 \pm 0.16$ for the positive tail and $\alpha = 3.37 \pm 0.47$ for the negative tail in the region $5 \leqslant g \leqslant 20$. These numbers are in remarkable agreement with

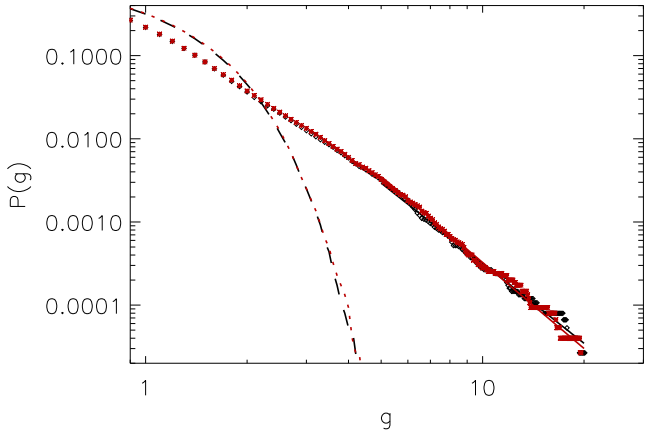

FIG. 4. (Color online) Cumulative probability distribution $P(g)$ of the normalized positive (black) and negative [red (gray)] values of $g(t)$. The black dashed and red (gray) dotted lines show the respective distributions for the initial white Gaussian noise.

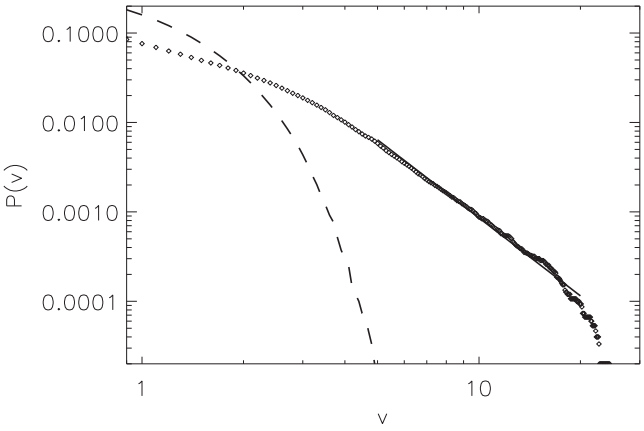

FIG. 5. Cumulative probability distribution $P(v)$ of the normalized volatility v. The black dashed line shows the respective distributions for the initial white Gaussian noise.

those obtained from empirical studies of market indices [20]. We further studied the statistical properties of the volatility $v(t)$ as defined as the average of $|g(t)|$ over a time window of length N, i.e., $v(t) = 1/N \sum_{t'=t}^{t+N-1} |g(t')|$. Figure 5 shows the cumulative probability distribution $P(v)$ for $N = 5$. As expected we find a distribution with fat tails, which can be fitted by $P(v) \sim v^{-\beta}$ with $\beta = 2.93 \pm 0.49$ in the region $5 \leqslant v \leqslant 20$. Again, this is in very good agreement with the scaling properties of the volatility of price fluctuations observed in empirical data [21].

Finally, we note that analogies between price dynamics of market indices and the velocity differences in three-dimensional fully developed turbulence have been pointed out by several authors (see, e.g., [22,23]). Consequently, the fat tails in the probability density functions of turbulence data may also be understood in terms of phase correlations allowing for a better characterization and discrimination of different scenarios of turbulence.

Summary. We have presented a method to generate time series with well-defined nonlinearities by imposing linear correlations among the Fourier phases. We have shown that the phase correlations between adjacent phases are tightly related with higher order statistics being estimated for the time series. These "Wiener-Khinchin-like" connections between phase information and higher order statistics are to a large extent independent of the input time series. Furthermore, the scaling of fluctuation and of the volatility of a time series can be understood in terms of a set of linear phase correlations. We expect that further studies with time series and also spatial structures with tailored nonlinearities, for which not only linear but more complex constraints on the Fourier phases are imposed, will shed more light on both the meaning of Fourier phases and the different kinds of nonlinearities as they are observed in nature.

Acknowledgments. This work has made use of observations obtained with XMM-Newton, an ESA science mission with instruments and contributions directly funded by ESA member states and the U.S. (NASA).

[1] J. Theiler, S. Eubank, A. Longtin, B. Galdrikian, and J. D. Farmer, Physica D **58**, 77 (1992).
[2] T. Schreiber and A. Schmitz, Phys. Rev. Lett. **77**, 635 (1996).
[3] C. J. Keylock, Phys. Rev. E **73**, 036707 (2006).
[4] C. J. Keylock, Nonlinear Processes Geophys. **17**, 615 (2010).
[5] C. Räth, M. Gliozzi, I. E. Papadakis, and W. Brinkmann, Phys. Rev. Lett. **109**, 144101 (2012).
[6] C. Räth, G. E. Morfill, G. Rossmanith, A. J. Banday, and K. M. Górski, Phys. Rev. Lett. **102**, 131301 (2009).
[7] C. Räth, A. J. Banday, G. Rossmanith, H. Modest, R. Sütterlin, K. M. Górski, J. Delabrouille, and G. E. Morfill, Mon. Not. R. Astron. Soc. **415**, 2205 (2011).
[8] Planck Collaboration, P. A. R. Ade, N. Aghanim, C. Armitage-Caplan, M. Arnaud, M. Ashdown, F. Atrio-Barandela, J. Aumont, C. Baccigalupi, A. J. Banday *et al.*, Astron. Astrophys. **571**, A23 (2014).
[9] H. I. Modest, C. Räth, A. J. Banday, K. M. Górski, and G. E. Morfill, Phys. Rev. D **89**, 123004 (2014).
[10] G. Sugihara and R. M. May, Nature (London) **344**, 734 (1990).
[11] T. Schreiber and A. Schmitz, Phys. Rev. E **55**, 5443 (1997).
[12] R. V. Donner, Y. Zou, J. F. Donges, N. Marwan, and J. Kurths, New J. Phys. **12**, 033025 (2010).
[13] I. Laut, C. Räth, L. Wörner, V. Nosenko, S. K. Zhdanov, J. Schablinski, D. Block, H. M. Thomas, and G. E. Morfill, Phys. Rev. E **89**, 023104 (2014).
[14] N. H. Packard, J. P. Crutchfield, J. D. Farmer, and R. S. Shaw, Phys. Rev. Lett. **45**, 712 (1980).
[15] A. M. Fraser and H. L. Swinney, Phys. Rev. A **33**, 1134 (1986).
[16] N. Marwan, J. F. Donges, Y. Zou, R. V. Donner, and J. Kurths, Phys. Lett. A **373**, 4246 (2009).
[17] J.-P. Eckmann, S. Oliffson Kamphorst, and D. Ruelle, Europhys. Lett. **4**, 973 (1987).
[18] L.-Y. Chiang, P. Coles, and P. Naselsky, Mon. Not. R. Astron. Soc. **337**, 488 (2002).
[19] R. N. Mantegna and H. E. Stanley, *Introduction to Econophysics* (Cambridge University Press, Cambridge, UK, 2007).
[20] P. Gopikrishnan, V. Plerou, L. A. Nunes Amaral, M. Meyer, and H. E. Stanley, Phys. Rev. E **60**, 5305 (1999).
[21] Y. Liu, P. Gopikrishnan, P. Cizeau, M. Meyer, C.-K. Peng, and H. E. Stanley, Phys. Rev. E **60**, 1390 (1999).
[22] S. Ghashghaie, W. Breymann, J. Peinke, P. Talkner, and Y. Dodge, Nature (London) **381**, 767 (1996).
[23] R. N. Mantegna and H. E. Stanley, Phys. A (Amsterdam, Neth.) **239**, 255 (1997).

Surrogate-assisted network analysis of nonlinear time series (Ref. [127])

I. Laut and C. Räth. *Surrogate-assisted network analysis of nonlinear time series*, Chaos **26** 103108 (2016) http://dx.doi.org/10.1063/1.4964646
©2016 AIP Publishing

Surrogate-assisted network analysis of nonlinear time series

Ingo Laut[a] and Christoph Räth[b]
Deutsches Zentrum für Luft- und Raumfahrt, Forschungsgruppe Komplexe Plasmen, 82234 Weßling, Germany

(Received 13 June 2016; accepted 28 September 2016; published online 18 October 2016)

The performance of recurrence networks and symbolic networks to detect weak nonlinearities in time series is compared to the nonlinear prediction error. For the synthetic data of the Lorenz system, the network measures show a comparable performance. In the case of relatively short and noisy real-world data from active galactic nuclei, the nonlinear prediction error yields more robust results than the network measures. The tests are based on surrogate data sets. The correlations in the Fourier phases of data sets from some surrogate generating algorithms are also examined. The phase correlations are shown to have an impact on the performance of the tests for nonlinearity. *Published by AIP Publishing.* [http://dx.doi.org/10.1063/1.4964646]

Networks generated from time series have recently attracted much attention as they provide additional information about the data under consideration. Various different ways of creating such a network from a time series have been proposed. In this paper, we use recurrence and symbolic networks to detect weak nonlinearities. The performance of these network measures is compared to the well-known nonlinear prediction error (NLPE). Since often only a limited amount of data is available, we focus on relatively short time series with a few thousand time steps. We find that while all methods perform equally well for the synthetic data of the Lorenz system, the nonlinear prediction error yields the most robust results for real-world data from active galactic nuclei. The measurements are based on *surrogates* which are ersatz data that contain no nonlinearities. Analyzing different surrogate generating algorithms, we find correlations in the Fourier phases of some classes of surrogates which reveal the existence of induced nonlinearities in the supposedly pure linear data sets. We show that these nonlinearities are responsible for the weak performance of the surrogates in question.

I. INTRODUCTION

A recent milestone in the field of statistical physics has been the complex network theory.[1] The constituents of complex systems are translated into the nodes of a network, and their interactions are represented as edges. The network then contains extensive information about the system. While this procedure is straightforward for systems like social or neural networks, there is no "natural" way of how to create a network from a time series.

Nonlinear time series analysis[2,3] deals with the question whether a time series has underlying chaotic dynamics. To this end, some measure of nonlinearity, most of which are derived from chaos theory, is calculated for the time series. In order to make a significant statement, the measure may also be applied to a set of so-called surrogate data sets which mimic the linear properties of the original data.[4] As it is impossible to perfectly reproduce both the autocorrelation function as well as amplitude distribution, the available surrogate generation algorithms focus on different aspects.[4–6]

One method of creating a network from a time series is the *recurrence network*[7–9] motivated from recurrence quantification analysis (RQA).[10] In RQA, the time series is embedded in an artificial phase space. The recurrence matrix then contains the information which points are sufficiently close to each other in phase space. The structural properties of the recurrence matrix can be used to characterize different dynamic aspects of the time series.[10] By interpreting the recurrence matrix as an adjacency matrix, a network can be constructed from the time series. This approach may be used to characterize the underlying dynamical system[9] or detect dynamic changes by a sliding-window technique.[8]

Another approach is a network derived from an ordinal partition of the time series.[11] In a sliding window scheme, the ordinal pattern of the windowed sequence corresponds to one node of the network. Nodes of consecutive sequences in the time series are connected in the network in order to save the temporal information. Since the amplitude information is neglected, this approach may be combined with a transition network, where the nodes of the network are the binned amplitudes of the time series.[12] A node then represents a combination of amplitude binning number and the ordinal pattern of the windowed sequence.

Often it is sufficient to analyze the characteristics of the network constructed from a time series. For example, in Refs. 8 and 12, the bifurcation diagram of a nonlinear system was analyzed. The different regimes were identified by dynamical changes of the measures as the control parameter was varied. In other cases, the network measures are not as descriptive and have to be compared to other data sets. In Ref. 13, the network of a time series was compared to a network that was created from points which were randomly drawn from the time series. Surrogates are another means to produce ersatz data. They have the same linear properties, i.e., the same autocorrelation function, as the original data while the nonlinear properties are randomized.[4] They provide a significant test for a given measure of nonlinearity by comparing the measure of the original time series to those of the surrogate data sets.

[a]Electronic mail: ingo.laut@dlr.de
[b]Electronic mail: christoph.raeth@dlr.de

Reuse of AIP Publishing content is subject to the terms at: https://publishing.aip.org/authors/rights-and-permissions. Downloaded to IP: 129.247.247.238 On: Fri, 21 Oct 2016 10:36:36

In this paper, we use recurrence and symbolic networks to test for weak nonlinearities in time series. To this end, network measures are calculated for the time series under study and for surrogate data sets. The performance of the network tests is compared to the nonlinear prediction error. The Lorenz system is used as a source of low-dimensional chaotic time series. In order to test both the ability to detect nonlinearities and the susceptibility to erroneously do so, the time series are mixed with a linear autoregressive (AR) process. As real-world data, light curves of active galactic nuclei (AGN) are examined. We attribute the performance differences of some surrogate generation algorithms to spurious nonlinearities that are introduced during the creation of the surrogates.

The paper is organized as follows. In Sec. II, we present the method of testing for nonlinearities with networks. In Sec. III, we describe the data sets and the process of mixing linear and nonlinear time series. In Sec. IV, we compare the performance of the tests for different data sets and surrogate generating algorithms. Induced correlations in the Fourier phases of some surrogates are also examined. Finally, in Sec. V, we conclude with a discussion and a summary of the main results.

II. METHODS

A. Networks

To create a recurrence network, a time series $\{y_n\}$ of length N is first embedded in an artificial phase space using the method of delay coordinates.[14,15] For an embedding dimension d and delay time τ, the method yields the state vector $\mathbf{y}_n = (y_{n-(d-1)\tau}, y_{n-(d-2)\tau}, \ldots, y_n)$ for the time steps $n = (d-1)\tau, (d-1)\tau+1, \ldots, N-1$. The adjacency matrix A of the recurrence network is defined as

$$A_{ij}(\epsilon) = \Theta(\epsilon - |\mathbf{y}_i - \mathbf{y}_j|) - \delta_{ij}, \tag{1}$$

where $\Theta(\cdot)$ is the Heaviside function, and ϵ is an appropriate threshold. The adjacency matrix connects points in the phase space that are sufficiently close to each other. The recurrence network has thus a total of $N_w = N - (d-1)\tau$ nodes. It is an undirected network since the adjacency matrix is symmetric. The recurrence network of the nonlinear time series shown in Fig. 1(a) can be seen in Fig. 1(b).

The symbolic network proposed in Ref. 12 is a directed network. Each time step n is associated with a symbol-pair containing the amplitude information $\alpha(n)$ and the ordinal pattern $\pi(n)$. The former is calculated by binning the time series in the interval $[\min(\{y_n\}), \max(\{y_n\})]$ into Q equal regions. $\alpha(n)$ is then simply the bin number of y_n. To compute $\pi(n)$, one considers the sequence $[y_n, y_{n+\tau}, \ldots, y_{n+(L-1)\tau}]$ for a given time-delay τ and window length L. The ordinal pattern $\pi(n) = (\beta_1, \beta_2, \ldots, \beta_L)$ contains the indices sorting the sequence such that $y_{n-1+\beta_1} \leq y_{n-1+\beta_2} \leq \ldots \leq y_{n-1+\beta_L}$. For example, the ordinal pattern corresponding to the sequence [1.2, 3.0, 2.0] is $\pi = (1, 3, 2)$. The symbol-pair at step n, $(\alpha(n), \pi(n))$, is then one node of the network, and it is connected by a directed link to the symbol-pair $(\alpha(n+1), \pi(n+1))$ of the successive time step. In this representation, different time steps may correspond to the same symbol-pairs. Only nodes whose symbol-pairs are present in the time series are part of the network; the actual number of nodes may thus be smaller than the maximal possible value $N_w^{\max} = Q \cdot L!$.

It was argued that the symbolic network provides a simple and robust scheme for phase space repartition where the window length L plays the role of the dimension d for time delay embedding.[11,12] In Fig. 2(a), the symbolic network constructed from the nonlinear time series of Fig. 1(a) is shown.

B. Measures

For the recurrence network, which is an undirected network, the local connectivity ρ_ν^{rec} is calculated by normalizing the number of nodes that are connected to node ν by the maximal value[9]

$$\rho_\nu^{\text{rec}} = \frac{1}{N_w - 1}\sum_i A_{\nu,i}, \quad \rho^{\text{rec}} = \frac{1}{N_w}\sum_\nu \rho_\nu^{\text{rec}}. \tag{2}$$

Here, N_w is the number of nodes of the network and $A_{\nu,i}$ is the adjacency matrix of a recurrence network. The average connectivity ρ^{rec} is calculated by averaging over all nodes of the network. If the attractor of the nonlinear time series is successfully reconstructed by the embedding, the recurrent trajectories will lead to a larger value of ρ^{rec} as compared to linear data sets. This can be seen in Fig. 1, where the average connectivity ρ^{rec} of a recurrence network derived from a nonlinear time series is compared to ρ^{rec} from surrogate data where the nonlinearities have been removed.

For the directed symbolic network described above, the degree k_ν^{sym} counts the number of links ending and starting at node ν separately

$$k_\nu^{\text{sym}} = \sum_i A_{\nu,i} + \sum_i A_{i,\nu}, \quad k^{\text{sym}} = \frac{1}{N_w}\sum_\nu k_\nu^{\text{sym}}. \tag{3}$$

As can be seen in Fig. 2, the nonlinear time series has a smaller value of the average degree k^{sym} than the linear surrogate. This can be understood by noting that the quasi-periodic orbits (QPOs) of the attractor lead to identical links between the symbols of the network, and thus to a smaller average degree.

The nonlinear prediction error (NLPE) is a commonly used test for nonlinearity.[2,16] In Ref. 17, it was found to be the one with the best overall performance for a broad range of applications. The NLPE of an embedded time series $\{\mathbf{y}_n\}$ is defined as[16]

$$\mathcal{E} = \frac{1}{\sqrt{N-T}}\sqrt{\sum_{i=0}^{N-T-1}\left(\mathbf{y}_{i+T} - \mathbf{F}[\mathbf{y}_i, g]\right)^2}, \tag{4}$$

where T is the lead time, and $\mathbf{F}$ is a predictor. The predictor $\mathbf{F}$ is calculated by averaging over the future values of the g nearest neighbors of point $\mathbf{y}_i$ a lead time T ahead. As the NLPE is calculated in an artificial embedding space, it also implicitly depends on the embedding dimension d and the delay time τ.

In order to perform a statistical test, the measures are compared to surrogate data described below. The size α of a

Reuse of AIP Publishing content is subject to the terms at: https://publishing.aip.org/authors/rights-and-permissions. Downloaded to IP: 129.247.247.238 On: Fri, 21 Oct 2016 10:36:36

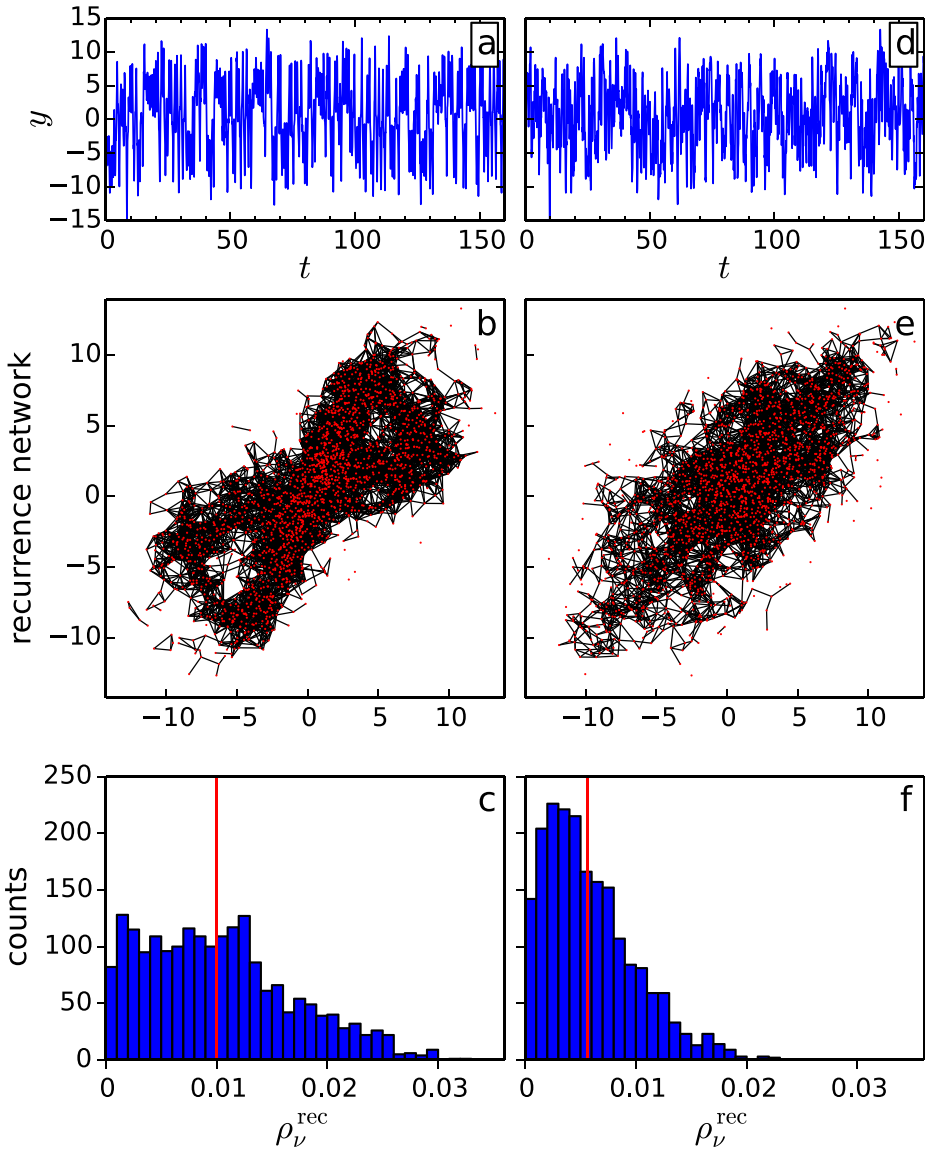

FIG. 1. Comparing the recurrence networks of a nonlinear time series and its AAFT surrogate. (a) A nonlinear time series with mixing parameter $m = 0.60$ (see Eq. (5)) consisting of $N = 2000$ time steps with a stepsize of $\delta t = 0.08$. (b) The recurrence network connects nodes that are sufficiently close in the embedded phase space. The threshold $\epsilon = 1.632$ was chosen such that the average connectivity obeys $\rho = 0.01$. The coordinates of the nodes in this representation are identical to the first two dimensions of the embedded time series into $d = 3$ dimension with delay time $\tau = 2\delta t$. The butterfly-shape of the attractor of the Lorenz system is clearly visible. (c) The distribution of the connectivity ρ_ν^{rec} for the recurrence network. The average connectivity ρ^{rec} is marked by a vertical line. (d)–(f) The same for an AAFT surrogate of the time series. The recurrence network in (e) is obtained for the same value of ϵ as for the original time series.

test is the probability that the null hypothesis is rejected, although it is in fact true.[17] A measure M is compared to the measures $\{M_{\mathrm{surro}}\}$ of B realizations of the surrogate data. As one expects a larger value of the average connectivity for recurrence networks in the presence of nonlinearity, the null hypothesis is rejected if ρ^{rec} is larger than all the $\{\rho^{\mathrm{rec}}_{\mathrm{surro}}\}$. The number of surrogates needed to achieve a given size of this *one-sided* test is $B = 1/\alpha - 1$. In the same manner, as one expects *smaller* values of the average degree for symbolic networks in the presence of nonlinearity, the null hypothesis is rejected if k^{sym} is smaller than the $\{k^{\mathrm{sym}}_{\mathrm{surro}}\}$. In the case of the NLPE, the null hypothesis of linearity is rejected if $\mathcal{E}$ is smaller than all the $\{\mathcal{E}_{\mathrm{surro}}\}$. By repeating the test, one can calculate the discrimination power $D(M)$ as the ratio of the number of rejections of the null hypothesis to the total number of tests.

For real-world data, there are often not enough time series available to calculate the discrimination power. In this case, the significance of the deviation of the time series from a set of surrogates is calculated as $S(M) = |M - \langle\{M_{\mathrm{surro}}\}\rangle| / \sigma(\{M_{\mathrm{surro}}\})$.

C. Surrogate algorithms

Surrogates are an important tool for the detection of nonlinearities in time series.[4,5,18–20] They are data sets which mimic the linear properties, i.e., the autocorrelation function, of the original data while possible higher order correlations are randomized. The most commonly used methods for generating surrogates are Fourier transformed (FT) surrogates and their amplitude-adjusted (AAFT) and iterative amplitude-adjusted (IAAFT) generalizations.

FT surrogates are compatible with the null hypothesis of a linear Gaussian process.[4] They are generated by randomizing the phases of the discrete Fourier transform of the original time series and subsequently performing the inverse transform. The Wiener-Khinchin theorem guarantees the surrogates to have the same autocorrelation function as the original time series. Being truly linear, the surrogates can unveil higher order correlations, however, this test is limited to time series which themselves obey a Gaussian distribution. The original time series therefore has to be rank-ordered-remapped to a Gaussian distribution prior to the analysis.[21]

Reuse of AIP Publishing content is subject to the terms at: https://publishing.aip.org/authors/rights-and-permissions. Downloaded to IP: 129.247.247.238 On: Fri, 21 Oct 2016 10:36:36

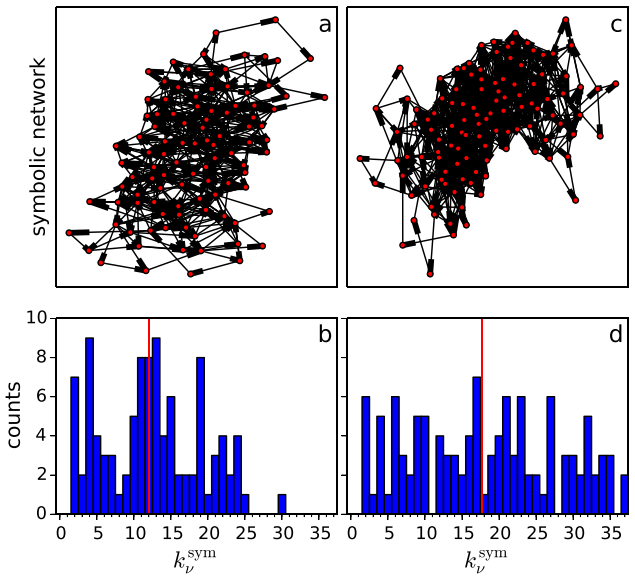

FIG. 2. Comparing the symbolic networks of the nonlinear time series of Fig. 1 and its AAFT surrogate. (a) The nodes (circles) of the network consist of symbols which are associated to each step of the time series, containing the ordinal pattern and amplitude information with $L=3$, $\tau=2\delta t$, and $Q=25$. The symbols of two successive time steps are connected by directed, unweighted links whose end points are indicated by a thicker end. (b) The corresponding degree distribution. The average degree k^{sym} is marked by a vertical line. (c) and (d) The same for the AAFT surrogate of the time series.

AAFT surrogates extend the null hypothesis to a Gaussian process which was distorted by an instantaneous, time-independent measurement function.[4] Here, a copy of the original time series is first rank-ordered remapped to a set of Gaussian random numbers. Then, FT surrogates of this remapped time series are created. Finally, the surrogates are rank-ordered remapped to the original time series. The surrogate now mimics both the autocorrelation function and the amplitude distribution. The final step, however, leads to a whitening of the power spectrum as compared to the original time series. In Ref. 5, it was shown that this may lead to an erroneous detection of nonlinearity in purely linear time series.

IAAFT surrogates were designed to overcome this shortcoming.[5] The method for generating IAAFT surrogates starts with a random shuffle $\{s_n\}$ of the original time series $\{y_n\}$. The Fourier amplitudes $\{\Phi_n\}$ of the original time series are saved. Now, the following two steps are repeated iteratively. (1) Take the Fourier transform of $\{s_n\}$, replace the corresponding Fourier amplitudes by $\{\Phi_n\}$, and transform back. $\{s_n\}$ has now exactly the same autocorrelation function as $\{y_n\}$, but not the same amplitude distribution. (2) Rank-ordered remap the resulting $\{s_n\}$ to $\{y_n\}$. As step (2) changes the power spectrum of the surrogate $\{s_n\}$, the two steps are repeated until the rank-ordered remapping no longer leads to a change in the surrogate.

III. DATA SETS

The tests for nonlinearity are applied to the well known Lorenz equations.[22] Time series containing $N=2000$ data points with a stepsize of $\delta t=0.08$ time units are considered (similar to Ref. 17). The x coordinates $\{x_n\}$ of the system are mixed with a (linear) autoregressive (AR) process $\{a_n\}$ in order to generate a new series $\{y_n\}$ that contains a fraction m of the nonlinear series. The same distorted AR process as in Ref. 5 is used; it reads $a_n=s_n\sqrt{|s_n|}$, $s_n=cs_{n-1}+\eta_n$ with $c=0.9$ and noise η_n drawn from a Gaussian distribution.

The mixed time series,

$$y_n=m\cdot x_n+(1-m)\cdot a_n, \tag{5}$$

is analyzed in order to test both the ability to detect weak nonlinearities and the susceptibility to erroneously reject the null hypothesis for a linear time series. A realization of a mixed time series for $m=0.6$ and its AAFT surrogate can be seen in Figs. 1(a) and 1(c).

In astrophysics, the analysis of light curves from AGN is important as the detection of nonlinearities can be used to test different theoretical models for the energy production at the center of the host galaxy.[23,24] An AGN is a luminous region at the very center of a galaxy that is powered by accretion onto a supermassive black hole. Seyfert galaxies discussed here are a subclass of radio-quiet AGN which are again subdivided into different types ranging from 1 to 2, depending on the observed line widths. It was argued that the variety of AGN is partly the result of different aspect angles.[25]

The contributions of a test for nonlinearity are twofold. First, linear models like global disk oscillation models[26] can be rejected with the detection of nonlinearities. Second, the analysis of the (nonlinear) dynamics can put to test different nonlinear models. For example, it was argued that AGN are galactic black hole binary systems with their masses scaled up.[27] Black hole binaries can be in the state of quasi periodic oscillation (QPO).[28] One evidence of the relation between galactic black hole systems and AGN would be the detection and characterization of QPOs in AGN data.[25] A unified model for these objects of very different masses and time scales would contribute greatly to the understanding of the physical processes close to a black hole.

The AGN data were taken from the public archive of the XMM-Newton satellite. The measured count rate of the pn-CCD camera was background subtracted and binned to a stepsize of $\delta t=50$ s. The first light curve considered here is a measurement of the Seyfert galaxy MCG-6-30-15 (MCG) taken during the 303th revolution of the satellite around the earth.[29] The time series is shown in Fig. 3, top row. With a duration of more than 120 kiloseconds (ks), or $N=2497$ time steps, it is the longest time series considered here. The bright narrow-line Seyfert 1 galaxy Mrk 766 (Mrk) has been observed by all main X-ray observatories. Here, a measurement taken by the XMM-Newton satellite, revolution 999, is used.[30] The light curve is shown in Fig. 3, middle row. Power density spectra have been analyzed by Markowitz *et al.*,[30] and a test for nonlinearity has previously shown a very significant outcome.[6] The significance of the detection of a QPO in another measurement on Mrk[31] was questioned by Benlloch *et al.*[32] The XMM-Newton observation of Ark 564 (Ark) during revolution 930 is also examined[33] (see Fig. 3, bottom row).

IV. RESULTS

A. Lorenz data

The delay time for the embedding of the mixed Lorenz data is set to $\tau=2\delta t=0.16$ such that the attractor is clearly

Reuse of AIP Publishing content is subject to the terms at: https://publishing.aip.org/authors/rights-and-permissions. Downloaded to IP: 129.247.247.238 On: Fri, 21 Oct 2016 10:36:36

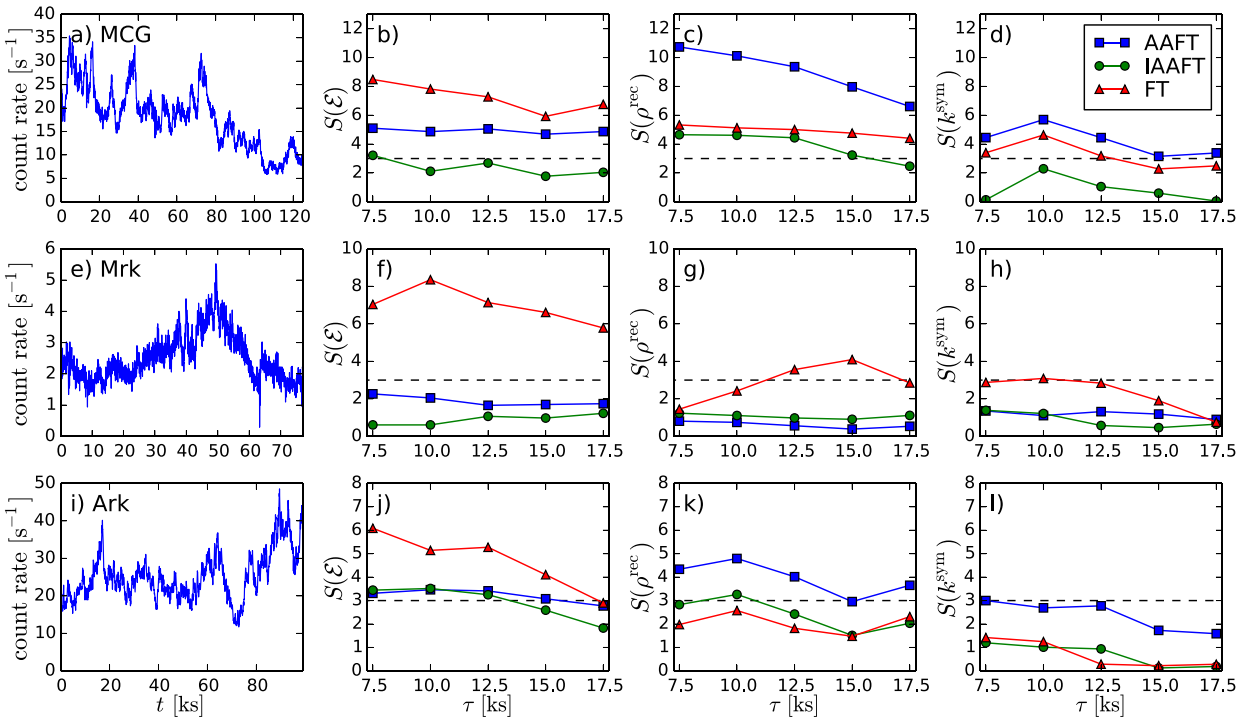

FIG. 3. Detection of nonlinearities in AGN time series. (a) The MCG time series, consisting of $N = 2497$ steps. (b) The significances $S(\mathcal{E})$ of the nonlinear prediction error $\mathcal{E}$ as a function of delay time τ. (c) The significances $S(\rho^{\mathrm{rec}})$ of the average connectivity ρ^{rec} for recurrence networks as a function of τ. (d) $S(k^{\mathrm{sym}})$ for symbolic networks as a function of τ. (e)–(h) The same for the Mrk time series consisting of $N = 1540$ steps. (i)–(l) The same for the Ark time series of $N = 1978$ steps. The step length of all time series is $\delta t = 50$ s. To calculate the significance, 400 surrogates were generated for each of the surrogate generating algorithms FT, AAFT, and IAAFT. For each measure, the 3σ detection limit is shown as a dashed line.

reconstructed for mixing parameter $m = 1$ (the "pure" Lorenz data). The appropriate embedding dimension d is determined with the false nearest neighbor statistics.[34] This method confirms the absence of false neighbors in the case of mixing parameter $m = 1$ for $d = 3$. To calculate the discrimination power $D(M)$ for the three measures M described in Sec. II, the tests of size $\alpha = 0.05$ are repeated 500 times. For $m = 0$, one expects $D(M) = \alpha$ as there are no nonlinearities present in the data and the null hypothesis is only rejected *by chance* when comparing the linear time series to the $B = 1/\alpha - 1$ surrogates. Larger values of $D(M)$ suggest then that the measure M is susceptible to erroneously detect nonlinearity in linear data. By increasing m, it can be studied how well weak nonlinearities are detected by the measure. Having checked that all tests perfectly detect the nonlinearities for $m > 0.6$, we show results for the values of m in the range $m = 0, 0.05, \ldots, 0.6$.

Varying the lead time T, the best results for the NLPE were found for $T = 2\delta t = 0.16$. The discrimination power $D(\mathcal{E})$ as a function of m can be seen in Fig. 4(a). The AAFT surrogates erroneously reject the null hypothesis at $m = 0$, where the series is a pure AR process, with a probability of 23%. This observation was used in Ref. 5 to argue the advantages of the IAAFT algorithm which indeed shows a lower percentage of false rejections. There, however, the performance of the algorithms was not compared for time series with spurious nonlinearities. In Fig. 4(a), it can be seen that at $m = 0.2$, the rejection probability of the IAAFT algorithm is still 5.2% which is very close to the size of the test. Before using the FT algorithm, the data sets are rank-order-remapped to a Gaussian distribution. The FT algorithm shows a good performance, starting at about 7.6% at $m = 0$ and showing a rejection probability of 21.4% at $m = 0.2$.

The same embedding parameters $d = 3$ and $\tau = 2\delta t$ are used for the recurrence network. The threshold ϵ is chosen such that the average connectivity of the time series is $\rho = 0.01$. The same threshold is then used for the surrogate data. Figure 4(b) shows the discrimination power $D(\rho^{\mathrm{rec}})$ of the test. The overall performance is similar to the NLPE, but slightly weaker. For $m = 0$, the FT and the AAFT surrogates have a slightly increased rejection probability of 8.8% and 10.2%, respectively. For intermediate values of the mixing parameter, $0.1 < m < 0.4$, the AAFT surrogates again show a high rejection probability, while the one for the IAAFT surrogates is very low.

Since the role of the window length L of the ordinal pattern is comparable to the embedding dimension d of time-delay embedding, $L = 3$ is used for the generation of symbolic networks. The same delay time $\tau = 2\delta t$ is used as for the embedding with delay coordinates. The amplitudes are binned to $Q = 25$ bins. The performance is again comparable to the NLPE (see Fig. 4(c)). AAFT surrogates have a slightly increased rejection probability $D(k^{\mathrm{sym}}) \simeq 9.8\%$ at $m = 0$, while, it is again smaller for the IAAFT surrogates at intermediate values of m. Here, however, the difference in performance of the three surrogate generating algorithms is very small.

Varying the embedding dimension d to larger values has only a weak influence on the results of the NLPE, while the discrimination power of the recurrence networks is already noticeably reduced for $d = 4$. Also the discrimination power of the symbolic networks is substantially reduced for larger

Reuse of AIP Publishing content is subject to the terms at: https://publishing.aip.org/authors/rights-and-permissions. Downloaded to IP: 129.247.247.238 On: Fri, 21 Oct 2016 10:36:36

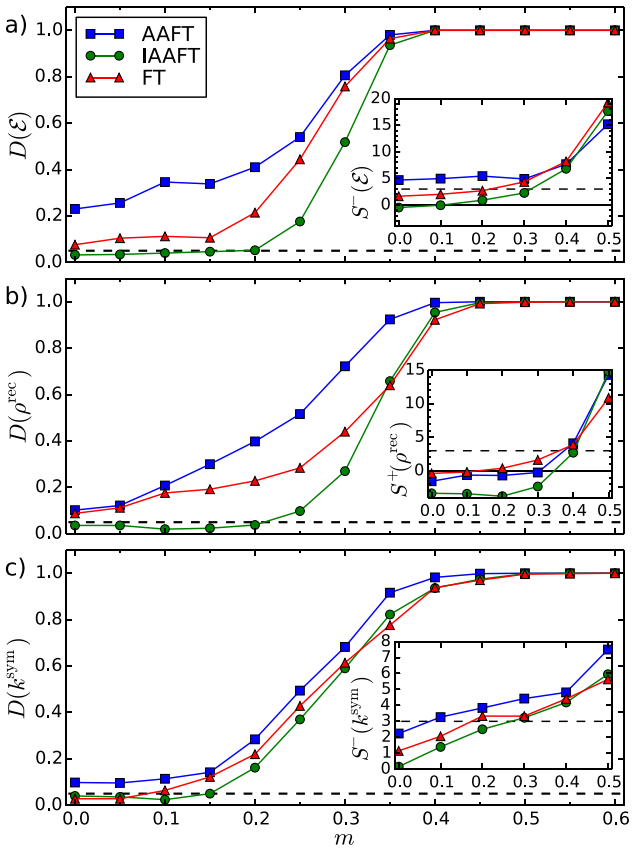

FIG. 4. Detection of nonlinearities in the mixed Lorenz system (see Eq. (5)). (a) Discrimination power $D(\mathcal{E})$ of the nonlinear prediction error as a function of mixing parameter m. Tests were carried out for 500 realizations of the mixed Lorenz system and three surrogate generating algorithms AAFT, IAAFT, and FT. The size $\alpha = 0.05$ of the test is shown as a dashed line. (b) The same for $D(\rho^{\mathrm{rec}})$ for the average connectivity of recurrence networks. (c) The same for $D(k^{\mathrm{sym}})$ for the average degree of symbolic networks. For comparison, the signed significance of a single realization of the time series is shown as an inset for each measure M as $S^{\pm}(M) = \pm(M - \langle\{M_{\mathrm{surro}}\}\rangle)/\sigma(\{M_{\mathrm{surro}}\})$. In the insets, the dashed line depicts the 3σ detection limit and the solid line $S^{\pm} = 0$.

L. Increasing the lead time T of the NLPE has almost no influence on the results.

The significance of tests based on a single realization of the time series is shown in the insets of Fig. 4. To facilitate the interpretation of the results for small m, the *signed* significance is calculated as $S^{\pm}(M) = \pm(M - \langle\{M_{\mathrm{surro}}\}\rangle)/\sigma(\{M_{\mathrm{surro}}\})$ which only yields large (positive) values if the measure M is larger (S^+) or smaller (S^-) than the average value of the surrogates, in conformity with the one-sided test of $D(M)$. For each test, 200 surrogates were used. The AAFT surrogates yield values above or near the 3σ detection limit for the NLPE and for the symbolic networks already at $m = 0$. A peculiarity is the negative value of $S^+(\rho^{\mathrm{rec}}) \simeq -4$ at $m = 0$ for the IAAFT surrogate which indicates that this measure detects *more nonlinearity* in the surrogates than in the (linear) time series. For larger m, the transition to significant values is comparable to the one of the discrimination power.

B. AGN light curves

One criterion of choosing the delay time τ for the AGN data is the first zero crossing of the autocorrelation function which varies from about $150\delta t = 7.5$ ks (Ark) to $350\delta t = 17.5$ ks (MCG). A range of $\tau = 7.5$, 10, 12.5, 15, and 17.5 ks is chosen. Determining the embedding dimension d, one has to find a compromise between avoiding false neighbors and maintaining enough data points due to the large delay times τ necessary for the data sets. $d = 3$ is a reasonable choice, as the number of false neighbors is already well below 10% for the AGN light curves considered here. The lead time for the NLPE is set to $T = 250$ s, or 5 time steps. The significances $S(\mathcal{E})$ of the NLPE for the three AGN curves depend strongly on the choice of the surrogate generation algorithm (see Fig. 3, second column). The FT surrogates show high significances for all curves. The AAFT surrogates show significant values for the MCG and slightly significant values $S(\mathcal{E}) \simeq 3.3$ for the Ark, while the IAAFT surrogates stay near or below the 3σ detection limit for all curves.

The significances of the tests from the recurrence networks with $d = 3$ are shown in Fig. 3, third column, as a function of delay time τ. The AAFT algorithm yields high significances for the MCG ($S(\rho^{\mathrm{rec}}) \simeq 10$) and Ark ($S(\rho^{\mathrm{rec}}) \simeq 5$) time series, while the other two algorithms show smaller significances. For the Mrk time series, the FT surrogates yield the highest significance $S(\rho^{\mathrm{rec}}) \simeq 4$, and the AAFT and IAAFT surrogates yield very low significances as was already the case for the NLPE.

To achieve significant results for the symbolic network, the sliding-window length is reduced to $L = 2$. The number of bins $Q = 25$ is the same as for the Lorenz data. The obtained significances $S(k^{\mathrm{sym}})$ are similar to those of the recurrence networks, but smaller. The AAFT surrogates yield significant values $S(k^{\mathrm{sym}}) \simeq 6$ for the MCG data, and values very close to the detection limit for the Ark data. As for the previous tests, no significant values are obtained from AAFT or IAAFT surrogates for the Mrk data.

The results depend rather weakly on the embedding dimension d. While the significances of the NLPE decrease with increasing d, $S(\rho^{\mathrm{rec}})$ tends to slightly increase for the FT surrogates. No significant results for $S(k^{\mathrm{sym}})$ were obtained for larger values of L. For d or L larger than 4, the number of data points becomes too small for a reasonable analysis. Using the *signed* significance defined in the caption of Fig. 4 only changes the sign of some measures with insignificant values of $S < 1$.

In Ref. 6, it was shown that the rank-ordered-remapping steps of the AAFT and IAAFT algorithms can introduce correlations in the Fourier phases of the surrogates. This may lead to a nondetection of weak nonlinearities in the time series. The FT surrogates, which are not rank-ordered-remapped, are not prone to phase correlations by construction. In the following, we will examine nonlinearities in the form of phase correlations in these surrogates for the Mrk data, where the difference between the FT surrogates and the (I)AAFT surrogates was most pronounced.

C. Phase correlations

In order to shed more light on the differences of the surrogate generation algorithms, the Fourier phases are analyzed using phase maps.[35] The phases of the Fourier modes $\{\phi_i\}$ are plotted versus the phases $\{\phi_{i+\Delta}\}$ of the modes that

Reuse of AIP Publishing content is subject to the terms at: https://publishing.aip.org/authors/rights-and-permissions. Downloaded to IP: 129.247.247.238 On: Fri, 21 Oct 2016 10:36:36

were shifted by a phase shift Δ. For a linear time series, the $\{\phi_n\}$ are independent, and thus scattered uniformly in the square bounded by $\pm\pi$. Structure in a phase map shows that the $\{\phi_n\}$ are not independent, which means that the phases contain information about the time series. One way to quantify the correlation in the phase maps is to calculate the cross correlation between $\{\phi_i\}$ and $\{\phi_{i+\Delta}\}$[6]

$$c(\Delta) = \frac{\langle \phi_i \phi_{i+\Delta} \rangle}{\sigma(\{\phi_i\})\sigma(\{\phi_{i+\Delta}\})} . \tag{6}$$

The average is performed over all possible pairs of shifted phases. c is normalized by the standard deviation of the phases, $\sigma(\{\phi_i\})$.

The FT scheme, which stops after randomizing the phases of the Fourier modes, is guaranteed to contain no phase information. The rank-ordering (AAFT) and the iteration scheme (IAAFT) can reintroduce phase correlations to the surrogates that only at the beginning of the algorithms were truly linear. As shown for AGN and financial market data in Ref. 6, these nonlinearities lead to a non-detection of nonlinearities in the time series.

In order to examine the impact of the phase correlations on the measures for nonlinearity, the NLPE of 200 surrogates of the Mkn data is plotted in Fig. 5(a) versus the cross correlation $c(\Delta = 1)$ of the phase maps. The delay time of the embedding is $\tau = 12.5$ ks. An anticorrelation for AAFT and IAAFT surrogates is clearly visible. This anticorrelation is quantified by calculating the cross correlation between $\mathcal{E}$ and c; the values are shown in the legend of Fig. 5. For the FT surrogates, there are no significant correlations.

Comparable results can be found for the recurrence network. In Fig. 5(b), the average connectivity ρ^{rec} is plotted versus the cross correlation $c(\Delta = 1)$. The values are now correlated instead of anticorrelated. This can be understood by noting that nonlinearities in the surrogates, quantified by a large value of c, lead to larger values of the average connectivity ρ^{rec}. In the case of the symbolic networks, where the difference between FT and (I)AAFT surrogates was less pronounced, k^{sym} and c are again anticorrelated, but the magnitude of the correlation coefficient is not as large as for the other two measures (see Fig. 5(c)).

V. DISCUSSION

The measures for nonlinearity derived from networks show a performance comparable to the NLPE when analyzing synthetic data of the mixed Lorenz equations. The different surrogate generating algorithms show the same tendencies for all measures: The AAFT surrogates tend to have a larger rejection probability, which may lead to a false rejection of the null hypothesis, i.e., a detection of nonlinearity in a linear data set. The IAAFT surrogates that were designed to overcome this problem show a relatively small rejection probability even when there is already a significant nonlinearity present in the data. Such a nondetection of nonlinearity may lead to a wrong (linear) modeling of the (nonlinear) system. The FT surrogates show the expected increase of the rejection probability when the nonlinearity is increased.

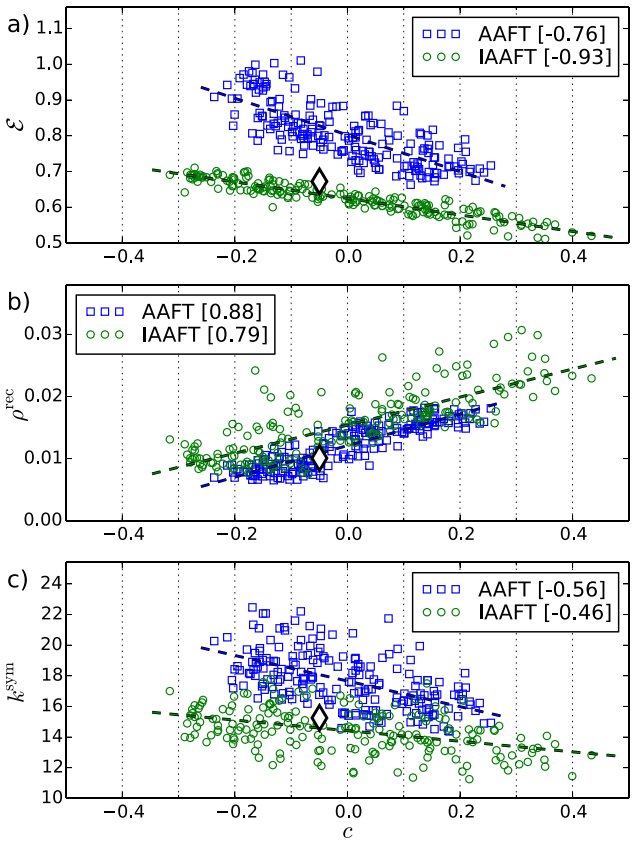

FIG. 5. Phase correlations in the surrogate data of the Mrk time series. (a) The nonlinear prediction error $\mathcal{E}$ as a function of the cross correlation in the phase maps c for $\Delta = 1$ (see Eq. (6)). A strong anticorrelation between the measures is clearly visible; the value of the cross correlation between $\mathcal{E}$ and c is given in square brackets in the legend for each surrogate generating algorithm. (b) The same for ρ^{rec} calculated for recurrence networks. (c) The same for k^{sym} calculated for symbolic networks. The values of the original time series are indicated by a white diamond. The dashed lines are shown to guide the eye.

In the case of AGN data, the differences are more severe. Significant values for all three light curves considered here are only obtained for the nonlinear prediction error in combination with FT surrogates. The analysis confirms that this measure is among the most robust measures for nonlinearity[17] and also that FT surrogates are not prone to induced nonlinearities during their generation.[6] The results suggest that the recurrence network is better suited to reconstruct the underlying phase space than the symbolic network which in all cases yields smaller significances. The tests based on networks yield significant values with AAFT surrogates only for two of the three light curves considered here.

In the special case of the Mrk light curve, an analysis of the phase relations of the AAFT and IAAFT surrogates shows that these algorithms induce phase correlations in the surrogate data which are correlated with the outcome of the test for nonlinearity.[6] These nonlinearities can explain the great differences between the significances of the FT surrogates on the one hand, and the AAFT and IAAFT surrogates on the other hand.

Analyzing the information encoded in the Fourier phases provides additional insight into the nonlinearities of a time series. In Ref. 36, the inverse approach was performed by analyzing the impact of manually created phase correlations on the outcome of nonlinearity measures. The correlations in the

Reuse of AIP Publishing content is subject to the terms at: https://publishing.aip.org/authors/rights-and-permissions. Downloaded to IP: 129.247.247.238 On: Fri, 21 Oct 2016 10:36:36

Fourier phases may thus not only help for checking surrogates for their linearity but also provide a powerful tool to discriminate linear from nonlinear time series.[37]

The analysis showed that surrogates provide a model-independent statistical test for measuring nonlinearities also in the rapidly evolving field of network analysis. Using FT surrogates of data that were rank-order-remapped to a Gaussian profile (or already obey a Gaussian distribution) seems to be the safest choice. In Ref. 38, network measures derived from the time series were compared to those of random networks.[39] It is probable that the outcome of the test depends on the type of random network used. "Surrogate networks" have also been proposed.[40,41]

To conclude, we have compared the tests for nonlinearity derived from networks to the nonlinear prediction error. While the performances are similar for the mixed Lorenz data, the nonlinear prediction error in combination with FT surrogates yields the most robust results for the real-world AGN data. Recurrence networks in combination with AAFT surrogates yield significant values only in two of the three AGN curves considered here. In the analysis of the third curve, we found phase correlations in the AAFT and IAAFT surrogates, which lead to a nondetection of the nonlinearities. Similar but less significant results are found for symbolic networks.

ACKNOWLEDGMENTS

The authors would like to thank the anonymous reviewers for their valuable comments that improved the quality of the paper. This work has made use of observations obtained with XMM-Newton, an ESA science mission with instruments and contributions directly funded by ESA member states and the U.S. (NASA).

[1]R. Albert and A.-L. Barabási, "Statistical mechanics of complex networks," Rev. Mod. Phys. **74**, 47–97 (2002).
[2]H. Kantz and T. Schreiber, *Nonlinear Time Series Analysis* (Cambridge University Press, 2004), Vol. 7.
[3]S. H. Strogatz, *Nonlinear Dynamics and Chaos* (Perseus Publishing, 2006).
[4]J. Theiler, S. Eubank, A. Longtin, B. Galdrikian, and J. Doyne Farmer, "Testing for nonlinearity in time series: The method of surrogate data," Physica D **58**, 77–94 (1992).
[5]T. Schreiber and A. Schmitz, "Improved surrogate data for nonlinearity tests," Phys. Rev. Lett. **77**, 635 (1996).
[6]C. Räth, M. Gliozzi, I. E. Papadakis, and W. Brinkmann, "Revisiting algorithms for generating surrogate time series," Phys. Rev. Lett. **109**, 144101 (2012).
[7]X. Xu, J. Zhang, and M. Small, "Superfamily phenomena and motifs of networks induced from time series," Proc. Natl. Acad. Sci. U.S.A. **105**, 19601–19605 (2008).
[8]N. Marwan, J. F. Donges, Y. Zou, R. V. Donner, and J. Kurths, "Complex network approach for recurrence analysis of time series," Phys. Lett. A **373**, 4246–4254 (2009).
[9]R. V. Donner, Y. Zou, J. F. Donges, N. Marwan, and J. Kurths, "Recurrence networks – a novel paradigm for nonlinear time series analysis," New J. Phys. **12**, 033025 (2010).
[10]J.-P. Eckmann, S. O. Kamphorst, and D. Ruelle, "Recurrence plots of dynamical systems," Europhys. Lett. **4**, 973–977 (1987).
[11]M. Small, "Complex networks from time series: Capturing dynamics," in *2013 IEEE International Symposium on Circuits and Systems* (IEEE, 2013), pp. 2509–2512.
[12]X. Sun, M. Small, Y. Zhao, and X. Xue, "Characterizing system dynamics with a weighted and directed network constructed from time series data," Chaos **24**, 024402 (2014).
[13]J. F. Donges, R. V. Donner, M. H. Trauth, N. Marwan, H.-J. Schellnhuber, and J. Kurths, "Nonlinear detection of paleoclimate-variability transitions possibly related to human evolution," Proc. Natl. Acad. Sci. U.S.A. **108**, 20422–20427 (2011).
[14]N. H. Packard, J. P. Crutchfield, J. D. Farmer, and R. S. Shaw, "Geometry from a time series," Phys. Rev. Lett. **45**, 712–716 (1980).
[15]F. Takens, *Detecting Strange Attractors in Turbulence*, Lecture Notes in Mathematics (Springer, 1981), pp. 366–381.
[16]G. Sugihara and R. May, "Nonlinear forecasting as a way of distinguishing chaos from measurement error in time series," Nature **344**, 734–734 (1990).
[17]T. Schreiber and A. Schmitz, "Discrimination power of measures for nonlinearity in a time series," Phys. Rev. E **55**, 5443 (1997).
[18]P. C. Ivanov, A. Yuen, B. Podobnik, and Y. Lee, "Common scaling patterns in intertrade times of US stocks," Phys. Rev. E **69**, 056107 (2004).
[19]K. J. Blinowska, R. Kuś, and M. Kamiński, "Granger causality and information flow in multivariate processes," Phys. Rev. E **70**, 050902 (2004).
[20]D. S. Bassett, M. A. Porter, N. F. Wymbs, S. T. Grafton, J. M. Carlson, and P. J. Mucha, "Robust detection of dynamic community structure in networks," Chaos **23**, 013142 (2013).
[21]By rank-ordered remapping a data set $\{x_n\}$ to $\{y_n\}$, we understand a reordering of $\{y_n\}$ such that if x_i is the ith smallest of the $\{x_n\}$, then y_i is the ith smallest of the $\{y_n\}$. The reordered $\{y_n\}$ thus "follows" the original set $\{x_n\}$ while having an amplitude distribution identical to the one of $\{y_n\}$.
[22]E. N. Lorenz, "Deterministic nonperiodic flow," J. Atmos. Sci. **20**, 130–141 (1963).
[23]B. M. Peterson, *An Introduction to Active Galactic Nuclei* (Cambridge University Press, 1997).
[24]M.-H. Ulrich, L. Maraschi, and C. M. Urry, "Variability of active galactic nuclei," Annu. Rev. Astron. Astrophys. **35**, 445–502 (1997).
[25]R. Antonucci, "Unified models for active galactic nuclei and quasars," Annu. Rev. Astron. Astrophys. **31**, 473–521 (1993).
[26]L. Titarchuk and V. Osherovich, "The global normal disk oscillations and the persistent low-frequency quasi-periodic oscillations in X-ray binaries," Astrophys. J. Lett. **542**, L111–L114 (2000).
[27]I. M. McHardy, E. Koerding, C. Knigge, P. Uttley, and R. P. Fender, "Active galactic nuclei as scaled-up Galactic black holes," Nature **444**, 730–732 (2006).
[28]R. A. Remillard and J. E. McClintock, "X-ray properties of black-hole binaries," Annu. Rev. Astron. Astrophys **44**, 49–92 (2006).
[29]S. Vaughan, A. C. Fabian, and K. Nandra, "X-ray continuum variability of MCG-6-30-15," Mon. Not. R. Astron. Soc. **339**, 1237–1255 (2003).
[30]A. Markowitz, I. Papadakis, P. Arévalo, T. Turner, L. Miller, and J. Reeves, "The energy-dependent X-ray timing characteristics of the narrow-line Seyfert 1 Mrk 766," Astrophys. J. **656**, 116 (2007).
[31]T. Boller, R. Keil, J. Trümper, P. O'Brien, J. Reeves, and M. Page, "Detection of an X-ray periodicity in the narrow-line Seyfert 1 galaxy Mrk 766 with XMM-Newton," Astron. Astrophys. **365**, L146–L151 (2001).
[32]S. Benlloch, J. Wilms, R. Edelson, T. Yaqoob, and R. Staubert, "Quasi-periodic oscillation in Seyfert galaxies: Significance levels. The case of Markarian 766," Astrophys. J. **562**, L121–L124 (2001).
[33]P. Arévalo, I. E. Papadakis, P. Uttley, I. M. McHardy, and W. Brinkmann, "Spectral-timing evidence for a very high state in the narrow-line Seyfert 1 Ark 564," Mon. Not. R. Astron. Soc. **372**, 401–409 (2006).
[34]M. B. Kennel, R. Brown, and H. D. I. Abarbanel, "Determining embedding dimension for phase-space reconstruction using a geometrical construction," Phys. Rev. A **45**, 3403–3411 (1992).
[35]L.-Y. Chiang, P. Coles, and P. Naselsky, "Return mapping of phases and the analysis of the gravitational clustering hierarchy," Mon. Not. R. Astron. Soc. **337**, 488–494 (2002).
[36]C. Räth and I. Laut, "Time series with tailored nonlinearities," Phys. Rev. E **92**, 040902(R) (2015).
[37]K. Schreiber, H. I. Modest, and C. Räth, "A test for Fourier phase correlations in nonlinear time series," (unpublished).
[38]A. K. Charakopoulos, T. E. Karakasidis, P. N. Papanicolaou, and A. Liakopoulos, "The application of complex network time series analysis in turbulent heated jets," Chaos **24**, 024408 (2014).
[39]P. Erdős and A. Rényi, "On the evolution of random graphs," Publ. Math. Inst. Hung. Acad. Sci. **5**, 17–61 (1960).
[40]G. Ansmann and K. Lehnertz, "Constrained randomization of weighted networks," Phys. Rev. E **84**, 026103 (2011).
[41]R. Mastrandrea, T. Squartini, G. Fagiolo, and D. Garlaschelli, "Reconstructing the world trade multiplex: the role of intensive and extensive biases," Phys. Rev. E **90**, 062804 (2014).

Reuse of AIP Publishing content is subject to the terms at: https://publishing.aip.org/authors/rights-and-permissions. Downloaded to IP: 129.247.247.238 On: Fri, 21 Oct 2016 10:36:36

Bibliography

[1] H. Kantz and T. Schreiber. *Nonlinear time series analysis*. Vol. 7. Cambridge university press (2004).

[2] S. H. Strogatz. *Nonlinear Dynamics and Chaos*. Perseus Publishing (2006).

[3] E. N. Lorenz. *Deterministic nonperiodic flow*. J. Atmos. Sci. **20**, 130 (1963).

[4] F. Takens et al. *Detecting strange attractors in turbulence*. Lecture Notes in Mathematics **898**, 366 (1981).

[5] N. H. Packard, J. P. Crutchfield, J. D. Farmer, and R. S. Shaw. *Geometry from a time series*. Phys. Rev. Lett. **45**, 712 (1980).

[6] M. B. Kennel, R. Brown, and H. D. I. Abarbanel. *Determining embedding dimension for phase-space reconstruction using a geometrical construction*. Phys. Rev. A **45**, 3403 (1992).

[7] A. M. Fraser and H. L. Swinney. *Independent coordinates for strange attractors from mutual information*. Phys. Rev. A **33**, 1134 (1986).

[8] G. U. Yule. *On a method of investigating periodicities in disturbed series, with special reference to Wolfer's sunspot numbers*. Philos. Trans. R. Soc. London A **226**, 267 (1927).

[9] G. Walker. *On periodicity in series of related terms*. Proc. Roy. Soc. A **131**, 518 (1931).

[10] N. Wiener. *Generalized harmonic analysis*. Acta Math. **55**, 117 (1930).

[11] P. Grassberger and I. Procaccia. *Measuring the strangeness of strange attractors*. Physica D **9**, 189 (1983).

[12] J. D. Farmer and J. J. Sidorowich. *Predicting chaotic time series*. Phys. Rev. Lett. **59**, 845 (1987).

[13] G. Sugihara and R. May. *Nonlinear forecasting as a way of distinguishing chaos from measurement error in time series*. Nature (London) **344**, 734 (1990).

[14] R. Albert and A.-L. Barabási. *Statistical mechanics of complex networks*. Rev. Mod. Phys. **74**, 47 (2002).

[15] M. E. J. Newman. *Mixing patterns in networks.* Phys. Rev. E **67**, 026126 (2003).

[16] G. Szabó and G. Fath. *Evolutionary games on graphs.* Phys. Rep. **446**, 97 (2007).

[17] S. Boccaletti, V. Latora, Y. Moreno, M. Chavez, and D.-U. Hwang. *Complex networks: Structure and dynamics.* Phys. Rep. **424**, 175 (2006).

[18] J. Zhang and M. Small. *Complex network from pseudoperiodic time series: Topology versus dynamics.* Phys. Rev. Lett. **96**, 238701 (2006).

[19] L. Lacasa, B. Luque, F. Ballesteros, J. Luque, and J. C. Nuño. *From time series to complex networks: The visibility graph.* Proc. Natl. Acad. Sci. USA **105**, 4972 (2008).

[20] N. Marwan, J. F. Donges, Y. Zou, R. V. Donner, and J. Kurths. *Complex network approach for recurrence analysis of time series.* Phys. Lett. A **373**, 4246 (2009).

[21] M. Small. "Complex networks from time series: capturing dynamics". *2013 IEEE International Symposium on Circuits and Systems*, 2509 (2013).

[22] X. Xu, J. Zhang, and M. Small. *Superfamily phenomena and motifs of networks induced from time series.* Proc. Natl. Acad. Sci. USA **105**, 19601 (2008).

[23] R. V. Donner, Y. Zou, J. F. Donges, N. Marwan, and J. Kurths. *Recurrence networks – A novel paradigm for nonlinear time series analysis.* New J. Phys. **12**, 033025 (2010).

[24] L. C. Freeman. *Centrality in social networks conceptual clarification.* Social Networks **1**, 215 (1979).

[25] X. Sun, M. Small, Y. Zhao, and X. Xue. *Characterizing system dynamics with a weighted and directed network constructed from time series data.* Chaos **24**, 024402 (2014).

[26] J. Theiler, S. Eubank, A. Longtin, B. Galdrikian, and D. J. Farmer. *Testing for nonlinearity in time series: the method of surrogate data.* Physica D **58**, 77 (1992).

[27] T. Schreiber and A. Schmitz. *Improved surrogate data for nonlinearity tests.* Phys. Rev. Lett. **77**, 635 (1996).

[28] C. Räth, M. Gliozzi, I. E. Papadakis, and W. Brinkmann. *Revisiting algorithms for generating surrogate time series.* Phys. Rev. Lett. **109**, 144101 (2012).

[29] C. K. Goertz. *Dusty plasmas in the solar system.* Rev. of Geophys. **27**, 271 (1989).

[30] H. Ikezi. *Coulomb solid of small particles in plasmas.* Phys. Fluids **29**, 1764 (1986).

[31] J. H. Chu and L. I. *Direct observation of Coulomb crystals and liquids in strongly coupled rf dusty plasmas.* Phys. Rev. Lett. **72**, 4009 (1994).

[32] H. Thomas, G. E. Morfill, V. Demmel, J. Goree, B. Feuerbacher, and D. Möhlmann. *Plasma crystal: Coulomb crystallization in a dusty plasma.* Phys. Rev. Lett. **73**, 652 (1994).

[33] Y. Hayashi and K. Tachibana. *Observation of Coulomb-crystal formation from carbon particles grown in a methane plasma.* Jpn. J. Appl. Phys. **33**, L804 (1994).

[34] P. K. Shukla and A. A. Mamun. *Introduction to Dusty Plasma Physics.* IOP Publishing, Bristol (2001).

[35] V. E. Fortov, A. V. Ivlev, S. A. Khrapak, A. G. Khrapak, and G. E. Morfill. *Complex (dusty) plasmas: Current status, open issues, perspectives.* Phys. Rep. **421**, 1 (2005).

[36] G. E. Morfill and A. V. Ivlev. *Complex plasmas: An interdisciplinary research field.* Rev. Mod. Phys. **81**, 1353 (2009).

[37] A. Ivlev, H. Löwen, G. Morfill, and C. P. Royall. *Complex Plasmas and Colloidal Dispersions: Particle-resolved Studies of Classical Liquids and Solids.* World Scientific, Singapore (2012).

[38] H. Rothermel, T. Hagl, G. E. Morfill, M. H. Thoma, and H. M. Thomas. *Gravity compensation in complex plasmas by application of a temperature gradient.* Phys. Rev. Lett. **89**, 175001 (2002).

[39] H. M. Thomas, G. E. Morfill, V. E. Fortov, A. V. Ivlev, V. I. Molotkov, A. M. Lipaev, T. Hagl, H. Rothermel, S. A. Khrapak, et al. *Complex plasma laboratory PK-3 Plus on the International Space Station.* New J. Phys. **10**, 033036 (2008).

[40] A. Piel, M. Klindworth, O. Arp, A. Melzer, and M. Wolter. *Obliquely propagating dust-density plasma waves in the presence of an ion beam.* Phys. Rev. Lett. **97**, 205009 (2006).

[41] M. A. Lieberman and A. J. Lichtenberg. *Principles of plasma discharges and materials processing.* Wiley, New York (2005).

[42] I. H. Hutchinson. *Ion collection by a sphere in a flowing plasma: 3. Floating potential and drag force.* Plasma Phys. Controlled Fusion **47**, 71 (2004).

[43] I. H. Hutchinson and L. Patacchini. *Computation of the effect of neutral collisions on ion current to a floating sphere in a stationary plasma.* Phys. Plasmas **14**, 013505 (2007).

[44] T. Bystrenko and A. Zagorodny. *Effects of bound states in the screening of dust particles in plasmas.* Phys. Lett. A **299**, 383 (2002).

[45] X.-Z. Tang and G. Luca Delzanno. *Orbital-motion-limited theory of dust charging and plasma response.* Phys. Plasmas **21**, 123708 (2014).

[46] V. N. Tsytovich. *Dust plasma crystals, drops, and clouds.* Physics-Uspekhi **40**, 53 (1997).

[47] S. A. Khrapak, G. E. Morfill, A. G. Khrapak, and L. G. D'yachkov. *Charging properties of a dust grain in collisional plasmas*. Phys. Plasmas **13**, 052114 (2006).

[48] S. Khrapak and G. Morfill. *Basic processes in complex (dusty) plasmas: charging, interactions, and ion drag force*. Contrib. Plasma Phys. **49**, 148 (2009).

[49] J. E. Daugherty, R. K. Porteous, M. D. Kilgore, and D. B. Graves. *Sheath structure around particles in low-pressure discharges*. J. Appl. Phys. **72**, 3934 (1992).

[50] S. Ratynskaia, U. De Angelis, S. Khrapak, B. Klumov, and G. E. Morfill. *Electrostatic interaction between dust particles in weakly ionized complex plasmas*. Phys. Plasmas **13**, 104508 (2006).

[51] I. L. Semenov, S. A. Khrapak, and H. M. Thomas. *Approximate expression for the electric potential around an absorbing particle in isotropic collisionless plasma*. Phys. Plasmas **22**, 053704 (2015).

[52] O. Ishihara and S. V. Vladimirov. *Wake potential of a dust grain in a plasma with ion flow*. Phys. Plasmas **4**, 69 (1997).

[53] M. Lampe, G. Joyce, G. Ganguli, and V. Gavrishchaka. *Interactions between dust grains in a dusty plasma*. Phys. Plasmas **7**, 3851 (2000).

[54] P. Ludwig, H. Kählert, and M. Bonitz. *Ion-streaming induced order transition in three-dimensional dust clusters*. Plasma Phys. Controlled Fusion **54**, 045011 (2012).

[55] D. Block, J. Carstensen, P. Ludwig, W. J. Miloch, F. Greiner, A. Piel, M. Bonitz, and A. Melzer. *Wake formation and wake field effects in complex plasmas*. Contrib. Plasma Phys. **52**, 804 (2012).

[56] I. H. Hutchinson. *Nonlinear collisionless plasma wakes of small particles*. Phys. Plasmas **18**, 032111 (2011).

[57] R. Kompaneets, A. V. Ivlev, V. Nosenko, and G. E. Morfill. *Wakes in inhomogeneous plasmas*. Physical Review E **89**, 043108 (2014).

[58] A. V. Ivlev and G. Morfill. *Anisotropic dust lattice modes*. Phys. Rev. E **63**, 016409 (2000).

[59] J. E. Daugherty, R. K. Porteous, and D. B. Graves. *Electrostatic forces on small particles in low-pressure discharges*. J. Appl. Phys. **73**, 1617 (1993).

[60] A. Melzer, V. A. Schweigert, and A. Piel. *Transition from attractive to repulsive forces between dust molecules in a plasma sheath*. Phys. Rev. Lett. **83**, 3194 (1999).

[61] S. Nunomura, T. Misawa, N. Ohno, and S. Takamura. *Instability of dust particles in a Coulomb crystal due to delayed charging*. Phys. Rev. Lett. **83**, 1970 (1999).

[62] C. Zafiu, A. Melzer, and A. Piel. *Nonlinear resonances of particles in a dusty plasma sheath*. Phys. Rev. E **63**, 066403 (2001).

[63] P. S. Epstein. *On the resistance experienced by spheres in their motion through gases.* Phys. Rev. **23**, 710 (1924).

[64] B. Liu, J. Goree, V. Nosenko, and L. Boufendi. *Radiation pressure and gas drag forces on a melamine-formaldehyde microsphere in a dusty plasma.* Phys. Plasmas **10**, 9 (2003).

[65] M. S. Barnes, J. H. Keller, J. C. Forster, J. A. O'Neill, and D. K. Coultas. *Transport of dust particles in glow-discharge plasmas.* Phys. Rev. Lett. **68**, 313 (1992).

[66] S. A. Khrapak, A. V. Ivlev, G. E. Morfill, and H. M. Thomas. *Ion drag force in complex plasmas.* Phys. Rev. E **66**, 046414 (2002).

[67] S. A. Khrapak, A. V. Ivlev, G. E. Morfill, and S. K. Zhdanov. *Scattering in the attractive Yukawa potential in the limit of strong interaction.* Phys. Rev. Lett. **90**, 225002 (2003).

[68] A. V. Ivlev, S. K. Zhdanov, S. A. Khrapak, and G. E. Morfill. *Ion drag force in dusty plasmas.* Plasma Phys. Controlled Fusion **46**, B267 (2004).

[69] A. V. Ivlev, S. K. Zhdanov, S. A. Khrapak, and G. E. Morfill. *Kinetic approach for the ion drag force in a collisional plasma.* Phys. Rev. E **71**, 016405 (2005).

[70] S. A. Khrapak, A. V. Ivlev, S. K. Zhdanov, and G. E. Morfill. *Hybrid approach to the ion drag force.* Phys. Plasmas **12**, 042308 (2005).

[71] V. A. Schweigert, I. V. Schweigert, A. Melzer, A. Homann, and A. Piel. *Plasma crystal melting: a nonequilibrium phase transition.* Phys. Rev. Lett. **80**, 5345 (1998).

[72] C. Killer, T. Bockwoldt, S. Schütt, M. Himpel, A. Melzer, and A. Piel. *Phase separation of binary charged particle systems with small size disparities using a dusty plasma.* Phys. Rev. Lett. **116**, 115002 (2016).

[73] H. M. Thomas and G. E. Morfill. *Melting dynamics of a plasma crystal.* Nature (London) **379**, 806 (1996).

[74] C. A. Knapek, D. Samsonov, S. Zhdanov, U. Konopka, and G. E. Morfill. *Recrystallization of a 2D plasma crystal.* Phys. Rev. Lett. **98**, 015004 (2007).

[75] T. Misawa, N. Ohno, K. Asano, M. Sawai, S. Takamura, and P. K. Kaw. *Experimental observation of vertically polarized transverse dust-lattice wave propagating in a one-dimensional strongly coupled dust chain.* Phys. Rev. Lett. **86**, 1219 (2001).

[76] S. Nunomura, D. Samsonov, S. Zhdanov, and G. Morfill. *Heat transfer in a two-dimensional crystalline complex (dusty) plasma.* Phys. Rev. Lett. **95**, 025003 (2005).

[77] V. Nosenko, K. Avinash, J. Goree, and B. Liu. *Nonlinear interaction of compressional waves in a 2D dusty plasma crystal.* Phys. Rev. Lett. **92**, 085001 (2004).

[78] V. Nosenko, J. Goree, and F. Skiff. *Bispectral analysis of nonlinear compressional waves in a two-dimensional dusty plasma crystal*. Phys. Rev. E **73**, 016401 (2006).

[79] Y.-Y. Tsai, J.-Y. Tsai, and L. I. *Generation of acoustic rogue waves in dusty plasmas through three-dimensional particle focusing by distorted waveforms*. Nat. Phys. **12**, 573 (2016).

[80] Y.-Y. Tsai, M.-C. Chang, J.-Y. Tsai, and L. I. *Spontaneous excitations of low amplitude hole filaments, acoustic vortices, and rogue wave events in weakly disordered dust acoustic waves*. Plasma Phys. Controlled Fusion **59**, 054006 (2017).

[81] L. Wörner, C. Räth, V. Nosenko, S. K. Zhdanov, H. M. Thomas, G. E. Morfill, J. Schablinski, and D. Block. *String structures in driven 3D complex-plasma clusters*. Europhys. Lett. **100**, 35001 (2012).

[82] I. Laut, C. Räth, L. Wörner, V. Nosenko, S. K. Zhdanov, J. Schablinski, D. Block, H. M. Thomas, and G. E. Morfill. *Network analysis of three-dimensional complex plasma clusters in a rotating electric field*. Phys. Rev. E **89**, 023104 (2014).

[83] A. V. Ivlev, M. H. Thoma, C. Räth, G. Joyce, and G. E. Morfill. *Complex plasmas in external fields: The role of non-Hamiltonian interactions*. Phys. Rev. Lett. **106**, 155001 (2011).

[84] A. V. Ivlev, U. Konopka, G. E. Morfill, and G. Joyce. *Melting of monolayer plasma crystals*. Phys. Rev. E **68**, 026405 (2003).

[85] L. Couëdel, S. K. Zhdanov, A. V. Ivlev, V. Nosenko, H. M. Thomas, and G. E. Morfill. *Wave mode coupling due to plasma wakes in two-dimensional plasma crystals: In-depth view*. Phys. Plasmas **18**, 083707 (2011).

[86] A. V. Ivlev, J. Bartnick, M. Heinen, C.-R. Du, V. Nosenko, and H. Löwen. *Statistical mechanics where Newton's third law is broken*. Phys. Rev. X **5**, 011035 (2015).

[87] L. Couëdel, V. Nosenko, A. V. Ivlev, S. K. Zhdanov, H. M. Thomas, and G. E. Morfill. *Direct observation of mode-coupling instability in two-dimensional plasma crystals*. Phys. Rev. Lett. **104**, 195001 (2010).

[88] L. Couëdel, S. Zhdanov, V. Nosenko, A. V. Ivlev, H. M. Thomas, and G. E. Morfill. *Synchronization of particle motion induced by mode coupling in a two-dimensional plasma crystal*. Phys. Rev. E **89**, 053108 (2014).

[89] S. K. Zhdanov, A. V. Ivlev, and G. Morfill. *Mode-coupling instability of two-dimensional plasma crystals*. Phys. Plasmas **16**, 083706 (2009).

[90] T. B. Röcker, A. V. Ivlev, R. Kompaneets, and G. E. Morfill. *Mode coupling in two-dimensional plasma crystals: Role of the wake model*. Phys. Plasmas **19**, 033708 (2012).

[91] T. B. Röcker, A. V. Ivlev, S. K. Zhdanov, and G. E. Morfill. *Effect of strong wakes on waves in two-dimensional plasma crystals*. Phys. Rev. E **89**, 013104 (2014).

[92] R. Kompaneets, U. Konopka, A. V. Ivlev, V. Tsytovich, and G. Morfill. *Potential around a charged dust particle in a collisional sheath*. Phys. Plasmas **14**, 052108 (2007).

[93] D. Samsonov, J. Goree, Z. W. Ma, A. Bhattacharjee, H. M. Thomas, and G. E. Morfill. *Mach cones in a coulomb lattice and a dusty plasma*. Phys. Rev. Lett. **83**, 3649 (1999).

[94] D. Samsonov, J. Goree, H. M. Thomas, and G. E. Morfill. *Mach cone shocks in a two-dimensional Yukawa solid using a complex plasma*. Phys. Rev. E **61**, 5557 (2000).

[95] D. H. E. Dubin. *The phonon wake behind a charge moving relative to a two-dimensional plasma crystal*. Phys. Plasmas **7**, 3895 (2000).

[96] O. Havnes, F. Li, F. Melandso/, T. Aslaksen, T. Hartquist, G. Morfill, T. Nitter, and V. Tsytovich. *Diagnostic of dusty plasma conditions by the observation of Mach cones caused by dust acoustic waves*. J. Vac. Sci. Technol. A **14**, 525 (1996).

[97] C.-R. Du, V. Nosenko, S. Zhdanov, H. M. Thomas, and G. E. Morfill. *Interaction of two-dimensional plasma crystals with upstream charged particles*. Europhys. Lett. **99**, 55001 (2012).

[98] C.-R. Du, V. Nosenko, S. Zhdanov, H. M. Thomas, and G. E. Morfill. *Channeling of particles and associated anomalous transport in a two-dimensional complex plasma crystal*. Phys. Rev. E **89**, 021101(R) (2014).

[99] H. Totsuji, C. Totsuji, and K. Tsuruta. *Structure of finite two-dimensional Yukawa lattices: Dust crystals*. Phys. Rev. E **64**, 066402 (2001).

[100] T. Ott, M. Bonitz, L. G. Stanton, and M. S. Murillo. *Coupling strength in Coulomb and Yukawa one-component plasmas*. Phys. Plasmas **21**, 113704 (2014).

[101] K. Qiao, J. Kong, E. Van Oeveren, L. S. Matthews, and T. W. Hyde. *Mode couplings and resonance instabilities in dust clusters*. Phys. Rev. E **88**, 043103 (2013).

[102] I. Laut, C. Räth, S. Zhdanov, V. Nosenko, L. Couëdel, and H. M. Thomas. *Synchronization of particle motion in compressed two-dimensional plasma crystals*. Europhys. Lett. **110**, 65001 (2015).

[103] S. K. Zhdanov, M. H. Thoma, and G. E. Morfill. *Spontaneous disordering of a two-dimensional (2D) plasma crystal*. New J. Phys. **13**, 013039 (2011).

[104] S. Zhdanov, R. A. Quinn, D. Samsonov, and G. E. Morfill. *Large-scale steady-state structure of a 2D plasma crystal*. New J. Phys. **5**, 74 (2003).

[105] T. E. Sheridan. *Melting transition in a two-dimensional complex plasma heated by driven acoustic instability.* Phys. Plasmas **15**, 103702 (2008).

[106] T. E. Sheridan. *Monte Carlo study of melting in a finite two-dimensional dusty plasma.* Phys. Plasmas **16**, 083705 (2009).

[107] J. Schablinski, D. Block, J. Carstensen, F. Greiner, and A. Piel. *Sheared and unsheared rotation of driven dust clusters.* Phys. Plasmas **21**, 073701 (2014).

[108] C. Durniak, D. Samsonov, N. P. Oxtoby, J. F. Ralph, and S. Zhdanov. *Molecular-dynamics simulations of dynamic phenomena in complex plasmas.* IEEE Trans. Plasma Sci. **38**, 2412 (2010).

[109] P. Schofield. *Computer simulation studies of the liquid state.* Comput. Phys. Commun. **5**, 17 (1973).

[110] D. Beeman. *Some multistep methods for use in molecular dynamics calculations.* J. Comput. Phys. **20**, 130 (1976).

[111] Z. Donkó, G. J. Kalman, and P. Hartmann. *Dynamical correlations and collective excitations of Yukawa liquids.* J. Phys. Condens. Matter **20**, 413101 (2008).

[112] P. Ramachandran and G. Varoquaux. *Mayavi: 3D visualization of scientific data.* Comput. Sci. Eng. **13**, 40 (2011).

[113] I. Laut, S. K. Zhdanov, C. Räth, H. M. Thomas, and G. E. Morfill. *Anisotropic confinement effects in a two-dimensional plasma crystal.* Phys. Rev. E **93**, 013204 (2016).

[114] Y. Kuramoto. *Cooperative dynamics of oscillator community a study based on lattice of rings.* Progr. Theoret. Phys. Suppl. **79**, 223 (1984).

[115] C. A. Knapek, C. Durniak, D. Samsonov, and G. E. Morfill. *Scale-free behavior of a 2D complex plasma during rapid cooling.* Phys. Rev. Lett. **110**, 035001 (2013).

[116] V. Nosenko, S. Zhdanov, and G. Morfill. *Supersonic dislocations observed in a plasma crystal.* Phys. Rev. Lett. **99**, 025002 (2007).

[117] J. Paulose, B. G. Chen, and V. Vitelli. *Topological modes bound to dislocations in mechanical metamaterials.* Nat. Phys. **11**, 153 (2015).

[118] A. V. Ivlev, T. B. Röcker, L. Couëdel, V. Nosenko, and C.-R. Du. *Wave modes in shear-deformed two-dimensional plasma crystals.* Phys. Rev. E **91**, 063108 (2015).

[119] M. Haslauer, I. Laut, and C. Räth. *Self-organized pattern formation in a linear interacting plasma crystal,* In preparation. (2017).

[120] J. K. Meyer, I. Laut, S. K. Zhdanov, V. Nosenko, and H. M. Thomas. *Coupling of non-crossing wave modes in a two-dimensional plasma crystal.* Submitted for publication in Phys. Rev. Lett. (2017).

[121] I. Laut, C. Räth, S. K. Zhdanov, V. Nosenko, G. E. Morfill, and H. M. Thomas. *Wake-mediated propulsion of an upstream particle in two-dimensional plasma crystals*. Phys. Rev. Lett. **118**, 075002 (2017).

[122] L. Couëdel, T. B. Röcker, S. K. Zhdanov, V. Nosenko, H. M. Thomas, and A. V. Ivlev. *Forced mode coupling in 2D complex plasmas*. Europhys. Lett. **115**, 45002 (2016).

[123] R. Bechinger, R. Di Leonardo, H. Löwen, C. Reichhardt, G. Volpe, and G. Volpe. *Active particles in complex and crowded environments*. Rev. Mod. Phys. **88**, 045006 (2016).

[124] J. Bartnick, A. Kaiser, H. Löwen, and A. V. Ivlev. *Emerging activity in bilayered dispersions with wake-mediated interactions*. J. Chem. Phys. **144**, 224901 (2016).

[125] P. Bandyopadhyay, R. Dey, and A. Sen. *Interaction and propagation characteristics of two counter and co-propagating Mach cones in a dusty plasma*. Phys. Plasmas **24**, 033706 (2017).

[126] C. Räth and I. Laut. *Time series with tailored nonlinearities*. Phys. Rev. E **92**, 040902(R) (2015).

[127] I. Laut and C. Räth. *Surrogate-assisted network analysis of nonlinear time series*. Chaos **26**, 103108 (2016).

[128] L.-Y. Chiang and P. Coles. *Phase information and the evolution of cosmological density perturbations*. Mon. Not. R. Astron. Soc. **311**, 809 (2000).

[129] P. Coles and L.-Y. Chiang. *Characterizing the nonlinear growth of large-scale structure in the Universe*. Nature (London) **406**, 376 (2000).

[130] L.-Y. Chiang, P. D. Naselsky, O. V. Verkhodanov, and M. J. Way. *Non-gaussianity of the derived maps from the first-year Wilkinson Microwave Anisotropy Probe data*. Astrophys. J. Lett. **590**, L65 (2003).

[131] P. Coles, P. Dineen, J. Earl, and D. Wright. *Phase correlations in cosmic microwave background temperature maps*. Mon. Not. R. Astron. Soc. **350**, 989 (2004).

[132] N. P. Subramaniyam and J. Hyttinen. *Characterization of dynamical systems under noise using recurrence networks: Application to simulated and EEG data*. Phys. Lett. A **378**, 3464 (2014).

[133] H. Dickten and K. Lehnertz. *Identifying delayed directional couplings with symbolic transfer entropy*. Phys. Rev. E **90**, 062706 (2014).

[134] S. Birkholz, C. Brée, A. Demircan, and G. Steinmeyer. *Predictability of rogue events*. Phys. Rev. Lett. **114**, 213901 (2015).

[135] K. Hayashi, H. Gotoda, and P. L. Gentili. *Probing and exploiting the chaotic dynamics of a hydrodynamic photochemical oscillator to implement all the basic binary logic functions*. Chaos **26**, 053102 (2016).

[136] O. Adegoke, S. Rakshit, and B. Mukhopadhyay. *Spectral and Time Series Analyses of the Seyfert 1 AGN: Zw 229.015*. Mon. Not. R. Astron. Soc. **466**, 3951 (2017).

[137] N. S. Carver and D. G. Kelty-Stephen. *Multifractality in individual honeybee behavior hints at colony-specific social cascades: Reanalysis of radio-frequency identification data from five different colonies*. Phys. Rev. E **95**, 022402 (2017).

[138] T. Schreiber and A. Schmitz. *Discrimination power of measures for nonlinearity in a time series*. Phys. Rev. E **55**, 5443 (1997).

[139] L.-Y. Chiang, P. Coles, and P. Naselsky. *Return mapping of phases and the analysis of the gravitational clustering hierarchy*. Mon. Not. R. Astron. Soc. **337**, 488 (2002).

[140] A. Markowitz, I. Papadakis, P. Arévalo, T. Turner, L. Miller, and J. Reeves. *The energy-dependent X-ray timing characteristics of the narrow-line Seyfert 1 Mrk 766*. Astrophys. J. **656**, 116 (2007).

Acknowledgment

I would like to express my gratitude to my supervisor Gregor Morfill for his support. Thank you for your guidance during the preparation of this thesis.

Very special thanks go to my direct supervisor Christoph Räth. You had a sincere interest in my development and taught me, among many other things, to go beyond the beaten tracks.

I would like to thank Sergey Zhdanov for sharing his huge experience and curiosity. I am happy that besides the many discussions and projects, you also played an official role in my thesis as my mentor. I would like to thank Vladimir Nosenko for his valuable discussions, his physical intuition and his accuracy in reading and writing scientific thoughts. Many thanks to Lénaïc Couëdel and Cheng-Ran Du for providing me experimental data and many interesting ideas. I would like to thank Hubertus Thomas and all the present and former members of the complex plasma research group, in particular the PhD students from the "other room" Alexander Böbel, Erich Zähringer and Meike Müller.